TAMPEREEN TEKNILLINEN YLIOPISTO
TAMPERE UNIVERSITY OF TECHNOLOGY

Jaakko Saarela

Gas-Phase Photoacoustic Spectroscopy

Advanced Methods for Photoacoustic Detection and Signal Processing

Julkaisu 998 • Publication 998

Tampere 2011

Tampereen teknillinen yliopisto. Julkaisu 998
Tampere University of Technology. Publication 998

Jaakko Saarela

Gas-Phase Photoacoustic Spectroscopy

Advanced Methods for Photoacoustic Detection and Signal Processing

Thesis for the degree of Doctor of Science in Technology to be presented with due permission for public examination and criticism in Tietotalo Building, Auditorium TB104, at Tampere University of Technology, on the 18th of November 2011, at 12 noon.

Tampereen teknillinen yliopisto - Tampere University of Technology
Tampere 2011

ISBN 978-952-15-2676-3 (printed)
ISBN 978-952-15-2729-6 (PDF)
ISSN 1459-2045

Abstract

Photoacoustic spectroscopy (PAS), as a branch of optical spectroscopy, is an established, robust, and sensitive method for trace gas monitoring. The concentration of a specific gas compound, among many other physical properties, can be revealed by using photoacoustics. In the photoacoustic (PA) effect modulated light is absorbed by the gas. The energy of the absorbed light is converted to sound due to an increase in the temperature and pressure of the gas. The induced sound waves are detected with a microphone. In the trace gas detection the sensitivity of the PA sensor is a crucial parameter, which affects the reliability of the measurement. In this work, new photoacoustic measurement and signal processing techniques are developed for the detection of three gaseous components: the greenhouse gas carbon dioxide, the atmospheric pollutant nitrogen dioxide, and the anesthetic agent propofol.

Carbon dioxide was used as a target gas in a research where different wavelength modulation waveforms were studied for the use in tunable diode laser PAS. The selection of the waveform and amplitude affect the sensitivity of the measurement. In addition, slow tuning of the laser can reduce the performance of the PA system. A novel shaped waveform was introduced which gives an enhanced sensitivity and which is less prone to the delayed wavelength tuning of the laser.

Three of the publications included into this thesis deal with nitrogen dioxide detection using a new type of microphone that was recently introduced for the PA method. The transducer is an electromechanical film microphone (EMFIT) whose sensitivity is comparable to those of the traditional microphones but, in addition, has an extremely broadband acoustic response, which is especially useful in PAS at high signal frequencies. The films can be layered and formed to different shapes for easy integration into all kinds of PA sensor designs. The films are also cheap so that low-cost but sensitive PA sensors can be realized. It was shown that the EMFIT films can be used for the detection of nitrogen dioxide in simple and cost-effective PA sensors which nevertheless are highly sensitive. The best limit of detection for nitrogen dioxide using low-cost light-emitting diodes as light sources is 10 ppb, and it was demonstrated in this thesis.

Photoacoustic detection of gas-phase propofol was demonstrated for the first time. Using pulsed PAS, a detection limit of 0.12 ppb was achieved which is well below typical propofol concentrations in patients' exhaled breath during surgical procedures.

Preface

The work of this Ph.D. thesis has been carried out in the Optics Laboratory of Department of Physics of Tampere University of Technology during the years 2007-2011. The Department of Physics and Finnish Academy of Science and Letters are acknowledged for the financial support.

I thank my supervisor Doc. Juha Toivonen for the guidance and support he has given during the years of this work. I am extremely thankful to my former colleagues Ph.D. Albert Manninen and M.Sc. Tapio Sorvajärvi. Lots of things have been shared and learnt together through the multitude of discussions about the scientific challenges and planning of measurements. Johan, Samu, Antti, Hannu, Miro, and Toni: it has also been pleasant to work with you. In addition, all the people in the Optics lab deserve a word of thanks for the nice working atmosphere.

The beacons of my life are my wife Johanna and son Joonas. My parents have been really supportive during the years of my studies and life. Unfortunately, my late father is not here among us to see the outcome of their support.

Tampere, November 2011

Jaakko Saarela

Contents

List of publications

Publ. 1 J. Saarela, J. Toivonen, A. Manninen, T. Sorvajärvi, and R. Hernberg, "Wavelength modulation waveforms in laser photoacoustic spectroscopy," Appl. Opt. **48**, 743–747 (2009).

Publ. 2 A. Manninen, J. Sand, J. Saarela, T. Sorvajärvi, J. Toivonen, and R. Hernberg, "Electromechanical film as a photoacoustic transducer," Opt. Express **17**, 16994–16999 (2009).

Publ. 3 J. Saarela, J. Sand, T. Sorvajärvi, A. Manninen, and J. Toivonen, "Transversely Excited Multipass Photoacoustic Cell Using Electromechanical Film as Microphone," Sensors **10**, 5294–5307 (2010).

Publ. 4 T. Laurila, T. Sorvajärvi, J. Saarela, J. Toivonen, D. W. Wheeler, L. Ciaffoni, G. A. D. Ritchie, and C. F. Kaminski, "Optical Detection of the Anesthetic Agent Propofol in the Gas Phase," Analytical Chemistry **83**, 3963–3967 (2011).

Publ. 5 J. Saarela, T. Sorvajärvi, T. Laurila, and J. Toivonen, "Phase-sensitive method for background-compensated photoacoustic detection of NO_2 using high-power LEDs," Opt. Express **19**, A725–A732 (2011).

Author's contribution

The Thesis consists of five publications. All the publications deal with recent advances made in the field of photoacoustic spectroscopy of different trace gases. Short descriptions about the subjects and the key results of the five publications, and the contribution of the author of this dissertation to each of the studies are listed below.

Publ. 1

This paper describes the use of different wavelength modulation waveforms in tunable diode laser photoacoustic spectroscopy. It was shown both by way of simulations and experiments that the selection of a proper modulation waveform and parameters have a significant effect on the generation of the photoacoustic signal and the sensitivity of the detector. This study offers knowledge how to increase the sensitivity of a given photoacoustic system by optimizing the laser modulation. The author had the full contribution in the preparation, experiments, simulations, data analysis, and reporting of the work.

Publ. 2

This is the first study in the field of photoacoustic spectroscopy where the newly developed electromechanical film is introduced as a microphone. The acoustic response of the electromechanical film is unique due to its relatively high sensitivity, extremely wide detection bandwidth, formability, and possibility to layer multiple films to further increase the sensitivity. In this study, the electromechanical film is installed onto the inner surface of a cylindrical photoacoustic cell, and it is used for high-frequency resonant photoacoustic detection of nitrogen dioxide together with a high-power pulsed laser. The author took part into the measurements and preparation of the manuscript of the study as a co-author.

Publ. 3

In this publication the photoacoustic method with the electromechanical film as a microphone is developed for a low-power continuous wave laser. The developed photoacoustic sensor consisted of a novel open acoustic resonator. Extra sensitivity was gained with respect to common photoacoustic devices by using an optical multipass cavity to increase the low power of the laser excitation. The in-house built microphone film stacks were characterized. The author did most of the preparations, and had the full responsibility of the measurements, analysis and reporting.

Publ. 4

In the study the optical detection of the anesthetic agent propofol in the gas phase is demonstrated. It is shown that photoacoustic spectroscopy has potential as a measurement technique for clinical use. The study was a broad co-operation between several research institutes. The author contributed to the measurements, data processing and reporting of the photoacoustic and absorption measurements carried out in the ultraviolet region.

Publ. 5

This publication continues on the topic of using the electromechanical film in photoacoustic spectroscopy. A cost-effective, and sensitive photoacoustic sensor is developed for nitrogen dioxide using an array of modern high-power LEDs in a robust measurement cell. A special emphasis is paid on the signal processing and automated operation of the measurement device. The author designed the measurement cell structure, built the microphones, planned and carried out all the measurements, and wrote the manuscript.

List of figures

List of tables

List of symbols

CW	Continuous wave
DAQ	Data acquisition unit
DFB	Distributed-feedback
DFT	Discrete Fourier transform
EMFIT	Electromechanical film
FFT	Fast Fourier transform
FSR	Free spectral range
FWHM	Full width at half maximum
HWHM	Half-width at half maximum
IR	Infrared
LED	Light emitting diode
LOD	Limit of detection
MI	Modulation index
OFDM	Orthogonal frequency-division multiplexing
OPO	Optical parametric oscillator
PA	Photoacoustic
PAS	Photoacoustic spectroscopy
PC	Personal computer

ppb	Parts per billion
ppm	Parts per million
PVDF	Polyvinylidene fluoride
QCL	Quantum cascade laser
QEPAS	Quartz-enhanced PAS
QSW	Quasi-square waveform
RAM	Residual amplitude modulation
SBR	Signal-to-background ratio
SNR	Signal-to-noise ratio
TDLAS	Tunable diode laser absorption spectroscopy
TDLPAS	Tunable diode laser PAS
UV	Ultraviolet
WM-PAS	Wavelength modulation PAS
WMS	Wavelength modulation spectroscopy
α	Spectral absorption coefficient $\left[\mathrm{cm}^{-1}\right]$
α_{jm}	j^{th} root of the derivate of the m^{th} Bessel function of the first kind divided by π
$\bar{y}_n$	Average of n samples of signal y
$\Delta\lambda_{\mathrm{FSR}}$	Free-spectral range of an interferometer [m]
$\Delta\omega_n$	FWHM of the power spectrum of the n^{th} acoustic resonance [Hz]
ΔL	Optical path length difference of an interferometer [m]
Δt	Sampling interval $[s]$
$\delta(f - f_0)$	Dirac's delta function at f_0
$\Delta\lambda$	Wavelength modulation amplitude of a laser [nm]
$\Delta\lambda_{CO2}$	Absorption linewidth HWHM of CO_2 [nm]
$\Delta\tilde{\nu}_{CO2}$	Absorption linewidth HWHM of CO_2 $[\mathrm{cm}^{-1}]$
γ	Adiabatic constant of gas
λ_L	Wavelength of a laser [nm]

λ_{jmq}	Wavelength of acoustic resonance [m]
$\lambda_{L,0}$	Center wavelength of a laser [nm]
$\mathbf{r_m}$	Microphone position vector $[m]$
ω	Angular frequency [rad/s]
ω_n	Angular frequency of n^{th} acoustic resonance [rad/s]
$\Phi(0)$	Incident radiant flux [W]
$\Phi(L)$	Transmitted radiant flux [W]
$\Phi_\lambda(0)$	Incident spectral radiant flux [W/nm]
$\phi_n(\omega)$	Phase of pressure wave [rad]
σ_λ	Spectral absorption cross-section $\left[\text{cm}^2/\text{molecule}\right]$
σ_{eff}	Effective absorption cross-section $\left[\text{cm}^2/\text{molecule}\right]$
$\sigma_y(\tau)$	Allan deviation
τ	Data acquisition time [s]
$\mathbf{r}$	Position vector [cm]
θ	Phase shift [rad]
φ	Azimuth angle
A	Absorptance
$A_n(\Omega)$	Complex amplitude of damped pressure wave [Pa]
$A_n(\omega)$	Complex amplitude of harmonic pressure wave [Pa]
c	Speed of sound [m/s]
$C_n(\mathbf{r_m}, \omega)$	Cell constant of PA detector $\left[\text{V}/\left(\text{cm}^{-1}\text{W}\right)\right]$
F_n	Normalized overlap integral
f_s	Sampling frequency $[Hz]$
f_{jmq}	Frequency of acoustic resonance [m]
$g(\mathbf{r})$	Normalized transverse intensity distribution of the light beam $\left[\text{cm}^{-2}\right]$
j	Index of radial resonance
J_m	m^{th} Bessel function of the first kind
L	Absorption path length [cm]

L_{res}	Length of the acoustic resonator [cm]
M	Number of atoms in a molecule
m	Index of azimuthal resonance
N	Number density of molecules $\left[\text{molecules/cm}^3\right]$
n	Index of resonance, $n = jmq$
$P\left(\mathbf{r}, t\right)$	Pressure wave [Pa]
$p_n(\mathbf{r})$	Dimensionless distribution function of the n^{th} acoustic eigenmode
q	Index of longitudinal resonance
Q_n	Quality factor of n^{th} acoustic resonance
$R(f)$	Value of an amplitude spectrum of a signal at frequency f
$R(k\Delta f)$	Value of a amplitude spectrum of a signal at index k $(k = 1, 2, \ldots, N)$
$R(n\Delta t)$	Value of a discrete time domain signal at index n $(n = 1, 2, \ldots, N)$
$R(t)$	Value of a time domain signal at time t
$R_T(f)$	Value of an amplitude spectrum of a truncated signal at frequency f
R_{res}	Radius of the acoustic resonator [cm]
$R_n\left(\omega\right)$	PA signal [V]
$S_m\left(\omega\right)$	Sensitivity of microphone $\left[\text{V/Pa}\right]$
T_m	Sampling time $[s]$
v_i	The i^{th} vibrational mode of a molecule ($i = 1, 2, 3$ for CO_2)
V_{res}	Volume of the acoustic resonator $\left[\text{cm}^3\right]$
z	Axial coordinate of cylinder [cm]
${\sigma_y}^2(\tau)$	Allan variance

Chapter 1

Introduction

Atmosphere contains a myriad of different gas components. Some of the gaseous trace constituents are toxic to breath, and some have a role in global warming. Therefore, it is relevant to be able measure the concentration of the molecules of interest. In addition to the environmental aspects, the monitoring of gases is important for example in modern medicine, and control of industrial processes.

Optical spectroscopy is a broad field of science which is used to study the interaction between light and matter. The concentration of a specific gas compound, among many other physical properties, can be revealed by using the methods of optical spectroscopy. The most common method of optical spectroscopy is a direct measurement of light that is transmitted through a gas sample. A part of the incident light is absorbed by the gaseous molecules, which are exited into higher energy levels. The concentration of the target molecules can be deduced by comparing the transmitted and incident powers of the light. The direct transmission measurement, however, typically lacks sensitivity that is required to detect trace gases at very low concentrations. To improve the sensitivity multipass techniques can be employed where the enhancement of the gas detection is achieved by increasing the interaction path length between light and matter[1] with the cost of increasing the complexity and size of the measurement unit.

The subject of this thesis is related to photoacoustic spectroscopy (PAS), which is a

branch of the more general field of optical spectroscopy. PAS is an established, robust, and sensitive method for trace gas monitoring. It is based on the photoacoustic (PA) effect that was first discovered by A. G. Bell[2]. In the PA effect modulated light is absorbed by gaseous molecules, which are excited to higher energy states. The energy of the absorbed light is converted to sound due to an increase in the temperature and pressure of the gas, which is caused by inelastic collisions between the molecules. The induced sound waves are usually further amplified using an echoic PA cell and detected with a microphone.[3] In principle PAS is a zero-background measurement technique because the PA signal is induced only when the target molecules are present. This is a considerable advantage as compared to the traditional direct transmission measurement.

In this work, new PA techniques are developed for the detection of gaseous carbon dioxide (CO_2), nitrogen dioxide (NO_2), and propofol ($C_{12}H_{18}O$). The ambient concentration of the greenhouse gas CO_2 is about 385 parts per million by volume (ppm)[4], whereas the typical mixing ratio of the atmospheric pollutant NO_2 is between $5 - 30$ parts per billion (ppb)[5]. Propofol is an intravenous sedative, used in surgical operations, whose residues are transported into a patient's exhaled breath where the concentration is also in the ppb range[6]. These low concentration levels emphasize the need for sensitive measurement techniques. Novel PA techniques are developed in this Thesis to fulfill these requirements.

Three of the five publications [Publ. 2,3,5] which are included into this Thesis, focus on NO_2 detection using a new type of microphone – the electromechanical film (EMFIT). The EMFIT films were recently introduced for the PAS of gases[7]. The EMFIT films allow the development of PA sensors that are low-cost, light-weight, and immune to ambient acoustic noise while their sensitivity is comparable to the sensitivities of commercial condenser microphones that are commonly used in PAS. In Publ. 1 it is shown that with a proper choice of modulation the sensitivity can be improved in wavelength-modulated PAS. Publ. 4 demonstrates the feasibility of PA detection of propofol in the ultraviolet (UV) spectral region of light.

The structure of this Thesis is divided into different chapters in such a way that in Chapter 2 the theory and basic concepts of PAS are presented. Chapter 3 is involved with the spectroscopic properties of CO_2, NO_2, and propofol. In Chapter 4 the essential experimental methods are presented in detail. The key results of the Thesis are reviewed in Chapter 5, and the final summary is given in Chapter 6.

Chapter 2

Photoacoustic spectroscopy

THEORY and basic concepts of PAS are presented in this Chapter. The absorption of light and generation of the induced pressure wave in a PA cell are explained in the first sections. The last section of this Chapter is devoted to different PA cell structures and microphone technologies that are used in the PAS of gases.

2.1 Fundamentals of photoacoustic spectroscopy

2.1.1 Photoacoustic effect

In the PA effect the absorption of modulated light results into a generation of a pressure wave. During absorption gas molecules are excited from a lower level to an energetically higher level, as presented in Fig. 2.1. The absorbed light energy is released as heat through subsequent nonradiative decay processes, i.e. multiple inelastic collisions between the molecules. As a result, the sample gas is heated locally within the interaction volume defined by a beam of light, and a pressure wave is induced which is detected with a microphone. The pressure wave can also arise from the photochemical dissociation of molecules in which the number density of particles is increased[8]. In addition to the acoustic detection of PAS, photothermal techniques,

such as the photothermal beam deflection method, can be used to measure the density and temperature variations of the gas by optical means[9].

The magnitude of the photo-induced pressure wavefront, which is detected in PAS, is directly proportional to the absorptance of light. Absorptance is described by the fundamental Beer–Lambert law which can be denoted in a generalized form for an optically thin gas sample as

$$A = \frac{\Phi(0) - \Phi(L)}{\Phi(0)} = 1 - \frac{\int \Phi_\lambda(0) \exp\left(-\sigma_\lambda NL\right) d\lambda}{\int \Phi_\lambda(0) d\lambda}$$
$$\approx \frac{\int \Phi_\lambda(0)\sigma_\lambda d\lambda}{\int \Phi_\lambda(0) d\lambda} NL \equiv \sigma_{\text{eff}} NL, \tag{2.1}$$

where $\Phi(0) - \Phi(L)$ is the absorbed radiant flux within an absorption path length L, and $\Phi(0)$ is the incident radiant flux. In addition, $\Phi_\lambda(0)$, σ_λ, and N are the incident spectral radiant flux, the spectral absorption cross-section of the molecule, and the number density of the molecules, respectively. On the right hand side of Eq. 2.1 the effective absorption cross-section σ_{eff} is defined as an average absorption cross-section, weighted by the spectral profile of the light source. For a spectrally narrowband light source, such as a laser, Eq. 2.1 reduces to the common representation of Beer-Lambert law where $\sigma_{\text{eff}} = \sigma_\lambda$.

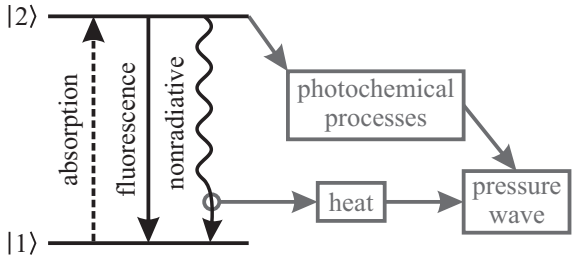

Figure 2.1 Schematic of an energy level diagram. Absorption of light ($|1\rangle \rightarrow |2\rangle$) is followed by radiative and nonradiative de-excitations ($|2\rangle \rightarrow |1\rangle$). Nonradiative and possible photochemical relaxation pathways produce a pressure wave which can be observed.[10]

2.1.2 Pressure eigenmodes of cylinder

The pressure wave that is induced through the PA effect, has typically a weak amplitude. Therefore, acoustic cavities are used to confine and amplify the pressure wave. The total pressure wave can consist of several partial waves, oscillating at different frequencies inside an acoustic cavity. The general expression for the total pressure wave that satisfies the acoustic wave equation, is [8]

$$P(\mathbf{r},t) = \sum_n A_n p_n(\mathbf{r}) \exp\left[i\left(\omega_n t - \theta_n\right)\right], \tag{2.2}$$

where A_n is a frequency-dependent complex pressure amplitude, $p_n(\mathbf{r})$ is a normalized pressure distribution function. Eq. 2.2 describes the behavior of a continuous pressure wave. In practice the pressure wave can also arise as an impulse response to a short pulse of light so that the oscillation frequency of an exponentially decaying PA pulse is given by $\Omega_n = \omega_n + ig_n$ where ω_n is the frequency of the continuous oscillation, and g_n is a damping factor that describes the decay of the acoustic pulse. In the following, only pressure waves that are excited using continuous wave (CW) light sources as the driving force for the acoustic wave, are considered. Then, the damping factor factor can be neglected, and $A_n = A_n(\omega)$. Furthermore, in Eq. 2.2 the factor θ_n is an additional phase angle, having contributions from an arbitrary detection phase [8] and other possible phase lags that can arise if the modulation frequency is high enough and comparable to the rate of nonradiative relaxations [11]. Usually in PAS, this extra phase shift can be disregarded since typical modulation frequencies are in the range of $10^2 - 10^5$ Hz, whereas nonradiative processes take place in $10^{-5} - 10^{-9}$ s in gases at normal pressure [10].

The oscillating pressure wave has antinodes at the walls of a PA cell due to the boundary conditions, which state that the pressure gradient must be zero at the walls. The most common cell structure used in PAS is a closed cylinder for which the time-independent solution is given by [12]

$$p_n(\mathbf{r}) = p_{jmq}(r,\varphi,z) = J_m\left(\frac{\pi\alpha_{jm}}{R_{\text{res}}}r\right)\cos(m\varphi)\cos\left(\frac{\pi q}{L_{\text{res}}}z\right). \tag{2.3}$$

Eq. 2.3 is the dimensionless pressure distribution function that represents an acoustic standing wave pattern in Eq. 2.2. The indices jmq define a specific resonance together so that j, m, q are the indices for the radial, azimuthal, and longitudinal resonances, respectively. The radius and the length of the resonator are R_{res} and L_{res}. In the radial part of the pressure wave of Eq. 2.3 the notation J_m is the m^{th} Bessel function of the first kind, whereas the solutions for the azimuthal and longitudinal modes are given by the the two cosine terms where φ and z are the azimuth angle and the longitudinal coordinate of the PA cell, respectively.

The second longitudinal [002] and radial [200] eigenmodes are illustrated as an example in Fig. 2.2. In general, the radial eigenmodes have lower pressure amplitudes at the walls of the cylinder than in the center, being 0.3 for the second radial mode, whereas the amplitude of the longitudinal modes remain the same at both ends of the resonator. However, usually radial modes tend to resonate better than the longitudinal ones which is discussed further in Section 2.2.

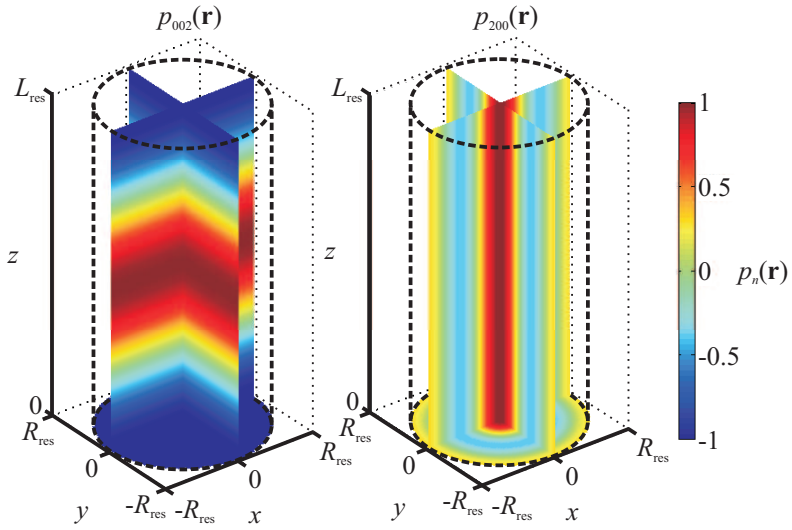

Figure 2.2 The second longitudinal $p_{002}(\mathbf{r})$, and the second radial eigenmode $p_{200}(\mathbf{r})$ of a cylindrical acoustic resonator, having a length L_{res} and radius R_{res}.

The acoustic resonance frequencies of a closed cylinder are[13]

$$f_{jmq} = \frac{c}{2}\sqrt{\left(\frac{\alpha_{jm}}{R_{\mathrm{res}}}\right)^2 + \left(\frac{q}{L_{\mathrm{res}}}\right)^2}, \tag{2.4}$$

where the first term describes the frequencies of both the radial and azimuthal resonances where α_{jm} is the j^{th} root of the derivate of the m^{th} Bessel function of the first kind divided by π. The second term is the frequency caused by the longitudinal resonance. The wavelength of the eigenmode is given through the relation $\lambda_{jmq} = c/f_{jmq}$. By inserting Eq. 2.4 into this relation, it can be seen that the wavelength of the eigenmode is a constant and is solely defined by the dimensions of the acoustic resonator and the order of the resonance. For example, a purely longitudinal eigenmode is described by the combination $n = jmq = 00q$, and the wavelength is $\lambda_{00q} = 2L_{\mathrm{res}}/q$. According to Eq. 2.4 the oscillation frequency is linearly dependent on the speed of sound c. The speed of sound is dependent on environmental parameters, such as the gas composition, temperature and humidity[14]. At 23°C in dry air[14] and nitrogen[15] atmospheres the speed of sound is about 345 m/s and 353 m/s, respectively. Some of the roots of the derivate of the first kind Bessel function are given in Table 2.1 which are required for the calculation of the resonance frequencies of the radial, azimuthal, and combinational modes. The first column ($m = 0$) in Table 2.1 can be used to calculate radial modes, and the first row ($j = 0$) gives azimuthal modes. All values with $[j, m] > [1, 1]$ describe combinational modes with contributions from both the radial and azimuthal parts. The first element with $\alpha_{jm} = 0$ gives $J_0 = 1$ in Eq. 2.3 with all values of r, describing radially independent pressure distribution.

Table 2.1. Values of α_{jm}, required for the calculation of acoustic resonance frequencies using Eq. 2.4. The indices j and m describe the radial and azimuthal resonances, respectively.

α_{jm}		m						
		0	1	2	3	4	5	6
j	0	0	0.5861	0.9722	1.3373	1.6926	2.0421	2.3877
	1	1.2197	1.6970	2.1346	2.5513	2.9547	3.3486	3.7353
	2	2.2331	2.7172	3.1734	3.6115	4.0368	4.4522	4.8600
	3	3.2383	3.7261	4.1923	4.6428	5.0815	5.5108	5.9325
	4	4.2410	4.7312	5.2036	5.6623	6.1103	6.5494	6.9811
	5	5.2427	5.7345	6.2111	6.6757	7.1304	7.5769	8.0163
	6	6.2439	6.7368	7.2166	7.6855	8.1454	8.5976	9.0431

2.1.3 Resonant mode of operation

The eigenmodes of the PA resonator can be excited by illuminating the cell with modulated light which is absorbed by the gas molecules, present inside the PA cell. The modulation of light can be accomplished by using wavelength or amplitude modulation. With amplitude-modulated CW light sources the modulation frequency must match the PA cell's resonance frequency. However, multiple acoustic resonances can be excited simultaneously with short laser pulses. In wavelength modulation a narrow laser line is swept twice across an absorption line during one modulation period, and the pressure wave is detected at the second harmonic of the modulation frequency. In this case the modulation frequency is set to the half of the resonance frequency of the PA cell. When CW light sources and sinusoidal modulation are used, the complex-valued amplitude of the pressure wave at the angular frequency of ω is

$$A_n(\omega) = \frac{i\omega}{{\omega_n}^2 - \omega^2 + i\dfrac{\omega_n \omega}{Q_n}} \frac{(\gamma - 1)\,\alpha L_{\mathrm{res}} \Phi(0)}{V_{\mathrm{res}}} F_n, \tag{2.5}$$

where ω_n, Q_n, γ, and V_{res} are the n^{th} resonance frequency of the cell, the quality factor, adiabatic constant of the gas, and the volume the PA resonator, respectively. Furthermore, F_n is a normalized overlap integral which describes the coupling between the light-induced heat source and the pressure eigenmode, and it is given by

$$F_n = \frac{\dfrac{1}{L_{\mathrm{res}}} \displaystyle\int g(\mathbf{r}) p_n(\mathbf{r}) dV}{\dfrac{1}{V_{\mathrm{res}}} \displaystyle\int |p_n(\mathbf{r})|^2 \, dV}, \tag{2.6}$$

where $g(\mathbf{r})$ is the transverse intensity distribution of the light beam inside the PA cell.[13] In order to maximize the pressure amplitude, the overlap integral must be maximized, i.e. the alignment of the beam of light, so that F_n is close to 1.

The line profile of the power spectrum of the acoustic resonance in Eq. 2.5, i.e. $|A_n(\omega)|^2$, is very close to a Lorentzian at high quality factors. The height and width of the profile are determined by the quality factor. At $\omega = \omega_n$ the magnitude

of the pressure wave in Eq. 2.5 is amplified by Q_n times as compared to the initial pressure wavefront. The quality factor of the resonance is defined through the ratio of the accumulated acoustic energy and the amount of energy that is lost during one period of oscillation, which is often described as

$$Q_n = \frac{2\pi \times \text{energy stored in mode } n}{\text{energy lost from mode } n \text{ in one period}} = \frac{\omega_n}{\Delta\omega_n}, \tag{2.7}$$

where $\Delta\omega_n$ is the width of the resonance profile, which is the full-width at half maximum (FWHM) value of the power spectrum or equivalently the $2^{-1/2}$ width of the amplitude spectrum.[13] The losses of the resonating acoustic wave can be divided into surface and volume losses which result from heat conduction, viscosity, and reflection losses at the walls of the PA cell. For example, near the boundaries of the resonator the tangential velocity component of the gas molecules is zero due to viscosity, dragging the propagating pressure wave.[3] The losses can be minimized to a certain extent by using hard and polished surfaces as the wall material of the resonator.

At the resonance frequency, the amplitude of the amplified pressure wave is purely real, as can be seen from Eq. 2.5. At other frequencies near the resonance the phase of the pressure wave is changed. The phase can be calculated in radians from

$$\phi_n(\omega) = \angle A_n(\omega) = \mathrm{Im}\left\{ \ln\left[A_n(\omega) \right] \right\}. \tag{2.8}$$

The magnitude and phase of the complex pressure amplitude, generated in the PA effect, are plotted in Fig. 2.3 according to Eq. 2.5 for an acoustic resonator having f_n and Q_n of 3.9 kHz and 50, respectively. The phase of the pressure wave changes from $-90°$ to $90°$. Usually in trace gas monitoring the magnitude of the pressure wave is of main interest since it gives the analyte concentration. However, for accurate concentration measurements with modulated CW light sources the resonant amplification of the pressure wave must be maintained. This can be compromised if the resonance frequency, given in Eq. 2.4, drifts due to possible changes in the speed of sound. However, the fact that the phase of the wave changes across the resonance, can be exploited to track the location of the resonance by using phase-sensitive detection.

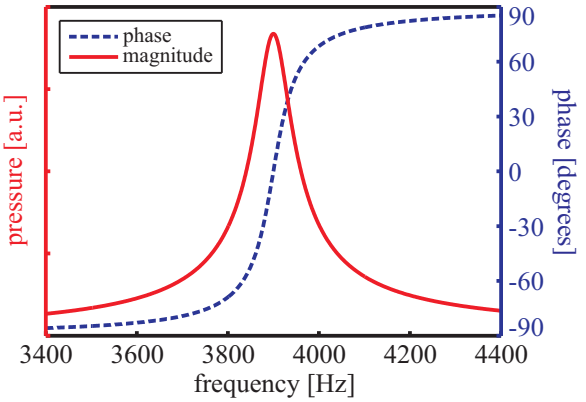

Figure 2.3 Magnitude and phase of the pressure wave, modeled according to Eq. 2.5 and Eq. 2.8, near an acoustic resonance, having $Q_n = 50$ and $f_n = 3.9$ kHz.

In pulsed photoacoustics, on the other hand, there is no need for active maintenance of the resonant amplification. A short light pulse excites an acoustically broadband pressure wavefront, which automatically resonates at all the eigenfrequencies of the PA cell, covered within the bandwidth of the induced wavefront [13,16]. At high enough pressure amplitudes, the location of the resonance can be directly interpreted from the measured amplitude spectrum, as opposed to the case of modulated CW excitation.

2.1.4 Non-resonant mode of operation

The complex-valued amplitude $A_n(\omega)$ in Eq. 2.5 describes also the non-resonant mode of operation where the PA cell is operated far away from its resonances, and usually so that $\omega \ll \omega_n$. In other words, the modulation frequency of the light source is much lower than any of the eigenfrequencies of the acoustic cavity, i.e. the acoustic wavelength is much larger than the PA cell dimensions. In this case the pressure distribution function $p_0(\mathbf{r}) = 1$ of Eq. 2.3, and it is independent on the location inside the cylindrical PA cell. The "resonance frequency" of this mode is $\omega_0 = 0$. The pressure amplitude of Eq. 2.5 is then reduced to*

$$A_0(\omega) = -\frac{i}{\omega}\frac{(\gamma-1)\,\alpha L_{\mathrm{res}}\Phi(0)}{V_{\mathrm{res}}}, \tag{2.9}$$

*For consistency, the subscript *res* is used in the equations to indicate the properties of a *resonator*, even though terms *cavity* or *cell* would be preferable in non-resonant mode of operation.

where the fraction $L_{\mathrm{res}}/V_{\mathrm{res}}$ is the cross-sectional area of the cavity just as in Eq. 2.5.

2.1.5 Photoacoustic signal

The pressure wave, which is induced in the PA effect and described by Eq. 2.2, is detected with a microphone which produces a proportional electrical output signal whose complex amplitude at the signal frequency ω is $R_n(\omega)$. The PA signal is the product between the microphone sensitivity $S_m(\omega)$ and the pressure amplitude at the location of the microphone[13]. Often, the PA signal amplitude is also described with the aid of a cell constant $C(\mathbf{r_m}, \omega)$ so that[10]

$$R_n(\omega) = S_m(\omega) P(\mathbf{r_m}, \omega) = C_n(\mathbf{r_m}, \omega) \alpha \Phi(0), \tag{2.10}$$

where the cell constant, or PA setup constant, is in units of $\mathrm{V}/\left(\mathrm{cm}^{-1}\mathrm{W}\right)$ giving the PA signal amplitude in volts[†]. If the pressure wave is detected with a large-area microphone, then the pressure amplitude $P(\mathbf{r_m}, \omega)$ in Eq. 2.10 should be taken as the integral average of the pressure that is exerted onto the whole area of the microphone membrane.

Using Eq. 2.5 and 2.9 the cell constants in resonant and non-resonant modes of operation are expressed as

$$C_n(\mathbf{r_m}, \omega) = S_m(\omega) \frac{i\omega}{{\omega_n}^2 - \omega^2 + i\dfrac{\omega_n \omega}{Q_n}} \frac{(\gamma - 1) L_{\mathrm{res}}}{V_{\mathrm{res}}} F_n p_n(\mathbf{r_m}), \tag{2.11a}$$

and

$$C_0(\mathbf{r_m}, \omega) = S_m(\omega) \frac{-i}{\omega} \frac{(\gamma - 1) L_{\mathrm{res}}}{V_{\mathrm{res}}}, \tag{2.11b}$$

respectively. The cell constant has primary contributions from the microphone sen-

[†]Sometimes the PA signal is given in units of pascals[13], which is the unit of the pressure wave amplitude. However, here the PA signal is defined as a measured electrical quantity.

sitivity, and the quality and dimensions of the acoustic resonator or cavity. In the resonant mode of operation the microphone position is important, and the microphone should be located at the antinode of the pressure distribution function $p_n(\mathbf{r})$. However, in the non-resonant case the microphone location is not that important since the pressure amplitude is constant everywhere inside the PA cell. Also, in the resonant mode the alignment of the light beam through the resonator has a crucial effect on the PA setup constant through the value of the overlap integral F_n. With a poor beam alignment the sensitivity of the measurement device is reduced. In fact, both the PA setup constants depend also on the method how the light source is being modulated. All the above equations have been derived assuming sinusoidal modulation. Different modulation techniques are discussed further in Chapter 4 and Publ. 1. In order to take into account the type of modulation, an additional proportionality factor could be added into Eq. 2.11.

As an important feature of PAS, in both the resonant and non-resonant modes of operation, it should be noted that the magnitude of the PA signal is inversely proportional to the modulation frequency and the cross-sectional area of the acoustic cavity. Furthermore, in theory lengthening of the cavity does not improve the sensitivity. This is a fundamental difference in favor of PAS over absorption spectroscopies. In conventional absorption spectroscopies the absorption signal is directly proportional the total light energy that is absorbed, and, therefore, high sensitivities are acquired by increasing the absorption path length, which easily results into bulky measurement devices. For example, in cavity-enhanced absorption techniques absorption path lengths of tens of kilometers can be acquired within a meter-scale measurement cell [1].

In non-resonant PAS it is possible to miniaturize the PA detector since a small-diameter PA cell and a low modulation frequency together give a large PA signal [17]. On the other hand, in the resonant case the sensitivity, as described by Eq. 2.11a, depends also on the Q_n factor, which scales approximately with the volume-to-surface ratio of the resonator [13]. Therefore, in order to improve the sensitivity the diameter of the resonator cannot be reduced indefinitely at the expense of diminishing Q_n. Furthermore, the demand for using a tightly focussed light beam sets a limit for reducing the PA cell diameter. [13]

2.2 Technological considerations

2.2.1 Photoacoustic cells

Photoacoustic cells are commonly categorized into resonant and non-resonant cells[3], which refer to the corresponding modes of operations as described in the previous sections. In practice, any PA cell can be operated in both resonant or non-resonant modes, and, therefore, it would be more appropriate to characterize only the mode of operation[13].

Resonantly excited cells

In the resonant mode closed cylindrical PA cells are the most common, where the radial, azimuthal, or longitudinal resonances are excited. Acoustic resonances are exploited in PAS to amplify the detected pressure wave and, thereby, to enhance the measured PA signal above the electrical noise level of common microphones. In order to maximize the coupling of light to acoustic energy, the light beam must be aligned carefully. The strength of the acoustic wave depends also on the Q_n factor of the resonance which is inversely proportional to the losses experienced by the propagating pressure wave (see Eq. 2.7). The best achieved Q_n factor is about 1000 for a polished cylinder, optimized for the excitation of the first radial mode[18]. Typically, the Q_n factors are smaller for the longitudinal modes than for the radial ones. The reason for the diminished amplification factors of longitudinal resonances is that the longitudinal modes experience larger viscous surface losses than the radial modes, as the pressure wave drags along the surfaces of the closed cylinder.

Helmholtz resonator is another type of acoustic resonator quite commonly used in PAS[19–23]. Helmholtz oscillations occur in acoustic cavities which have smaller dimensions than the acoustic wavelength and have a narrow opening into free space[23]. The gas inside the capillary is an equivalent to a mass that oscillates on a spring, which is represented by the compressible gas inside the cavity[20]. A common example is an open bottle which resonates when air is blown by the neck. In PAS of gases the benefits of Helmholtz resonators are that the pressure distribution is constant inside the cavity, making it easy to couple light into the acoustic resonance, and shape of

the cavity does not have a significance[23]. However, quality factors of Helmholtz resonators are typically quite low and they are operated at low frequencies, which makes them prone to ambient acoustic noise. Quality factors ranging from 5 to 20 have been reported[20,23].

Spherical cells have also been used in PAS[24–26]. In principle radial modes of a spherical resonators can have higher Q_n factors, as compared to those of a cylinder having the same radius, because of smaller surface losses of the propagating pressure wave[26]. Q_n factors as high as $2000-10000$ can be realized for spherical resonators[13]. However, spherical resonators are rarely used for trace gas monitoring. In order to obtain the maximum pressure amplitude the microphone has to be placed near the center of the sphere[26], which expectably introduces additional losses and lowers the Q_n factor close to those of ordinary cylindrical resonators. Also, as a consequence of the conservation of the energy, the amplitude of a spherical pressure wave decreases as r^{-1}, whereas a cylindrical pressure wavefront shows a $r^{-1/2}$ dependence[27], which makes cylinders more favorable over spheres in PAS if the pressure amplitude is detected at the circumference of the PA cell. In addition, a collimated cylindrical laser beam is coupled more conveniently to a radial mode of a cylinder.

In addition to amplifying the PA signal using acoustic resonances, further enhancement can be achieved with optical multipass- and cavity-enhanced techniques where the effective absorption path length is increased[22,26,28–35]. As a result, the energy density that is deposited inside the PA cell, is increased. However, the multipass- and cavity-enhanced techniques usually require laser sources which exhibit highly directional beam propagation. Extremely high sensitivities can be achieved by placing the PA cell inside a laser resonator, which enables the measurement of gas absorption coefficients in the low 10^{-10} cm^{-1} range[29]. With extracavity PA systems optically non-resonant multipass cavities are used because of the practical difficulty of maintaining optical resonances of high-finesse cavities. Optically non-resonant Herriott-type multipass cavities with spherical mirrors are commonly used in PA detectors[31–33]. The beam pattern inside such cavities possess cylindrical symmetry of a rotational hyperboloid[36,37]. If radial resonances are excited, the PA cell radius can be tailored so that the beam family lies close the inner surface of the PA cell[31]. A more efficient excitation of radial modes in multipass cavities can be achieved using an optical cavity with cylindrical mirrors, which produces a Lissajous beam pattern with overlapping beams at the center of the cavity[26]. On the other hand, Herriott-type resonators can be used

to excite longitudinal resonances of an open pipe-resonator[32,33]. Multipass excitation of longitudinal acoustic modes can also be effectively achieved using perpendicular or transverse illumination, in which the light beam can be introduced radially, through a small aperture, into a closed PA cell having reflective walls[34]. Similar radial illumination can be used in a Helmholtz resonator[22]. Alternatively, open windowless PA cells can be placed between high-reflectivity mirrors as discussed in Publ. 3 and Ref.[38]. The benefit of such windowless PA cells is that the PA background, which originates from light absorption at the windows and walls, can be avoided[31,38]. In addition, a usual method to avoid the interfering PA background is the combination of wavelength modulation spectroscopy and second harmonic detection of the PA signal. However, this is actually related to the detection method of the PA signal rather than to the PA cell design and, therefore, is further discussed in Chap. 4.2.

Differential PA cells have been successfully implemented for the elimination of both the PA background and ambient acoustic noise[3,19–21,39–41]. These PA cells have been designed for both the resonant[19–21,39,40] and non-resonant[3,41] modes of operation.

Non-resonantly excited cells

In general, the term non-resonant refers to any scheme of PA detection where resonances of the PA cell are not employed to enhance the acoustic wave.

Usually in the non-resonant mode of operation the dimensions of the PA cell are much smaller than the acoustic wavelength of the pressure wave that is induced through the PA effect. In this case the pressure increases and decreases homogeneously in the PA cell at the same oscillation frequency as the modulation frequency of light. Commonly the non-resonantly operated PA cells are cylindrical, even though the shape is not as crucial as in the resonant mode. As discussed in Section 2.1.5, small-diameter PA cells and low modulation frequencies are used in the non-resonant mode to maximize the sensitivity. However, the total volume of a non-resonant PA cell is an important parameter which cannot miniaturized indefinitely because the sensitivity of a microphone depends on size of the gas volume, surrounding the microphone membrane[42,43].

The excitation of the spatially independent acoustic mode of a closed PA cell is just one example of the non-resonant operation. There are also PA cells where acoustic wavefronts, having shorter wavelengths than the dimensions of the PA cell, are exited and

detected without exploiting the resonant amplification by the PA cell[21,38,44]. Calasso et al. detected the broadband, free-field pressure wavefront which was induced by a short laser pulse[44]. In other studies PA cells have been designed where the pressure wavefront was focussed onto a microphone using acoustic mirrors[21,38,45].

2.2.2 Microphones

The most common microphones, which have been used in PAS of gases, include condenser, electret, electromechanical film, quartz tuning fork, and optical cantilever microphones. The schematics of these microphones are shown in Fig. 2.4.

The selection of a proper microphone depends on its use. In the trace gas analysis at low concentrations such a microphone should be selected which gives the best signal-to-noise ratio (SNR) for the PA signal[44]. The main characteristics of a microphone, affecting the SNR, are its sensitivity, measurement frequency bandwidth, noise characteristics, and stability[42]. In some applications the prize of the microphone can be important. All microphones have in common that they respond mechanically to a changing pressure and output a proportional electric signal.

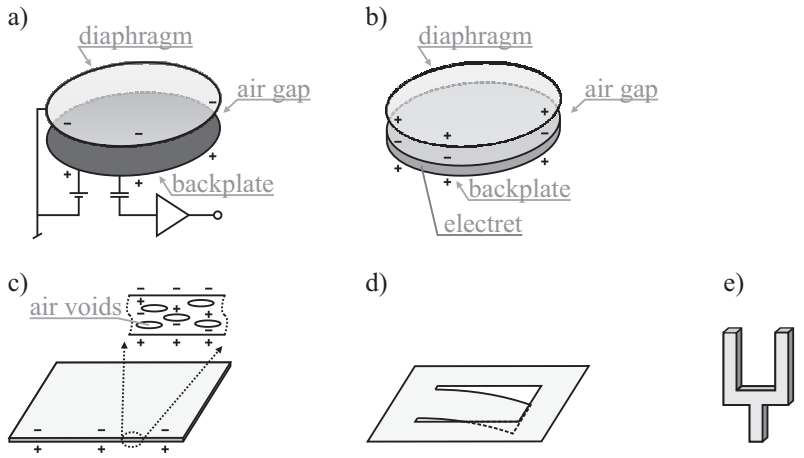

Figure 2.4 Schematics of microphones used in PAS. The conventional microphones include condenser **(a)**, and electret microphones **(b)**. New microphones, which have been introduced-for PAS of gases, are the electromechanical film **(c)**, the optical cantilever microphone **(d)**, and the quartz tuning fork **(e)**.

Condenser microphone

A condenser microphone is shown in Fig. 2.4 a. A condenser microphone has a rigid back plate and a thin metal diaphragm, which is tightened by the microphone enclosure like a drum. The pressure-sensitive front diaphragm and the rigid back plate have an air gap between them, constituting a capacitor. An external polarization voltage, typically about 200 V, is applied across the metal diaphragm and the back electrode. As the diaphragm moves due to a changing incident pressure wave, the capacitance of the charged condenser microphone changes which results into a fluctuating output voltage difference between the electrodes.[42,44] The sensitivity and the measurable frequency bandwidth depends on, among other things, the stiffness of the diaphragm, the diaphragm damping by the moving air in the gap (so called breathing effect[43]), and the diaphragm mass and area.[44] For example, the sensitivity of an oscillating condenser microphone, in units of mV/Pa, is directly proportional to the surface area and inversely proportional to the distance between the electrodes. Thus, the sensitivity of the microphone increases with an increasing surface area. However, at the same time the increased mass of the oscillating diaphragm causes the high-frequency response to drop. In general, there is a trade-off between the sensitivity and measurable bandwidth[44].

Electret microphone

Electret microphones differ from condenser microphones in that respect that they do not require a high external polarization voltage. The charging of the front diaphragm and the back plate is achieved by placing a permanently pre-polarized dielectric layer, i.e. an electret layer, on top of the back plate and in between the two electrodes as shown in Fig. 2.4 b. The polymer electret material possesses a uniform distribution of trapped charges near the surface facing the air gap, which produces the required electric fields into electret and the air gap of the microphone. Regardless of the differences in their constructions, the operation of an electret microphone is similar to that of a condenser one: An incident pressure wave causes a change in the capacitance which results into a measurable output voltage. Miniature electret microphones are commonly used for example in hearing aid devices.[42,44]

Electromechanical film

The electromechanical film[46–51] is a flexible polymer film which has a permanent internal electric charge. The electromechanical film is also known as EMFi of EMFIT film (EMFIT Ltd.). The films have air voids or bubbles inside them as shown in Fig. 2.4 c, which makes them compliant to external pressure changes. The internal polarization is introduced through corona charging during the manufacturing.[46,48] The most sensitive EMFIT films developed are approximately 70-μm-thick sheets. Thin metal electrodes on the both sides of the film allow the extraction of the pressure-induced electric signal. The metal electrodes have to be thin enough in order not to remarkably increase the mass of the moving film. The best sensitivities have been achieved with electrodes which are less than 300 nm thick.[50]

The electromechanical film was invented in the late 1980's, and it was originally intended to be used as an acoustic transducer and receiver in audio and ultrasonic applications[46,47]. Due to the extremely broadband and flat acoustic response of a single film ($0 - 300$ kHz) and relatively high sensitivity (~ 1 mV/Pa), the film is applicable to the PAS of gases. However, the EMFIT film is a rather new microphone technology for the gas-phase photoacoustic measurements. The use of EMFIT films is demonstrated in the publications related to this thesis. In the history of the PAS of gases, the closest resemblance to the electromechanical film was introduced by Claspy et al. who used an aluminized electret film microphone that was wrapped around a holey brass cylinder[52]. Other types of early film microphones include for example ceramic piezoelectric, polymer polyvinylidene fluoride (PVDF), or ceramic piezo-PVDF composite microphones. Due to their high stiffness and acoustic impedance, piezo transducers are better suited for the PAS of liquids and solids than gases[53,54].

In comparison, the EMFIT film is approximately $2 - 3$ orders of magnitude more sensitive for the acoustic measurements in air than ceramic piezoelectric or PVDF transducers. However, composite piezo-PVDF ceramics fall only by a factor of 4 behind the EMFIT film.[50] However, as demonstrated by Hillenbrand et al.[49] and in Publ. 3 the sensitivity of an EMFIT transducer can be enhanced by layering multiple films together. Layering of n films together increases the sensitivity n times. At the same time the electromechanical resonance frequency is reduced by a factor of n since the total mass of the transducer is increased by the same amount.[49] Still, as shown in Publ. 3, for five layers the resonance remains above 40 kHz which is usually far

beyond the operation frequencies of common PA detectors. Different applications of EMFIT films for the PAS of gaseous NO_2 are presented in Publ. 2,3,5.

Optical cantilever microphone

The optical cantilever microphone was introduced for PAS of gases in the early 2000's and has since been used in a number of studies [43,55–64]. The optical cantilever-type microphone consists of a flexible pressure-sensitive, high-purity crystalline silicon cantilever whose typical dimensions (length×width×thickness) are 4 mm × 2 mm × 5 μm, and of an optical interferometer unit. The cantilever microphone is presented in Fig. 2.4 d without the optical readout unit. The optical interferometer detects the door-like bending motion of the cantilever, and additional signal processing is used to convert the cantilever displacement to a voltage signal. The main difference to the conventional membrane-based electrical microphones is the optical readout. In addition, a freely oscillating cantilever does not experience the damping breathing effect, as the condenser and electret microphones do due to the closely-spaced electrodes. Because of its flexibility, the cantilever exhibits a very high response at low frequencies. The magnitude of the cantilever motion can be about 100 times larger than the movement of the membrane of a conventional microphone under the same pressure. Cantilever displacements as small as 2 pm can be detected. [43] The electric noise of the interferometric cantilever-type microphone can be negligible. Then, the noise of the optical pressure sensor is defined by the random Brownian bombardment of the cantilever by the surrounding gas molecules. [62] In this case acoustic resonances of a PA cell cannot be used to enhance the performance of a PA detector because the signal and the Brownian noise are acoustically amplified by the same amount, keeping the SNR unaffected. For the same reason the mechanical resonance of the cantilever, which usually occurs below 1 kHz, does not improve the SNR. For these reasons only small-diameter PA cell, operated in the non-resonant mode at low frequencies, are employed with the cantilever-type optical microphone.

Quartz tuning fork

The tuning fork is made of piezoelectric quartz, and it consists of two prongs connected by a bridge as shown in Fig. 2.4 e. They are commonly used as timing oscillators in

electronic clocks[65] but have also been used as force detectors in near-field optical microscopy, atomic force microscopy etc.[66]. The tuning fork can also be used as a resonant microphone. Only the symmetric bending mode of the tuning fork is piezoelectrically active. Therefore, in quartz-enhanced PAS (QEPAS) where quartz tuning forks are used as the pressure transducer[11,65,67–71], a laser beam is usually focussed through the center of the prongs. In vacuum the resonance frequency of the tuning fork is about 32.76 kHz, and the quality of the resonance can exceed 10^5. In air at atmospheric pressure the corresponding values are about 32.75 kHz and 10^4, giving about 3 Hz for the $2^{-1/2}$ linewidth. A pressure-dependence of the resonance of 9.6 mHz/Torr has been reported.[67] The resonance of the quartz tuning fork can be excited just the same way as the resonances of any PA cell, either using pulsed or modulated CW light sources. An additional PA signal enhancement of about $7 - 10$ times has been achieved by placing two micro-resonator tubes, half a wavelength apart from each other, close to the tuning fork, so that the resonance of the micro-tubes matches with that of the tuning fork[67,69,71]. The benefits of the tuning fork in PAS are its high resonance frequency, which makes it practically immune to interfering ambient acoustic, its small size, and low cost. Sample cell volumes as small as a few mm^3 can be used.[67] However, the small size of the gap of the tuning fork requires that lasers, outputting tightly focusable beams, must be used which easily raises the overall price of the PA system. Furthermore, optical multipass cavities might be difficult to employ.

Chapter 3

Spectroscopic properties of the gases

SPECTROSCOPIC properties of the three gases, carbon dioxide (CO_2), nitrogen dioxide (NO_2), and propofol ($C_{12}H_{18}O$), studied in this work are reviewed in this Chapter.

3.1 Carbon dioxide

Carbon dioxide is a triatomic, linear molecule with a center of inversion. A linear molecule composing of M atoms has $3M - 5$ normal modes of vibration, whereas a non-linear molecule possesses $3M - 6$ normal modes.[72] Thus, CO_2 has a total of 4 vibrational modes, which are the symmetric stretch (v_1), bending (v_2), and asymmetric stretch (v_3) vibrations. The bending mode is doubly degenerate which makes the fourth normal mode.[73]

The spectral* absorption cross-section of CO_2 is shown in Fig. 3.1. The absorption band is centered at 1575.34 nm or 6347.85 cm^{-1}.[74] It corresponds to a combinational overtone transition where the CO_2 molecule is excited from its ground level to vibrate in the v_1 and v_3 modes by three and one quanta, respectively[75]. A general require-

*The term *spectral* is often omitted.

ment for an optically active transition is that the transition must accompany a change in the dipole moment of the molecule[72]. The symmetric stretch mode of CO_2 alone is not infrared (IR) active, since the non-polarity of the molecule remains unaffected during the vibration. However, the combination with asymmetric stretch makes the afore-mentioned overtone transition electric dipole allowed. The rotational fine structure in the spectrum arises from transitions between the different rotational states, associated with the ground and excited vibrational states. The $R(18)$ ro-vibrational transition at 6361.25 cm^{-1}, the second strongest line in the R branch, was measured in Publ. 1. The peak cross-section of the line is 7.4158×10^{-23} cm^2. The line was probed by scanning the wavelength of a longitudinally single-mode distributed-feedback (DFB) diode laser back and forth across it. This results into a periodical changes in the absorption of light and into a pressure wave through the PA effect as discussed in Chap. 2.1.

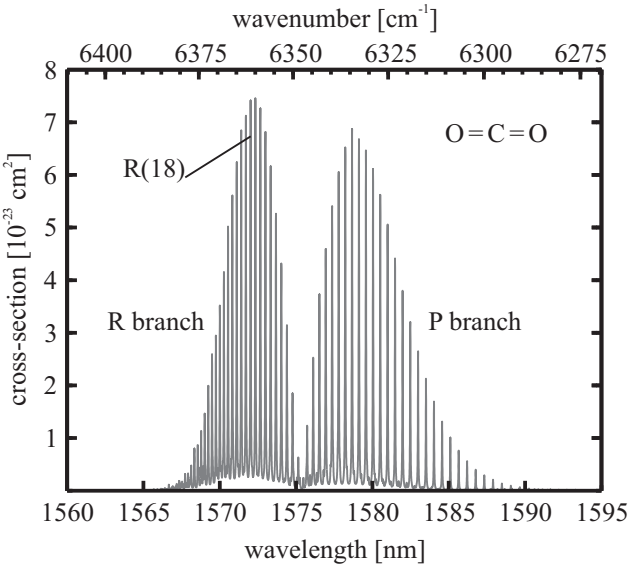

Figure 3.1 Absorption cross-section spectrum of gaseous CO_2 in the 1.6 μm region. The vibration-rotation spectrum composes of discrete rotational lines, forming the P and R branches of the band. The spectrum was modeled using data from HITRAN2008 molecular spectroscopic database[76] at the pressure and temperature of 1 atm and 23°C, respectively. The $R(18)$ line was probed in Publ. 1 with narrow-linewidth wavelength-tunable diode laser.

3.2 Nitrogen dioxide

Nitrogen dioxide is a non-linear triatomic molecule with a permanent dipole moment. All the three vibrational modes are IR active, and they can be probed by PA means e.g. with quantum cascade lasers (QCL)[77,78]. NO_2 has also a strong absorption band in the visible part of the electromagnetic spectrum between $250 - 700$ nm as shown in Fig. 3.2. The spectrum consists of several different electronic transitions[79]. The fine structure, seen above 350 nm, arises from a plethora of Doppler-broadened ro-vibrational transitions. There are many PA applications where the absorption in the visible range has been used because of the multitude of available laser sources[52,80–85] and light-emitting diodes[86,87] (LED) in this region.

The absorption band extends into the UV region as can be seen from Fig. 3.2. However, below 415 nm the NO_2 molecule is photodissociated[79,89,90]. The fragment products are a ground state NO molecule and O atom. As described in Eq. 3.1, the O radical may further react with an NO_2 molecule or form an ozone (O_3) molecule with oxygen. The laboratory experiments of this work were carried out in nitrogen atmosphere, so the latter reaction is not observed. However, considering the PA applications, Eq. 3.1b is still relevant. The thermal energy released in Eq. 3.1b is about 25 % less than the absorbed energy in Eq. 3.1a.[3,7] At low NO_2 concentrations the O_2 formation reaction

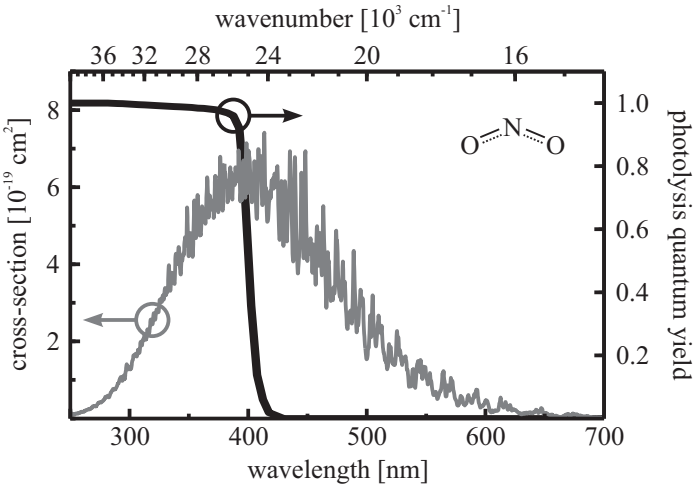

Figure 3.2 Absorption cross-section spectrum of gaseous NO_2 in the visible part of the electromagnetic spectrum[88] (grey), and the quantum yield of photodissociation[89] (black).

is slow, and takes place in between 30 μs and 2 ms, which results into a pronounced reduction of the PA signal at high modulation frequencies and at shorter wavelengths than the dissociation limit of NO_2.[7] This is the reason why excitation wavelengths longer than 415 nm are preferred in the PA detection of NO_2. Above 415 nm and at the normal pressure the non-radiative relaxation pathways of electronically excited NO_2 dominate over the fluorescence decay, giving approximately 90 % of the absorbed energy as heat as discussed in Publ. 5.

$$NO_2(^2A_1) + h\nu \rightarrow NO(X^2\Pi) + O(^3P) \tag{3.1a}$$

$$O + NO_2 \rightarrow NO + O_2 \tag{3.1b}$$

$$O + O_2 + M \rightarrow O_3 + M \tag{3.1c}$$

The PA detection of NO_2 at the wavelengths of 436 nm, 473 nm, and 453 nm, is demonstrated in Publ. 2,3,5 using the new EMFIT film microphone. Because of the low cost of the EMFIT microphone, a special emphasis is paid in the last publication (Publ. 5) to replace the previously used, expensive laser sources with modern cost-effective high-power LEDs.

3.3 Propofol

Propofol (2,6-diisopropylphenol; $C_{12}H_{18}O$) is an aromatic hydrocarbon, consisting of a benzene ring to which two isopropyl and a hydroxyl groups are attached. The UV absorption cross-section spectrum of gas-phase propofol is presented in Fig. 3.3. According to the numerical modeling of the electronic transitions of propofol at Cambridge University, the long wavelength part of the absorption spectrum of propofol is composed of two electronic transitions whose maxima are about 6 nm apart from each other. The two maxima can be seen in Fig. 3.3 at 269 nm and 276 nm. Both the transitions occur between π and π^* molecular orbitals of the aromatic part of the molecule. The absorption spectrum measured from the liquid phase[91,92] is is very close to that measured from the gas-phase in Publ. 4.

The PA detection of propofol is presented in Publ. 4 using optical parametric oscillator (OPO) laser system whose emission wavelength can be tuned between $210 - 2300$ nm. The broad tunability of the laser improves the spectral identification of broadband absorbers from other background absorbers. In exhaled breath acetone is an expected interfering compound which could compromise specific and unambiguous detection of propofol. However, acetone absorbs light also at longer wavelength in the UV than propofol so that these can in principle be separated from each other.

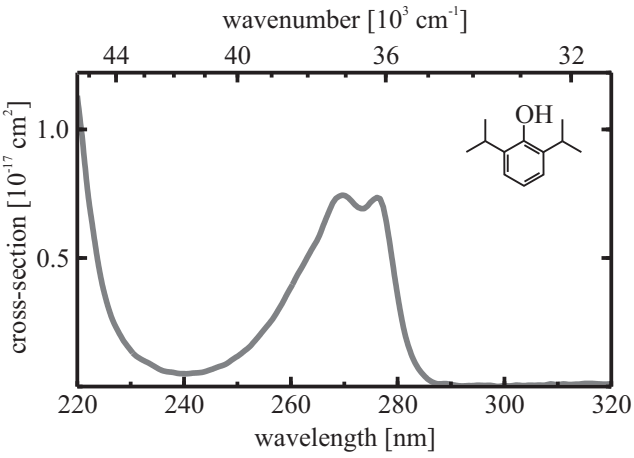

Figure 3.3 Absorption cross-section spectrum of gaseous propofol (data from Publ. 4).

Chapter 4

Experimental methods

THE experimental and data processing methods, used in the appended publications, are presented in detail in this chapter. The measurable electric signals are commonly analyzed using Fourier analysis which is explained it the first section.

4.1 Fourier analysis of signals

Noisy time domain signals are commonly analyzed in the frequency domain where the overall random noise is distributed into a wide spectrum. This enables the detection of weaker signals in the frequency domain than in the time domain. Fourier transforms form the basis for the data analysis of all the attached publications.

4.1.1 Fourier transforms

Any infinitely long periodic, i.e. continuous, signal having the fundamental frequency of f_0, can be represented as a Fourier series which consists of sinusoids that oscillate at the fundamental frequency and its harmonics $n \times f_0$ ($n = 1, 2, 3, \ldots$). Each frequency component has a unique complex amplitude that describes its magnitude and phase.

Instead of calculating the infinitely long series of a time domain signal, it is common to retrieve the complex amplitudes of different frequency components from the amplitude spectrum, which can easily be calculated with a computer.[93,94]

The amplitude of a noisy signal can be retrieved by using the Fourier transform which is the connection between the time and frequency domain representations of the signal. The Fourier transform pair between the frequency and time domain representations of an infinitely long signal is

$$R(f) = \mathscr{F}\{R(t)\} = \int_{-\infty}^{\infty} R(t)\exp(-j2\pi ft)\ \mathrm{d}t \tag{4.1a}$$

$$R(t) = \mathscr{F}^{-1}\{R(f)\} = \int_{-\infty}^{\infty} R(f)\exp(j2\pi ft)\ \mathrm{d}f, \tag{4.1b}$$

where $\mathscr{F}$ and $\mathscr{F}^{-1}$ are the Fourier and inverse Fourier transform operators, respectively. The amplitude spectrum composes of negative and positive frequency bands, which are replicas of each other. The energy of the signal is distributed equally on the both sides of the spectrum. Since the two sides of the spectrum are identical, usually only the positive frequencies are of interest.

In practice the signal $R(t)$ is sampled, or measured, for a finite period of time (T_m) using a digitizer, which takes discrete sample points from the signal in time intervals of Δt or at a sampling frequency of f_s. A signal of N samples has a discrete Fourier transform (DFT) pair, which are approximations to Eq's 4.1 and can be defined as*

$$R^{\Delta t}_{T_m}(k\Delta f) = \Delta t \sum_{n=0}^{N-1} R(n\Delta t)\exp(-j2\pi nk/N) \tag{4.2a}$$

$$R^{\Delta f}_{f_{\max}}(n\Delta t) = \Delta f \sum_{k=0}^{N-1} R(k\Delta f)\exp(j2\pi nk/N) \tag{4.2b}$$

*Often the DFT pair in Eq's 4.2 is defined for arbitrary data without the integration variables Δt and Δf, and with a normalization factor of $1/N$ in Eq. 4.2b.[93] (p. 407) These definitions, however, yield the same results as Eq's 4.2 since the product $\Delta t \times \Delta f = 1/N$. The conventions of Eq. 4.2 are used in this work since they illustrate better the connection to Eq. 4.1.

where $R(k\Delta f)$ and $R(n\Delta t)$ are the discrete samples of the spectrum and the signal, respectively.[94] The data points in the spectrum of Eq. 4.2a are spaced $\Delta f = 1/T_m = 1/(N\Delta t)$ apart from each other. The discrete frequencies reside within a band of $[0, 1/\Delta t]$ at $k\Delta f$ where the index $k = 0, 1, \ldots, N$. Both the frequency and time domain representations of the signal compose of the same number of N data points. For a large number of N the calculation of the DFT spectrum can be slow, which hinders the data analysis. In 1965 Cooley et al.[95] introduced a computational method, called the fast Fourier transform (FFT), to calculate the amplitude spectrum of a discretely sampled signal effectively. In this method N is an even number and a certain power of two. The data points with $k = 0, \ldots, N/2 - 1$ represent the positive frequency side of the FFT spectrum, and those with $k = N/2, \ldots, N$ form the other side of the FFT spectrum. Because N is an even number and one the points are used for the zero frequency component, the positive and negative sides of the FFT spectrum are not fully symmetric.

4.1.2 Continuous signals

An infinitely long sinusoidal time domain signal, having the frequency and amplitude of f_0 and $R = R(f_0)$, respectively, is defined by

$$R(t) = R\cos\left(2\pi f_0 t\right). \tag{4.3}$$

The Fourier transform spectrum $R(f)$ consists of two peaks $R/2 \times \delta(f - f_0) + R/2 \times \delta(f + f_0)$ where $\delta(f - f_0)$ is the Dirac's delta function.[94] The true amplitude of the infinite sinusoid, R, is twice the peak amplitude that is measured in the frequency plane at f_0. When the sinusoidal signal is observed only for a finite time period of T_m, it can be shown that the positive side of the spectrum of such a truncated signal is given by

$$R_{T_m}(f) = \mathscr{F}\left\{R_{T_m}(t)\right\} = \frac{R}{2} \times T_m \,\mathrm{sinc}\big(\pi\left(f - f_0\right)T_m\big). \tag{4.4}$$

The effect of the signal truncation is that the signal peak in the frequency plane will be distorted and broadened from the ideal Dirac's delta function into a sinc profile.[94] At $f = f_0$ the value of the sinc function is 1, and a numerically obtained value for the FWHM in the frequency plane is $1.207/T_m$ (Hz). Usually, the observation or sampling time is so large that the distortion of the signal peak in the frequency plane is not observed and the weak side lobes of the sinc function are buried into the noise. As an important effect of the signal truncation, it can be seen from Eq. 4.4 that the signal amplitude due to the sampling is now $RT_m/2$ instead of the amplitude $R/2$ of an infinitely long signal. Clearly, the spectrum needs to be normalized with the sampling period if signals, measured with different sampling periods, are to be compared.

The comparison $R_{T_m}(f_0) = R_{T_m}{}^{\Delta t}(f_0)$, according to Eq's 4.2a and 4.4, yields for the true amplitude spectrum

$$\begin{aligned} R(k\Delta f) &= \frac{2\Delta t}{T_m} \sum_{n=0}^{N-1} R(n\Delta t) \exp(-j2\pi nk/N) \\ &= \frac{2}{N} \sum_{n=0}^{N-1} R(n\Delta t) \exp(-j2\pi nk/N), \end{aligned} \tag{4.5}$$

Eq. 4.5 gives the corrected discrete amplitude spectrum of a truncated continuous signal as if it represented the spectrum of an infinitely long signal. Yet, each frequency component is smoothed by the sinc instrumental function of signal truncation. The measured signal amplitude in Eq. 4.5 is no longer dependent on the measurement time T_m as in Eq. 4.4. However, it should be noted that Eq. 4.5 gives correct results only for undamped periodic signals. The FFT methods, presented in this chapter, are used in Publ. 1,3,5 in the analysis of continuous PA signals. The analysis of pulsed PA signals is slightly different and is presented in Sect. 4.1.3.

It is required for the accurate measurement of the amplitude of a continuous signal that the sampling frequency f_s, the measurement time T_m, or the signal frequency f_0 are chosen so that $f_0 = k\Delta f = k \times f_s/N = k/T_m$ with a certain value of k. In other words, the total measurement time consists an integer number signal periods, i.e. $T_m = k/f_0$. Then, the k^{th} data point in the spectrum coincides with the signal frequency giving the true signal amplitude $R(f_0) = R(k\Delta f) = R$. This point is illustrated in Fig. 4.1. The

infinitely long wave (—) of Fig. 4.1a was sampled at $f_s = 1$ MHz and with $N = 2^{13}$. The frequency of the wave was set to about $f_0 = 4028.32$ Hz so that the sampled signal was composed of exactly 33 periods. Then, in the FFT spectrum of Fig. 4.1b the $k = 33$ data point matches with the signal frequency, giving the correct peak amplitude of the broadened sinc function. In practice, the record length is usually much larger, giving a better resolution to the FFT spectrum than in Fig. 4.1b, which is 122 Hz.

The gray curves in Fig. 4.1b show how an erroneous amplitude measurement can occur if the signal frequency does not match with any of the data point frequencies. The energy of the signal is spread out to several frequency components, and the data points lie on the envelope of the sinc profile. The effect of spreading is called spectral leakage[96]. However, the spectral leakage can be reduced to a certain point by using an additional windowing function for the time domain signal. The window functions can also be used reduce spectral leakage in signal averaging and in the presence of interfering peaks that are nearby the measurement frequency.[96] With the proper choice of the signal frequency, as already discussed, all the energy is concentrated into a single frequency component, and the nearby data points (**o**) reside at the zeros of the sinc function, which is called critical or optimal sampling[94].

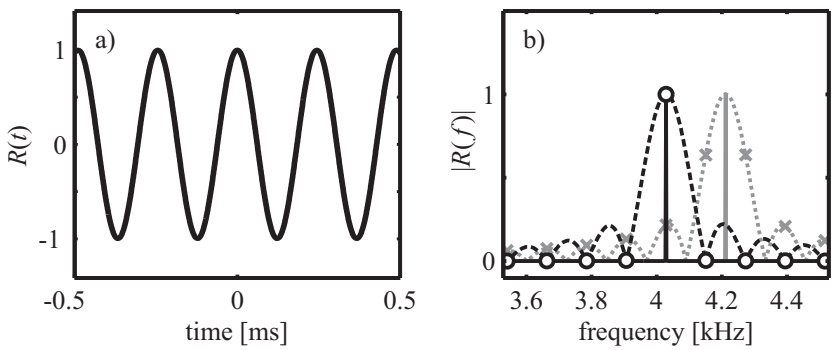

Figure 4.1 Illustration of optimal sampling of a continuous signal. **(a)** An "infinitely" long continuous wave (—) in the time domain, whose **(b)** Fourier transform gives the narrow Dirac's delta peak (—) at about $f_0 = 4028$ Hz. By sampling the signal for a finite period of time, a discrete FFT spectrum is obtained where the data points (**o**) lie on the envelope of a sinc function (- - -). With a proper choice of the sampling frequency f_s, measurement time T_m, or the signal frequency f_0 the discrete signal consists of and integer number of periods. Then, the peak amplitude of the signal is measured correctly from the resulting FFT spectrum (**o**). Non-optimal sampling results into a distorted FFT spectrum (✖) and incorrect amplitude measurement.

In principle, by using the idea of critical sampling it is possible to construct a frequency-multiplexed, or multitone, PA detection system where multiple light sources are modulated at the neighboring frequencies, e.g. under the same resonance profile of the PA cell. In the field of signal processing this type of usage of multiple optimally-spaced frequencies is known as orthogonal frequency-division multiplexing[97,98] (OFDM), and is commonly used in broadband data transmission systems[99]. In PAS an alternative, and more complex but common, way is to use multi-wavelength PA detection system which comprises of multiple PA cells, which are used separately to detect the different PA signals[100]. In addition to OFDM, time-division multiplexing can also be used in PAS so that the different gas components are measured sequentially one after another in the same PA cell. However, then the measurements have to be made from a static gas sample, or fast enough from a flowing sample so that the relative concentrations do not change.

4.1.3 Pulsed signals

An infinitely long, decaying sinusoidal signal represents the impulse response of a PA cell when one of its acoustic eigenmodes are exited for example with a short laser pulse. The damped oscillator is defined ($t \geq 0$) as[13]

$$R(t) = R\cos\left(\sqrt{(2\pi f_0)^2 - g^2} \times t\right)\exp\left(-gt\right), \tag{4.6}$$

where g is the damping factor. When g is negligible compared to the center frequency, the frequency shift in the argument of the cosine can be disregarded, and the power spectrum of is a Lorentzian centered at f_0. Schäfer et al.[16] have derived an analytical expression for the whole amplitude spectrum of a windowed ($0 \leq t \leq g^{-1}$) PA signal pulse, which can be calculated by applying Eq. 4.1a to Eq. 4.6. For long observation times ($T > g^{-1}$) the amplitude of the exponentially decaying oscillator, at f_0 in the frequency plane, is[8]

$$R_T(f_0) = \frac{R}{2g} = \frac{R}{\Delta\omega_0} = \frac{R}{2\pi\Delta f_0}, \tag{4.7}$$

where Δf_0 is the FWHM of the Lorentzian in the power spectrum. For a decaying

PA signal pulse, which oscillates at a certain resonance of the PA cell, the value Δf_n was defined through Eq. 2.7 as $\Delta f_n = f_n/Q_n$. Hence, the damping factor of a PA signal is related to the width of the acoustic resonance through $g = g_n = \pi\Delta f_n = \pi f_n/Q_n = \omega_n/(2Q_n)$. Similarly as with the continuous signals, the comparison of Eq's 4.2a and 4.7 yields the following expression for the spectrum:

$$R(k\Delta f) = 2\pi\Delta f_0 \times \Delta t \sum_{n=0}^{N-1} R(n\Delta t)\exp(-j2\pi nk/N). \tag{4.8}$$

The difference between the equations of the continuous (Eq. 4.5) and the damped signal (Eq. 4.8) is that the peak amplitude of the continuous signal needs to be normalized with the data record length N, whereas that of the damped signal must be multiplied with the width of the line profile $\Delta\omega_0 = 2\pi\Delta f_0$. In addition to giving the correct initial amplitude of the damped oscillation, the benefit of using Eq. 4.8 is that possible long-term changes in the width of the resonance, i.e. in the quality factor of the resonator, are eliminated so that the peak amplitude is the same in all cases. Still, the SNR, and thus the achievable detection limit, at f_0 is affected by Δf_0 because Eq. 4.8 scales also the noise of the FFT spectrum.

With the damped pulses the data record length N and the sampling frequency f_s of the measured signal should be chosen so that the resolution of the spectrum is adequate to correctly interpret both height and the width of the line profile. However, an upper limit is set for these two parameters by the digitizer used. If the spectral resolution of the FFT spectrum has to be enhanced, a method called zero-padding can be used, in which extra zero-value data points are added to the end of the decayed signal.

Sometimes pulsed signals are measured as a series of periodically repeating disturbances within a single measurement window. In PAS this is encountered if high repetition rate lasers are used. In some cases the repetition rate can be tuned to match the resonance frequency of a PA cell, which results into a quasi-CW PA signal. Optimally, the peak amplitude of the FFT spectrum at the resonance frequency is $\pi/2$ times as large as in the CW excitation[81]. The train of PA pulses can also be measured in a non-resonant PA cell. Usually the vibrational relaxation time is very short compared to the repetition period of the laser pulses. Then, a single laser pulse, having the duration in the ns range, excites a short bipolar pressure wavefront with a broad frequency bandwidth, which depends also on the diameter of the laser beam[44].

The temporal behavior of the pressure wavefront that propagates radially away from the laser beam, can be approximated as a derivate of a Gaussian pulse[38], rather than by Eq. 4.6. The duration of the acoustic pulse can be in the μs range for laser beam sizes in the mm range. The FFT spectrum of the train of individual pulses, detected in a non-resonant PA cell, composes of peaks, which are separated by the repetition rate of the laser and whose amplitudes follow the spectral envelope of a single pulse. Instead of measuring the fundamental of the laser repetition rate, a larger PA signal can be measured by detecting some of the higher-amplitude harmonics.[38]

4.2 Modulation techniques

In wavelength modulation spectroscopy[101] (WMS), and also in its photoacoustic relative WM-PAS,[102,103] a targeted IR absorption line of a gas molecule is usually probed with a narrow tunable semiconductor laser whose wavelength is scanned periodically across the line. Longitudinally single-mode diode lasers and QCL's are ideal for WM-PAS in the IR spectral region[†] in the sense that their emission linewidths are typically less than a thousandth of the absorption linewidth and because of the possibility to tune the laser wavelength.

Wavelength modulation of a single-mode DFB diode laser can be accomplished by directly modulating the injection current that is fed through the P–N junction. The flow of electric current through the laser induces changes in the refractive index and temperature of the active region of the laser, which both cause the emission wavelength to change. At low modulation frequencies of the injected current thermal effects are the dominant cause for the wavelength tuning[104]. However, thermal processes are typically slower than the movement of current, causing a delay between the current and wavelength modulation[103,105]. The wavelength of the diode laser, λ_L, is usually modulated sinusoidally across the absorption line but, in general, can be modulated with any type of function f, so that

$$\lambda_L(t) = \lambda_{L,0} + \Delta\lambda f\left(\omega t + \theta\right) \tag{4.9}$$

[†] Also multimode Fabry–Perot type lasers, forced into the single-mode emission by the combination with external cavities are used in WM-PAS.

where λ_0 and $\Delta\lambda$ are the center wavelength during the modulation period and the wavelength modulation amplitude, respectively. The amplitude is directly proportional to the modulation current, and it is usually smaller than or in the range of the absorption linewidth. The phase shift θ is the delay between current and wavelength modulation. The spectroscopic diode-laser-based technique where the wavelength is modulated according to Eq. 4.9, is actually called tunable diode laser absorption spectroscopy (TDLAS), and its PA counterpart is tunable diode laser PAS (TDLPAS). Because the absorption line is scanned twice in a modulation period, the signal is formed at twice the modulation frequency 2ω and at other higher harmonics. In the actual WMS the center wavelength $\lambda_{L,0}$ is additionally scanned slowly back and forth the absorption line with a large-amplitude ramp modulation. This type of multi-tone modulation results into a temporally changing absorption signal which can be represented as a combination of different high-order derivates of the line profile of the absorbing molecule[101,106].

The reason why the sinusoidal modulation, as described in Eq. 4.9, is usually used in WM-PAS and TDLPAS is that it is simple to use and gives nearly the best SNR. In fact, there are other modulation waveforms than the sinusoidal one, e.g. the triangular waveform, which give a higher absorption signal, as will be shown in Publ. 1. The SNR in an optical transmission measurement is not determined only by the electric noise of the detector but is also affected by interference or etalon effects. A typical WMS measurement setup consist of various optical components, in addition to the laser source and the detector. At the interfaces of the windows, and lenses etc. the laser beam is partly reflected, and the reflections easily impinge onto the optical detector giving rise to a fine-pitch fringe pattern or noise which continuously changes as the laser wavelength is modulated. The triangular and sinusoidal waveforms give the smallest etalon noise and, thus, the best SNR if the fringes exceed the electric noise of the detector.[107] However, in the WM-PAS the induced pressure wave, which is measured, originates from the whole volume of the PA cell in such a way that the fine-pitch interference effects are averaged out, and the overall noise is ruled by the electric noise of the microphone. Then, the choice of a proper modulation waveform is not restricted to the basic waveforms, such as the sine or triangle.

In Publ. 1 different wavelength modulation waveforms are compared using the TDLPAS technique. The four waveforms studied are shown in Fig. 4.2. These include the afore-mentioned sinusoidal and triangular waveforms, and in addition the quasi-

square waveform (QSW) and the shaped waveform. The three-level, staircase-type QSW waveform was proposed for the WMS by Iguchi [107] and experimentally implemented by Fried et al. [108] and Pilgrim et al. [109]. The shaped modulation waveform was introduced in Publ. 1 as a new type of wavelength modulation waveform which mimics the Voigt absorption lineprofile and produces a purely sinusoidally varying absorption with all the signal energy concentrated into the fundamental frequency. On the other hand, the QSW waveform maximizes the time spent at the center of the absorption line and produces a square wave second harmonic signal [108]. A square wave signal with a 50% duty cycle has the largest amplitude at its fundamental frequency, and it is $4/\pi$ times the amplitude of the sinusoidal absorption waveform, i.e. 27 % larger, despite the fact that part of the signal energy is distributed also to the higher harmonics [93]. Thus, ideally the QSW waveform is the optimum choice for PAS. The differences and the usability of the different waveforms are discussed further in Chap. 5 and Publ. 1.

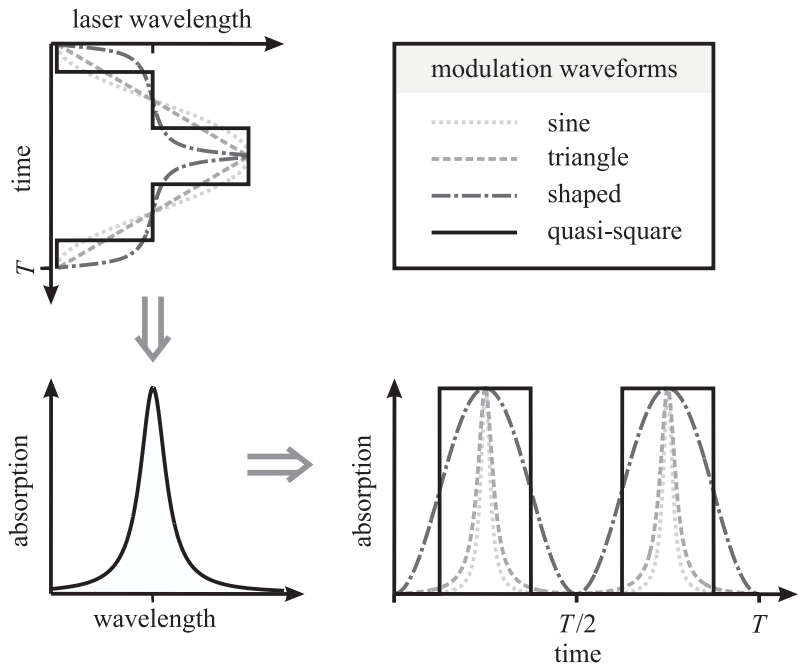

Figure 4.2 Wavelength modulation waveforms studied in Publ. 1. In the wavelength modulation spectroscopy the targeted absorption line is probed with narrow tunable laser whose wavelength is scanned periodically across the line. The shaped modulation waveform was introduced in Publ. 1 as a new type of waveform which mimics the Voigt absorption line and produces a purely sinusoidally varying absorption.

All the wavelength modulation waveforms produce PA signals whose fundamental frequency is twice the modulation frequency. Any periodic function $\lambda_L(t)$ which changes according to $\lambda_L(t + T/2) = -\lambda_L(t)$ about its average value, consists only of odd harmonics[93] (p. 297). All the modulation waveforms in Fig. 4.2 fulfill this criterion, and they are periodic in time with the period of T. Thus, if the modulated laser beam is absorbed for example at the PA cell windows, whose absorption spectrum changes usually linearly within a narrow wavelength band in the IR, the background PA signal is observed only at frequencies $1/T$, $3/T$, $5/T$ etc. if the background absorption is strong enough. All the PA signal waveforms are periodic and have the fundamental frequency at $2/T$. In addition to the wavelength modulation, the current modulation induces also an inherent modulation to the optical power that is emitted by the semiconductor laser. Assuming that the power–current (P–I) curve is linear within the range of the current modulation, the residual amplitude modulation (RAM) does not produce a PA signal at $2/T$ but again only at the odd harmonics. Thus, because there is no background signal at the second harmonic, it is said that the TDLPAS, and the WM-PAS as well, is a background-free measurement technique. However, this can be compromised if the P–I curve or the background absorption change nonlinearly but usually this is not a problem.

4.3 Phase-sensitive detection

The amplitude of a signal is a complex number $R = |R| \exp(i\phi) = |R| \left[\cos(\phi) + i \sin(\phi)\right]$ where $|R|$ and ϕ are the magnitude and phase of the signal, respectively. In the complex plane the amplitude is represented as a vector $\mathbf{R} = (|R|, \phi)$ as shown in Fig. 4.3. The real and imaginary parts of the amplitude are $\mathrm{Re}\{R\} = |R| \cos(\phi)$ and $\mathrm{Im}\{R\} = |R| \sin(\phi)$.

Phase-sensitive detection refers to a technique where the real and imaginary components of an input signal can be measured with respect to the phase of a reference signal. This is usually achieved using an electronic device called a lock-in amplifier. Essentially, the lock-in amplifier is a device that is capable of extracting the Fourier component of a noisy signal at the reference frequency[110]. It multiplies the input signal with in-phase and out-of-phase reference signals and gives the integral averages of the two components at a narrow band around the reference frequency, while rejecting

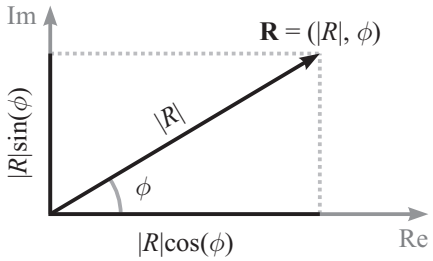

Figure 4.3 Vector representation of a complex-valued signal amplitude.

most of the noise at other frequencies[111,112]. The strengths of the in-phase and out-of-phase, i.e. quadrature, components can be used to calculate the magnitude and phase of the original signal. On the other hand, once the signal is digitized the FFT routine provides the same information that is required to calculate the magnitude and phase of the signal component. The benefit of using the FFT method is that it is faster than the lock-in technique if information is required at broad range of frequencies, instead of the narrow band at the reference frequency[113]. Actually, the complex-valued FFT spectrum, as described in Eq. 4.2a, gives the required information for all the measured frequencies simultaneously. An additional benefit of the digital signal processing is that possible temperature-dependent phase shifts, which can be present in the analog lock-in devices, are minimized[113].

Phase-sensitive detection using lock-in amplifiers is widely implemented in different PA applications to improve the SNR, or the signal-to-background ratio (SBR) of the PA signal. In this work, the phase-sensitive PA detection, based on the FFT method, is presented. The schematic of the set-up used in Publ. 5 is shown in Fig. 4.4. The second longitudinal mode of the PA resonator is excited at the center of the cell so that two EMFIT film microphones produce opposite-phase PA signals when NO_2 gas molecules are present inside the cell. The two PA signals are digitized using a two-channel digitizer (DAQ), and the data are transmitted in the digital form to the personal computer (PC). A LabVIEW program controls the signal generator and data acquisition parameters and computes the FFT spectrum of the acquired PA signal. The program retrieves the complex number of the FFT spectrum at the modulation frequency. The modulation frequencies from the signal generator are set based on the sampling rate f_s and record length N of the digitizer so that the criterion of critical sampling is fulfilled (see Sect. 4.1.2. In Publ. 5 sampling parameters of $f_s = 1$ MHz and $N = 2^{19}$ were used, resulting into a measurement time and frequency resolution

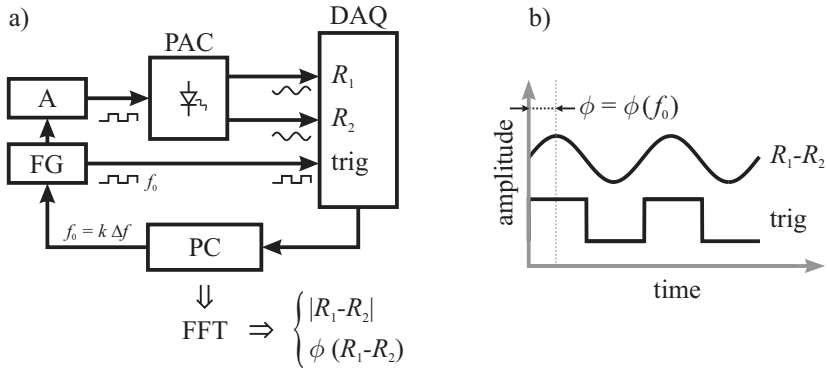

Figure 4.4 (a) Schematic of the phase-sensitive detection setup used in Publ. 5. The function generator (FG) and current amplifier provide square wave modulated current to the LED light source inside the PA cell (PAC). The modulation frequency of the FG is preset by a computer program running on the PC. Data acquisition unit (DAQ) is triggered by the FG, the signals R_1 and R_2, picked up by two microphones in the PAC, are digitized. FFT algorithm is used to acquire the magnitude and phase angle of the difference PA signal. **(b)** Visualization of the difference PA signal and its phase angle with respect to the start of the measurement window.

of about $T_m = 0.5$ s and $\Delta f = 2$ Hz, respectively. The phase of the PA signal is calculated by applying Eq. 2.8 to the complex number of the FFT spectrum at the index of the modulation frequency ($k = 2001$ when $f_0 = 4$ kHz). The high sampling rate is required for the possibility to fine tune the detection phase of the PA signal, which can be done by removing extra data points from the beginning of the data vector and by zero-padding the end of the vector by the same number of points so that the critical sampling is maintained.

4.4 Resonance tracking

In the resonant mode PAS the frequency drifts of either the modulation or resonance frequency can introduce errors into the measurement of the gas concentration, as already discussed in Sect. 2.1.3. The phase sensitive detection method, introduced in the previous section, can be exploited to avoid the possible measurement errors which are due to the frequency offset between the modulation and resonance frequencies, i.e. $f_0 - f_n$. The goal in the resonance tracking is to maintain the resonant amplification of the excited pressure wave at all times. This is obtained by keeping $f_0 = f_n$, regardless of the changes in the measurement conditions.

In the resonant mode of PAS both the phase angle and the magnitude of the PA signal are dependent on the difference $f_0 - f_n$. As it was shown earlier in Fig. 2.3, the PA signal magnitude is maximized when $f_0 - f_n = 0$. At the same time the phase angle is zeroed, provided that the measurement setup does not introduce additional phase shifts between the PA signal and the triggering signal. Because the PA signal magnitude is also dependent on the concentration of the analyte molecule, according to the Beer–Lambert's law of absorption, the magnitude is not a good parameter to monitor the frequency difference $f_0 - f_n$. Furthermore, the PA signal magnitude is a symmetric function of $f_0 - f_n$ so that it does not give unambiguous information about whether the frequency difference is positive or negative. On the contrary, the PA signal phase ϕ is a better measure of the frequency difference since it changes monotonically across the resonance as shown again in Fig. 4.5 b. Near the resonance the change is fairly linear. If the slope of the curve is predetermined, the measurement of the PA signal phase gives direct knowledge about the frequency correction that is required in order to maintain the modulation frequency f_0 at the PA cell's resonance f_n. When the resonance frequency of the PA cell drifts due to the changes in the speed of sound, the location of f_n on the frequency axis shifts but the profile of the phase curve remains unchanged. Provided that f_0 does not change remarkably within one measurement period, then the PA system can keep up with the shifting resonance. Prior to each measurement sequence the modulation frequency of the light source should be corrected to a value $k\Delta f \approx f_0 - \phi_0/(\mathrm{d}\phi/\mathrm{d}f)$ according to the parameters of the previous measurement f_0 and ϕ_0 while maintaining k as an integer so that the critical sampling of the PA signal is not compromised.

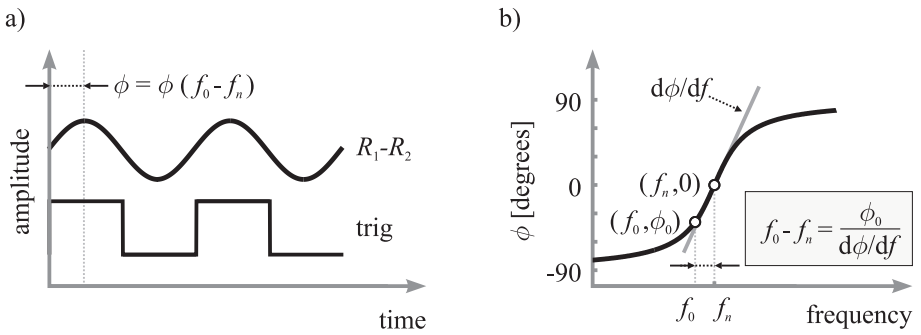

Figure 4.5 Resonance tracking of the PA cell from the phase of the PA signal. **(a)** The time domain PA signal and its phase. **(b)** The phase ϕ changes linearly near the PA cell's resonance frequency f_n. By knowing the value for the slope, the measured PA signal phase $\phi(f_0)$ can be used to drive the modulation frequency f_0 back to the drifting resonance f_n.

Chapter 5

Results and discussion

The key results of this Thesis will be presented and discussed in this Chapter. Supplementary material that has not been shown in the five publications, are also presented. The results of Publ. 1 are reviewed in Sect. 5.1. The results of the three publications 2, 3, and 5, all of which deal with the developed EMFIT-film-based PA sensors, are combined and compared in Sect. 5.2, and Sect. 5.3 gives insight on the resonance tracking method introduced in Publ. 5. The last section is devoted to the results of the PA technique presented in Publ. 4 for the sensing of propofol.

5.1 Tunable diode laser photoacoustic spectroscopy

In Publ. 1 different wavelength modulation waveforms were studied for the use in TDLPAS. The waveforms, as presented in Sect. 4.2, were the QSW, shaped, triangular, and sinusoidal waveforms. The TDLPAS measurement set-up consisted of a single-mode fiber-coupled DFB diode laser, the temperature and current controllers of the laser, a cantilever-type PA sensor, and a power meter. The laser emitted radiation near the $R(18)$ rotational line of CO_2 target gas whose half-width at half maximum (HWHM) linewidth of the pressure-broadened Lorentzian was $\Delta\tilde{\nu}_{CO2} = 0.0714\ \mathrm{cm}^{-1}$ or $\Delta\lambda_{CO2} = 17.6$ pm. The current injected through the DFB diode laser was mod-

ulated at amplitudes between $0 - 34$ mA about the DC value of 165 mA where the average emission power was 30 mW. The current was fine-tuned to that value so that the center wavelength of the laser coincided with the absorption maximum of the $R(18)$ rotational line. The lasing threshold of the laser was about 15 mA. According to the wavelength tuning parameter of the laser of 7.6 pm/mA, the maximum current modulation amplitude corresponds to a maximum wavelength modulation amplitude $\Delta\lambda_L = 260$ pm. Normalized with the HWHM of CO_2, this yields a calculated maximum modulation index of $\mathrm{MI} = \Delta\lambda_\mathrm{L}/\Delta\lambda_\mathrm{CO2} = 14.8$.

The FFT spectra, acquired with the different modulation waveforms using a MI of 10, are shown in Fig. 5.1. The background-free second harmonic PA signal peak is observed at 140 Hz. At such a high MI a large portion of the whole PA signal energy is distributed to the higher harmonics with the sinusoidal and triangular modulation waveforms which diminishes the second harmonic PA signal. In addition, a large-amplitude fundamental peak can be observed at 70 Hz which originates from the large power modulation of the laser and which has contributions from the light absorption both by the PA cell windows and CO_2 molecules. On the other hand, it can be seen from Fig. 5.1d that the FFT spectrum produced by the shaped waveform, tailored for the specific absorption line shape and MI, does not have a significant fundamental component and most of the PA signal energy is concentrated to the second harmonic frequency of 140 Hz as expected. By varying the modulation indices of the differ-

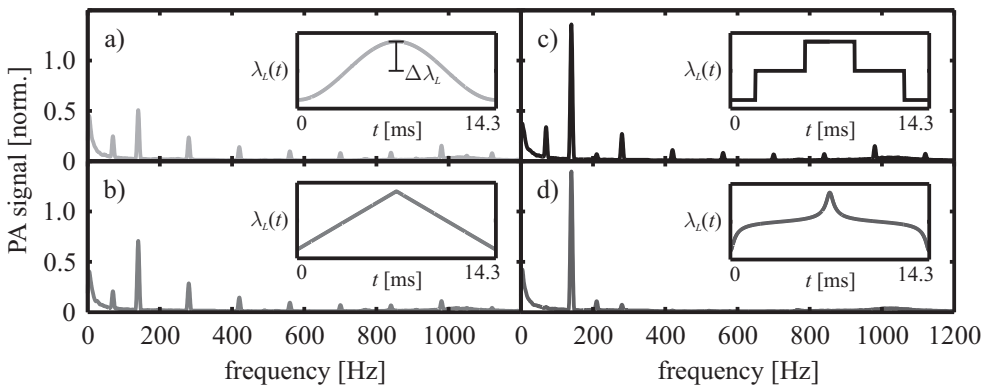

Figure 5.1 Photoacoustic amplitude spectra measured with different modulation waveforms, which are the **(a)** sinusoidal, **(b)** triangular, **(c)** quasi-square (QSW), and **(d)** shaped waveforms. The insets show one period of each modulation waveform at $f = 70$ Hz. The second harmonic PA signals are detected at 140 Hz. (Data from Publ. 1)

ent waveforms curves displayed in Fig. 5.2 were recorded. The separate points are measured data, and the solid curves were obtained from computer simulations.

The four waveforms produce different PA responses as shown in Fig. 5.2. The measured data of the sinusoidal, triangular, shaped, and QSW waveforms show PA signal maxima at 2.2, 3.0, > 8, and 5.0 with relative amplitudes of 1.00, 1.12, 1.42, and 1.57, respectively. Conventionally, the sinusoidal modulation waveform is used in PAS due to its simple use but evidently the other waveforms give an improved response. The achieved results for the sinusoidal and triangular waveforms are similar as in earlier studies[107,114,115]. The novel shaped waveform gives rise to a nearly pure sinusoidal signal whose amplitude is saturated at large MI's. However, the measured response of the QSW modulation waveform differs from the previous findings[107–109]. According to the simulations carried out here and in Iguchi's work[107], the QSW waveform should produce a pure square-wave PA signal whose magnitude is independent on MI at large values. The expected saturation level of the PA signal is 1.84. Yet, the measured data points deviate from the simulated curve. The amplitude of a square wave signal is by a factor of $4/\pi$, or about 27 % larger than that of the sinusoidal signal[93]. This is approximately the difference between the simulated saturation levels of the second

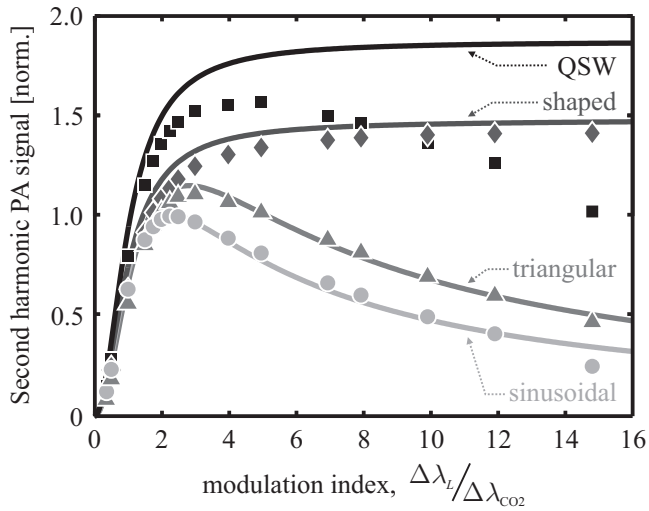

Figure 5.2 Second harmonic PA signals measured (points) and modeled (curves) with different modulation waveforms as a function of modulation index, i.e. the amplitude of laser wavelength modulation divided by the HWHM of the absorption line of CO_2. (Data from Publ. 1)

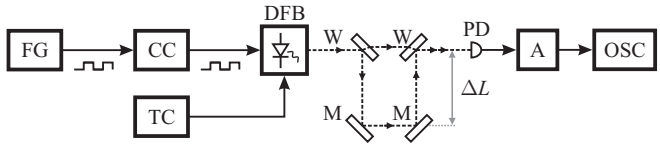

Figure 5.3 Mach–Zender interferometer for measuring impulse response of the DFB diode laser. The DFB diode laser is driven with step modulation current through a current controller (CC). The interfering beams are detected with a photodiode (PD) whose electric signal is amplified (A) and recorder with an oscilloscope (OSC).

harmonic signals produced by the shaped and QSW waveforms. Actually, the same difference is also observed at very low MI's between the PA responses of the sinusoidal and QSW waveforms since near the absorption line center the change of the absorption is fairly linear. Because the measured PA responses of the waveforms, other than the QSW, behave as was simulated, it would be expected that the wavelength tuning characteristics of the QSW waveform are different from the other waveforms.

In order to study the impulse response of the DFB diode laser and its wavelength tuning characteristics a Mach–Zender type interferometer setup, shown in Fig. 5.3, was built. The setup is identical to the PA measurement setup, as shown in Publ. 1, but the PA detector has been replaced with the optical interferometer. The interfer-

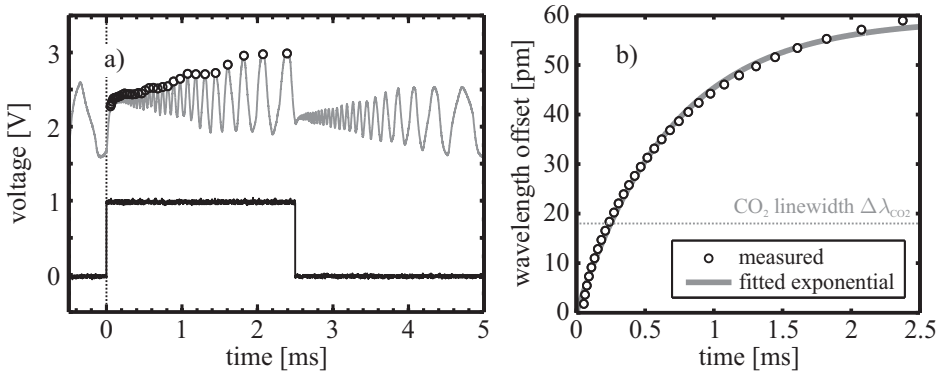

Figure 5.4 Delayed wavelength tuning of the DFB diode laser used in Publ. 1. **(a)** Oscilloscope trace of the interference pattern (gray) recorded with the Mach–Zender interferometer, having a free spectral range of 1.8 pm, during the step modulation of the QSW waveform (black). **(b)** The wavelength tuning as a function of time as interpreted from the interferogram. The 1/e time constant of the wavelength tuning is about 600 μs, whereas the laser power level sets within 30 μs. The horizontal level shows the HWHM linewidth of CO_2, which is 18 pm at normal pressure and temperature conditions.

ometer splits the laser beam (dashed line) into two different beams which experience different propagation delays. The optical path length difference between the two interferometer arms was $\Delta L = 0.67$ m, which results into a free-spectral range (FSR) of $\Delta\lambda_{\mathrm{FSR}} = {\lambda_L}^2/(2\Delta L) = 1.8$ pm. The recorded oscilloscope trace is shown in Fig. 5.4a where the laser current was modulated using 100 Hz QSW modulation. After the positive edge of modulation step at $t = 0$ the laser power (gray curve) changes and sets to the higher level within 30 μs. The transient oscillation of the laser power is interference, and it occurs because of the wavelength of the laser tunes after the impulse. There are 32 observable periods in the interferogram within the 2.5-ms-long quarter period of the QSW waveform. Because each period in Fig. 5.4a correspond to the FSR of the interferometer, the interferogram can be used to deduce the timely behavior of the wavelength tuning. The cumulative sum of the number of periods, multiplied by the FSR, yields the wavelength modulation amplitude or the wavelength offset from the average value, which is plotted in Fig. 5.4b. The wavelength tunes exponentially with a 1/e time constant of 600 μs. The wavelength modulation amplitude is about 60 pm. The 1 V modulation step, applied to the current controller (CC in Fig 5.3), corresponds to 20 mA current modulation amplitude. Thus, according to the tuning parameter, the expected wavelength modulation amplitude would be about 150 pm if the wavelength tuning was ideal and instantaneous. The observed wavelength amplitude is less than half of the expected value at the 100 Hz fundamental modulation frequency. The horizontal line shows for reference the HWHM value of CO_2 absorption line, which was 17.6 pm. Because of the limited response of the DFB diode laser, the QSW waveform does not produce an ideal square wave PA signal but rather a distorted square wave where each corner is rounded to an exponential, and the modulation amplitude is reduced. The result is that the second harmonic PA signal with the QSW waveform is less than that of the modeled ideal square wave response as was seen in Fig. 5.2. This is a new finding in WM-PAS which emphasizes that the optimum PA response is not necessarily obtained by using the QSW modulation. However, this is the case only with lasers that exhibit slow wavelength tuning relative to the duration of the modulation period. The DFB diode lasers can have tuning times from less than a microsecond to several milliseconds[116,117] which is also the range into which the laser, used here, falls. The novel shaped waveform does not have sharp edges near the absorption line center which is why it gives a better PA signal enhancement at large MI's than the QSW waveform.

5.2 EMFIT-based photoacoustic sensors

Three PA sensors based on the new type of EMFIT film microphone were developed in Publ. 2, 3, and 5 for the detection of gaseous NO_2. In the first of these three publications the EMFIT film microphone was introduced as a pressure transducer for the gas-phase PAS. The developed PA cell consisted of a cylindrical PA cell (see Fig. 5.5a). Half of the inner surface of the cylinder was coated with a 2-layer EMFIT film microphone, giving the same sensitivity as if the whole surface was laminated with a single EMFIT layer. Due to the flexibility and formability of the microphone film, a layered microphone with improved sensitivity is easy to construct simply by gluing the layers together and onto the surface of the PA cell. The benefit of using only the half of the surface was that both the radial and the azimuthal acoustic eigenmodes of the PA cell could be detected. The radial eigenmodes of the PA cell were excited using a pulsed tunable OPO laser system, pumped by a frequency-tripled Nd:YAG laser. Optimum excitation of the radial modes was achieved by tuning the laser wavelength to 436 nm where the NO_2 absorption cross-section is close to its maximum value (see Fig. 3.2), and where the laser pulse energy was 5.8 mJ. The best SNR was achieved by detecting the pulsed PA signal at the resonance frequency of the 6^{th} radial mode at 59.2 kHz. A limit of detection (LOD) of 27 ppb was achieved for NO_2 with a data acquisition time of 1 s. The LOD corresponds to a minimum detectable absorption coefficient of 5×10^{-7} cm^{-1}. The achieved LOD is low enough for example for monitoring NO_2 emissions from exhaust gases of gasoline engines where the relative mixing ratios can be in the ppm range[118]. Even though the demonstrated PA cell and the microphone

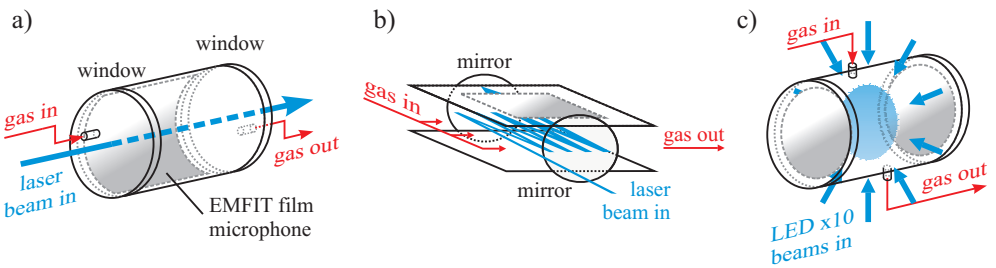

Figure 5.5 The three EMFIT-microphone-based PA sensors designed in Publ. 2, 3, and 5 are **(a)** the closed cylindrical PA cell with co-axial laser excitation of radial acoustic modes, **(b)** open rectangular multipass cell with transverse laser excitation of longitudinal modes, and **(c)** closed transparent cell with transverse excitation of longitudinal modes using an array of high-power LEDs, respectively.

are robust, the overall measurement setup hardly is field-deployable for NO_2 emission monitoring because of the bulkiness and high prices of the OPO laser system and data acquisition devices. Furthermore, the LOD of the PA setup should be somewhat lower for air quality monitoring of ambient urban air where the average concentrations of NO_2 are in the $5 - 30$ ppb range[5].

More sensitive PA detection of NO_2 is demonstrated in publications 3, and 5, using cheap and field-deployable technology. A 473 nm DPSS laser, operating in the CW mode and emitting an average of 10 mW of square-wave-modulated optical power, is utilized in Publ. 3. The PA cell was an open multipass cell which is shown in Fig. 5.5b. The DPSSL beam was bounced back and forth between the two high-reflectivity (99.8 %) mirrors, creating a plane of overlapping beams in between the two plates. A maximum of 70 laser beam passes was achieved, giving an effective optical excitation power of about 650 mW. The family of laser beams excited the 2^{nd} longitudinal acoustic eigenmode of the PA cell at 14.9 kHz. The pressure waves were detected with a 5-layer EMFIT film. Despite the low input power from the laser, the LOD of NO_2 was improved to 22 ppb due to multipass enhancement of the optical power and increased number of the layered EMFIT films. The sensitivity of the self-made 5-layer microphone was also characterized by comparing it with a calibrated, commercial condenser microphone and with a single microphone film layer. The acoustic responses are shown in Fig. 5.6 from which it can be seen that the layering of five films gives approximately five-fold sensitivity as compared to that of the single layer, and also the same sensitivity of the reference microphone which was in the mV/Pa range in the audible range. In addition, Fig. 5.6 illustrates the unique property of the EMFIT films which is their extremely broadband acoustic response. The measured electromechanical resonance of the single film layer was 280 kHz, and even as high as 45 kHz with the 5-layer microphone.

In Publ. 5 the NO_2 detection system was further improved. The schematic of the PA cell is shown in Fig. 5.5c. About seven times the optical power of Publ. 3 was realized using an array of ten high-power LEDs arranged onto the circumference of a transparent cylindrical PA cell, which was made of acrylic plastic. The LEDs illuminated the PA cell from the transverse or radial direction and excited the 2^{nd} longitudinal resonance at 3.9 kHz. Each of the LEDs emitted an average of 450 mW of modulated power. An additional improvement to the sensitivity of the device was made by adding another 5-layer microphone at the other end of the longitudinal resonator. Using low-

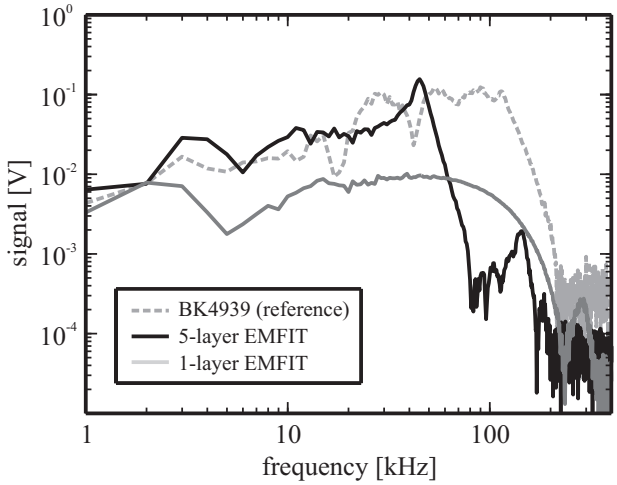

Figure 5.6 Measured acoustic responses of the EMFIT film microphones compared with a reference microphone, having a calibrated sensitivity of 4.14 mVPa at 250 Hz [Data from Publ. 3]. 5-layer EMFIT films were used in Publ. 3, and 5.

cost and field-deployable technology only, the LOD was more than halved to 10 ppb from the previous studies of this thesis. Furthermore, the LOD achieved here is more than six times better than the other more complicated LED-based photoacoustic NO_2 sensors, which have been introduced in different studies[86,87]. By comparing the total power of 4.5 W of the high-power LEDs with the 650 mW of the multipass PA system, the expected improvement on the LOD, due to the use of the LEDs, would have been by a factor of 1/7 instead of the 1/2. This is mainly attributed to the differences in the Q_n values of the LED and multipass PA cells. The Q_n values of the 2$^{\text{nd}}$ longitudinal

Table 5.1. Comparison of the key parameters of the EMFIT-film-based PA sensors developed in Publ. 2, 3, and 5 for the detection of NO_2.

Publ.	Fig. 5.5	Parameter						
		excitation	λ [nm]	Φ_{tot} [W]	f_n [kHz]	Q_n	LOD [ppb]	price* [€]
2	a	pulsed	436	1.1M†	59.8‡	1180	27	50,000
3	b	CW	473	0.65	14.9§	175	22	10,000
5	c	CW	453	4.50	3.9§	50	10	500

*Approximate component prices of the PA sensor, including the PA cell and the light source.
†Peak power of the pulsed laser.
$^{\ddagger}n = jmq = 600$ (6$^{\text{th}}$ radial resonance).
$^{\S}n = jmq = 002$ (2$^{\text{nd}}$ longitudinal).

resonances of the LED and multipass PA cells were 50 and 175, respectively. The key parameters of the three different PA sensors that were developed in this work, are summarized in Table 5.1.

5.3 Resonance tracking

A special emphasis was paid on the elimination of the background signals in Publ. 5, which actually enabled the afore-mentioned LOD of 10 ppb together with the use of high-power LEDs. The use of high-power light sources is beneficial in the PA method since the PA signal is directly proportional to the input power but, on the other hand, the PA signal from the background absorption can interfere with the detection of the targeted gas molecules – especially so with amplitude-modulated light sources. In the course of the study, it was found out that the high-power LEDs generated audible background PA signal at the measurement frequency. In addition, due to the high electric current (1 A) used to drive the LEDs, a large electric background was also observed. Large PA and electric background signals can limit the LOD of the PA detector if they are unstable in time. In order to avoid the interference caused by the electric background, two 5-layer EMFIT film microphones were used. The two microphones were constructed, and installed into the pressure field of the PA cell in such a way that they produced opposite-phase PA signals. With a differential measurement of the two PA signals the common-mode electric background was removed. Because the LEDs, which generated the audible noise, were placed outside the PA cell, the PA background experienced a phase lag with respect to the PA signal. Thus, due to the propagation delay between the acoustic waves, the interference caused by the LEDs was eliminated from the PA signal by using phase-sensitive detection.

Phase-sensitive detection was also used in Publ. 5 to demonstrate that the PA signal phase could be used to actively minimize the frequency difference between the modulation and the resonance frequency. As discussed in Sect. 4.4 and 2.1.3, the drift between the modulation and the resonance is a well-known problem in the resonant mode of operation of a PA cell. In Fig. 5.7a two long-term measurement sequences are shown where the PA signal from 3 ppm NO_2 sample was measured for two hours during which the PA cell's temperature rose by about 15°C due to the heating, caused by the high-power LEDs. The dotted curves are the actual measured imaginary parts of

the PA signals as a function of time. With the use of the resonance tracking algorithm the modulation frequency followed the drifting acoustic resonance according to the staircase-type frequency plot of Fig. 5.7b. The 1.9 Hz steps in Fig. 5.7b correspond to the resolution of the FFT spectrum, which was defined by the 1 MHz sampling rate and 2^{19} number of data points. The modulation frequencies were tuned in discrete steps so that the critical sampling of the PA signal was maintained at all frequencies. The linear trend in the raw PA signal is related to a temperature-dependent microphone sensitivity, which is removed from the solid curves in Fig. 5.7a. The baseline correction was made to show the expected PA signal level that would be measured if the self-made EMFIT microphones were calibrated. In addition, by eliminating this systematic error the PA signal stability can be analyzed.

The Allan variance or the two-sample variance[119] can be used to analyze the PA signal stability. It is defined as[120]

$$\sigma_y{}^2(\tau) = \left\langle (\bar{y}_{n+1} - \bar{y}_n)^2 \right\rangle \tag{5.1}$$

where τ is the data acquisition or integration time, $\bar{y}_n$ is the average signal of n samples within the observation interval τ. Correspondingly, $\bar{y}_{n+1}$ is the average of $\bar{y}_n$ and the

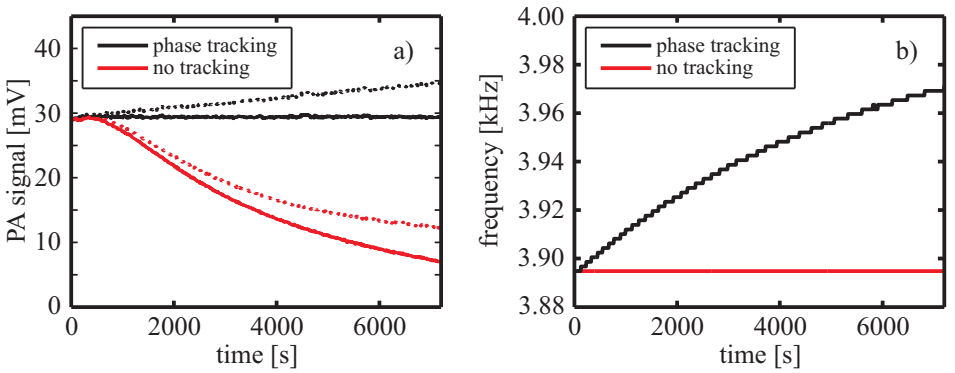

Figure 5.7 Long-term PA measurement of constant 3 ppm of NO_2 using phase-sensitive detection and the resonance tracking method presented in Chap. 4.4. **(a)** The PA signals as a function of measurement time, and **(b)** the corresponding modulation frequencies of the LEDs. The linear trend in the dotted line in (a) is related to the changing sensitivity of the microphone which was removed from the solid curves to represent the expected constant PA signal level. (Data partly from Publ. 5).

next $(n+1)^{\text{th}}$ data point. In other words, the Allan variance describes how the average signal level evolves as the integration time τ increases. The assumption in Eq. 5.1 is that there is no dead time between the samples. In practice, data is usually sampled for a finite time, and there is a dead time before the next sample is acquired. In Publ. 5 the difference PA signal was acquired for 2.1 s, which was followed by about 5 s of data processing time or dead time. In order to be able to apply Eq. 5.1 to such data, the dead times have to be removed. The Allan deviation, i.e. the square root of Eq. 5.1, is presented in Fig. 5.8 for the two solid curves of Fig. 5.7a with the dead time removed. It can be seen from Fig. 5.8 that the resonance tracking algorithm enables long-term measurement of the NO_2 concentration, and the deviation reduces linearly on the logarithmic scale with a slope of -0.9. This is useful for example if longer integration times are required for the sake of improving the measurement accuracy. If the resonance tracking is not used and the modulation frequency of the LEDs is left passively to the initial value while the resonance drifts, it is evident that the optimum averaging time is limited to about 2 min which corresponds, in these measurements, to the time taken for the peak of the PA cell's resonance to drift away from the starting frequency.

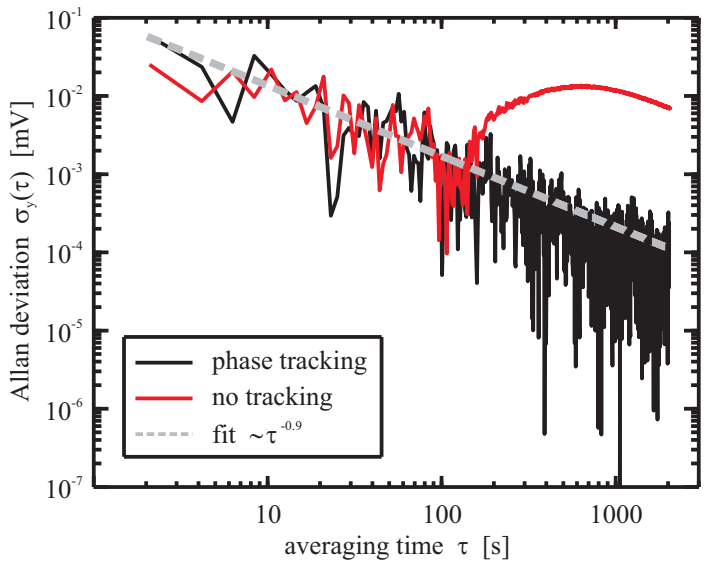

Figure 5.8 Allan deviation of a long-term, phase-sensitive PA measurement of 3 ppm of NO_2 with (—) and without (—) the resonance tracking. The resonance tracking allows for long integration times, improving the measurement accuracy.

5.4 Pulsed photoacoustic detection of propofol

A resonantly excited PA cell was developed in Publ. 4 for the detection of gas-phase propofol. This is the first study in the field of optical spectroscopy where the feasibility of the detection of the anesthetic agent propofol was demonstrated in the gas phase. The PA cell is presented in Fig. 5.9a. It consists of a hollow cylinder as the acoustic resonator in the central part of the cell, windows, and acoustic bafflers in between them. The PA signal is picked up by a calibrated condenser microphone whose membrane was aligned to the level of the inner surface of the resonator. The radius of the resonator was 12 mm giving the resonance frequency of about 17.8 kHz for the first radial mode in nitrogen atmosphere. The first radial mode was excited using the same wavelength-tunable OPO laser, which was also used in Publ. 2, in the wavelength range of $210 - 310$ nm. The PA signals from the microphone were electronically band-pass-filtered to $12 - 23$ kHz so that only the first radial mode at 17.8 kHz was observed and recorded with an oscilloscope. According to Eq. 2.4 and the values given in Table 2.1, the two closest higher radial modes are located at 32.8 kHz and 47.5 kHz.

The PA spectrum shown in Fig. 5.9b was measured by stepping the emission wavelength of the OPO laser in 2 nm intervals. The PA signal is presented here as the initial amplitude of the pressure wave normalized with the average pulse energy of the OPO laser. As opposed to the previous studies, here the absolute pressure amplitude in pascals was calculated from the measured PA signals because of the availability of the calibration data of the microphone. In addition, the PA signals were normalized with the laser pulse energies due to changes in the energies between different laser wavelengths. At each wavelength a thousand PA signal pulses were averaged, giving

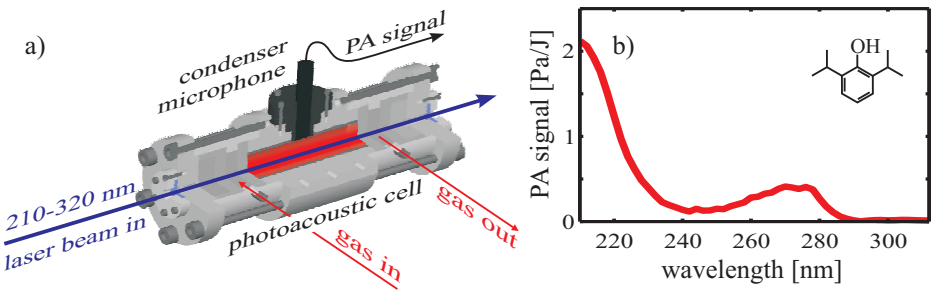

Figure 5.9 PA detection of gas-phase propofol. **(a)** The cylindrical PA cell with the detection of the first radial acoustic mode. **(b)** The PA spectrum of propofol (Data from Publ. 4).

a total integration time of 20 s per data point. The highest PA signal was observed at 270 nm where the SNR was 420 yielding a LOD of 0.12 ppb. This is a promising result and sufficient for the detection of the anesthetic agent propofol whose concentrations in the exhaled breath fall into the range of tens of ppb. However, the UV spectral range is known as a problematic region for molecule specific detection since many molecules have overlapping absorption spectra. In the exhaled breath acetone may be the major compound causing interference to the PA detection of propofol, as discussed in detail in Publ. 4. On the other hand, these two compounds have absorption maxima at different wavelengths so that the identification should be possible using multi-wavelength PA detection. In addition, the phase-sensitive PA detection offers another possible solution for the molecular discrimination due to the fact that different molecules have different thermal relaxation times. This can be exploited especially in the PAS at high frequencies and at low gas pressures, in which case the phase shifts between the PA signals of the different gas components may become significant [11]. Further research on the selectivity of the PA detection of propofol in exhaled air would be needed.

Chapter 6

Summary

PHOTOACOUSTIC spectroscopy (PAS) of gases was studied in this Thesis. The photoacoustic (PA) method is based on the absorption of modulated light by the sample molecules, which results into a temporally varying pressure wave inside the sample volume that is measured with a microphone. In trace gas detection the sensitivity of the PA sensor is a crucial parameter, which affects the reliability of the measurement. In addition to the design of a photoacoustic sensor, the sensitivity is also dependent on the modulation waveform that is used to generate the pressure wave. In general, the excitation of the pressure wave can be accomplished either by wavelength or amplitude modulation of the light source.

The first of the five publications, included into this Thesis, focussed on the use of different wavelength modulation waveforms in laser photoacoustic spectroscopy. In the experiments CO_2 was used as the target molecule whose rotational line in the near infrared spectrum was probed with a telecom DFB diode laser, and the photoacoustically excited pressure variations were detected with a non-resonant PA detector. It was shown that a quasi-square modulation waveform is the ideal choice, and it gives the best sensitivity for the PA detection but in practice the sensitivity can be limited due to a possible delayed wavelength tuning of the laser. In the study, a novel shaped waveform was introduced which mimics the absorption line profile, across which the laser wavelength is scanned, and produces a purely sinusoidal PA signal. The shaped

waveform was less prone to the delayed wavelength tuning of the laser and gave better results than the other modulation waveforms at large wavelength modulation amplitudes. The results of the publication give insight for the optimization of the wavelength modulation in laser photoacoustic spectroscopy.

In the second study a new type of acoustic transducer was introduced for PAS. The transducer is a recently developed electromechanical film microphone (EMFIT). It has unique properties as compared to other microphones that have been used in PAS earlier. The sensitivity of the EMFIT film microphone is comparable to those of the best condenser microphones albeit the fact that its acoustic response is extremely broadband, which is especially useful in PAS at high signal frequencies. Furthermore, the films can be layered and formed to different shapes which enable easy integration of the films into all kinds of PA sensor designs. The EMFIT films are also cheap so that low-cost but sensitive PA sensors can be realized. Indeed in publications 3 and 5 it was shown that EMFIT films can be used for NO_2 detection in simple and cost-effective PA sensors which nevertheless are highly sensitive. The best NO_2 detection limit using LEDs as light sources is 10 ppb, and it was demonstrated in publication 5 by using a resonant PA cell, operating at 3.9 kHz, and phase-sensitive detection of the PA signals. The phase-sensitive detection method, developed in this work, was accomplished using fast-Fourier transform algorithms for data processing as an alternative to the commonly used lock-in amplifier devices. It was also shown that the PA signal phase can be used as a feedback for the modulation frequency of the light source in order to stabilize the PA measurement. This is especially important in automated long-term measurements when resonant PA sensors whose resonance frequency may drift due to changes in the speed of sound, are used.

In publication 4 it was shown that pulsed resonant PA detection in the UV spectral region of light is a feasible method for the detection of gas-phase propofol. Propofol is an intravenous agent that is use in surgical operation to sedate a patient. The concentration of the exhaled propofol gives information about the metabolized levels of propofol and also the depth of the anesthesia. The limit of detection achieved by the PA method was 0.12 ppb which is well below typical propofol concentrations in a patient's breath during the operation.

References

[1] J. M. Langridge, T. Laurila, R. S. Watt, R. L. Jones, C. F. Kaminski, and J. Hult, "Cavity enhanced absorption spectroscopy of multiple trace gas species using a supercontinuum radiation source," Opt. Express **16**, 10178–10188 (2008).

[2] A. G. Bell, "On the production and reproduction of sound by light," Am. J. Sci. **20**, 305–324 (1880).

[3] A. Rosencwaig, *Photoacoustics and Photoacoustic spectroscopy* (Robert E. Krieger Publishing Company, 1980).

[4] "Inventory of U.S. greenhouse gas emissions and sinks: 1990–2009," Tech. rep., U.S. Environmental Protection Agency (2011).

[5] "Our nations air - status and trends through 2008," Tech. rep., U.S. Environmental Protection Agency (2010).

[6] T. Perl, E. Carstens, A. Hirn, M. Quintel, W. Vautz, J. Nolte, and M. Jnger, "Determination of serum propofol concentrations by breath analysis using ion mobility spectrometry," British Journal of Anaesthesia **103**, 822–827 (2009).

[7] A. Manninen, "Pulsed laser spectroscopy: Bioaerosol fluorescence and gas-phase photoacoustics," Ph.D. thesis, Tampere University of Technology (2009).

[8] T. Sorvajärvi, A. Manninen, J. Toivonen, J. Saarela, and R. Hernberg, "Photoacoustic resonance cell for pulsed laser analysis of gases in high-temperature," Rev. Sci. Instrum. (2009).

[9] G. Calasso, "Photoacoustic and photothermal laser spectroscopy applied to trace gas detection and molecular dynamics," Ph.D. thesis, Swiss Federal Institute of Technology (1998).

[10] V. P. Zharov and V. S. Letokhov, *Laser Optoacoustic Spectroscopy* (Springer-Verlag, Berlin, 1986).

[11] A. Kosterev, Y. Bakhirkin, F. Tittel, S. Blaser, Y. Bonetti, and L. Hvozdara, "Photoacoustic phase shift as a chemically selective spectroscopic parameter," Applied Physics

B: Lasers and Optics **78**, 673–676 (2004).

[12] P. M. Morse, *Vibration and Sound* (McGraw-Hill Book Company, Inc., 1948).

[13] A. Miklós, P. Hess, and Z. Bozóki, "Application of acoustic resonators in photoacoustic trace gas analysis and metrology," Rev. Sci. Instrum. **72**, 1937–1955 (2001).

[14] D. A. Bohn, "Environmental effects on the speed of sound," J. Audio Eng. Soc **36**, 223–231 (1988).

[15] M. F. C. Gomes and J. P. M. Trusler, "The speed of sound in nitrogen at temperatures between T = 250 K and T = 350 K and at pressures up to 30 MPa," The Journal of Chemical Thermodynamics **30**, 527 – 534 (1998).

[16] S. Schäfer, A. Miklós, and P. Hess, "Quantitative signal analysis in pulsed resonant photoacoustics," Appl. Opt. **36**, 3202–3211 (1997).

[17] S. L. Firebaugh, K. F. Jensen, and M. A. Schmidt, "Miniaturization and integration of photoacoustic detection," Journal of Applied Physics **92**, 1555–1563 (2002).

[18] S. Schäfer, A. Miklos, A. Pusel, and P. Hess, "Absolute measurement of gas concentrations and saturation behavior in pulsed photoacoustics," Chemical Physics Letters **285**, 235–239 (1998).

[19] V. Zeninari, V. A. Kapitanov, D. Courtois, and Y. N. Ponomarev, "Design and characteristics of a differential helmholtz resonant photoacoustic cell for infrared gas detection," Infrared Physics and Technology **40**, 1–23 (1999).

[20] V. Zeninari, B. Parvitte, D. Courtois, V. A. Kapitanov, and Y. N. Ponomarev, "Methane detection on the sub-ppm level with a near-infrared diode laser photoacoustic sensor," Infrared Physics & Technology **44**, 253–261 (2003).

[21] Y. N. Ponomarev, "Photo-acoustic measurements of gas and aerosol absorption with diode lasers," Spectrochimica Acta Part A: Molecular and Biomolecular Spectroscopy **60**, 3469 – 3476 (2004).

[22] M. Mattiello, M. Niklès, S. Schilt, L. Thévenaz, A. Salhi, D. Barat, A. Vicet, Y. Rouillard, R. Werner, and J. Koeth, "Novel helmholtz-based photoacoustic sensor for trace gas detection at ppm level using GaInAsSb/GaAlAsSb DFB lasers," Spectrochimica Acta Part A: Molecular and Biomolecular Spectroscopy **63**, 952 – 958 (2006). 5th International Conference on Tunable Diode Laser Spectroscopy, 2005.

[23] M. Mattiello, "Gas traces measurement by photoacoustic spectroscopy using helmholtz resonator-based sensors," Ph.D. thesis, École Polytechnique Fédérale de Lausanne (2008).

[24] A. Karbach, J. Roper, and P. Hess, "Computer-controlled performance of photoacoustic resonance experiments," Review of Scientific Instruments **55**, 892–895 (1984).

[25] A. Karbach and P. Hess, "Laser excitation of acoustic resonances in a spherical resonator," Journal of Applied Physics **58**, 3851–3855 (1985).

[26] L.-Y. Hao, S. Qiang, G.-R. Wu, L. Qi, D. Feng, Q.-S. Zhu, and Z. Hong, "Cylindrical mirror multipass lissajous system for laser photoacoustic spectroscopy," Review of

Scientific Instruments **73**, 2079–2085 (2002).

[27] P. M. Morse and K. U. Ingard, *Theoretical Acoustics* (McGraw-Hill Book Company, Inc., 1968).

[28] R. Gerlach and N. Amer, "Brewster window and windowless resonant spectrophones for intracavity operation," Applied Physics A: Materials Science & Processing **23**, 319–326 (1980).

[29] F. J. M. Harren, F. G. C. Bijnen, J. Reuss, L. A. C. J. Voesenek, and C. W. P. M. Blom, "Sensitive intracavity photoacoustic measurements with a CO_2 waveguide laser," Applied Physics B Photophysics Laser Chemistry **50**, 137–144 (1990).

[30] F. G. C. Bijnen, F. J. M. Harren, J. H. P. Hackstein, and J. Reuss, "Intracavity co laser photoacoustic trace gas detection: cyclic ch_4, h_2o and co_2 emission by cockroaches and scarab beetles," Appl. Opt. **35**, 5357–5368 (1996).

[31] C. Hornberger, M. König, S. B. Rai, and W. Demtröder, "Sensitive photoacoustic overtone spectroscopy of acetylene with a multipass photoacoustic cell and a colour centre laser at 1.5 μm," Chemical Physics **190**, 171 – 177 (1995).

[32] M. Nägele and M. Sigrist, "Mobile laser spectrometer with novel resonant multipass photoacoustic cell for trace-gas sensing," Applied Physics B: Lasers and Optics **70**, 895–901 (2000).

[33] J. Rey, D. Marinov, D. Vogler, and M. Sigrist, "Investigation and optimisation of a multipass resonant photoacoustic cell at high absorption levels," Appl. Phys. B **80**, 261–266 (2005).

[34] N. Ioli, P. Violino, and M. Meucci, "A simple transversely excited spectrophone," Journal of Physics E: Scientific Instruments **12**, 168–170 (1979).

[35] K. Veeken, N. Dam, and J. Reuss, "A multipass transverse photoacoustic cell," Infrared Physics **25**, 683–696 (1985).

[36] D. Herriott, H. Kogelnik, and R. Kompfner, "Off-axis paths in spherical mirror interferometers," Appl. Opt. **3**, 523–526 (1964).

[37] G. S. Engel and E. J. Moyer, "Precise multipass herriott cell design: Derivation of controlling design equations," Opt. Lett. **32**, 704–706 (2007).

[38] A. Miklós, S.-C. Pei, and A. H. Kung, "Multipass acoustically open photoacoustic detector for trace gas measurements," Appl. Opt. **45**, 2529–2534 (2006).

[39] V. A. Kapitanov, V. Zeninari, B. Parvitte, D. Courtois, and Y. N. Ponomarev, "Optimisation of photoacoustic resonant cells with commercial microphones for diode laser gas detection," Spectrochim Acta A Mol Biomol Spectrosc **58**, 2397–2404 (2002).

[40] J. M. Rey and M. W. Sigrist, "Differential mode excitation photoacoustic spectroscopy: A new photoacoustic detection scheme," Rev. Sci. Instrum. **78**, 063104–1–063104–5 (2007).

[41] J. Uotila, V. Koskinen, and J. Kauppinen, "Selective differential photoacoustic method for trace gas analysis," Vibrational Spectroscopy **38**, 3–9 (2005).

[42] Brüel&Kjær, *Microphone Handbook – Vol. 1: Theory*, Nærum, Denmark (1996).

[43] J. Kauppinen, K. Wilcken, I. Kauppinen, and V. Koskinen, "High sensitivity in gas analysis with photoacoustic detection," Microchemical Journal **76**, 151–159 (2004).

[44] I. G. Calasso and M. W. Sigrist, "Selection criteria for microphones used in pulsed nonresonant gas-phase photoacoustics," Rev. Sci. Instrum. **70**, 4569–4578 (1999).

[45] J.-M. Heritier, J. E. Fouquet, and A. E. Siegman, "Photoacoustic cell using elliptical acoustic focusing," Appl. Opt. **21**, 90–93 (1982).

[46] K. Kirjavainen, "Electromechanical film and procedure for manufacturing same," U.S. Patent No. 4 654 546 (1987).

[47] A. Savolainen and K. Kirjavainen, "Electrothermomechanical film. part i. design and characteristics," Journal of Macromolecular Science: Part A - Chemistry **26**, 583–591 (1989).

[48] M. Paajanen, J. Lekkala, and K. Kirjavainen, "Electromechanical film (EMFi) - a new multipurpose electret material," Sens. Actuators, A **84**, 95–102 (2000).

[49] J. Hillenbrand and G. M. Sessler, "High-sensitivity piezoelectric microphones based on stacked cellular polymer films (l)," Acoustical Society of America Journal **116**, 3267–3270 (2004).

[50] V. Bovtun, J. Döring, J. Bartusch, U. Beck, A. Erhard, and Y. Yakymenko, "Ferroelectret non-contact ultrasonic transducers," Appl. Phys. A **88**, 737–743 (2007).

[51] J. Döring, V. Bovtun, J. Bartusch, U. Beck, and M. Kreutzbruck, "Cellular polypropylene ferroelectret film piezoelectric material for non-contact ultrasonic transducers," 17th World Conference on Nondestructive Testing, Shanghai, China (2008).

[52] P. C. Claspy, C. Ha, and Y.-H. Pao, "Optoacoustic detection of no_2 using a pulsed dye laser," Appl. Opt. **16**, 2972–2973 (1977).

[53] M. M. Farrow, R. K. Burnham, M. Auzanneau, S. L. Olsen, N. Purdie, and E. M. Eyring, "Piezoelectric detection of photoacoustic signals," Appl. Opt. **17**, 1093–1098 (1978).

[54] Y. Nosaka and E. Tokunaga, "Development of photoacoustic spectroscopy with a piezofilm," Appl. Opt. **46**, 4289–4293 (2007).

[55] K. Wilcken and J. Kauppinen, "Optimization of a microphone for photoacoustic spectroscopy," Appl. Spectrosc. **57**, 1087–1092 (2003).

[56] T. Laurila, H. Cattaneo, V. Koskinen, J. Kauppinen, and R. Hernberg, "Diode laser-based photoacoustic spectroscopy with interferometrically-enhanced cantilever detection," Opt. Express **13**, 2453–2458 (2005).

[57] T. Laurila, H. Cattaneo, T. Pyhnen, V. Koskinen, J. Kauppinen, and R. Hernberg, "Cantilever-based photoacoustic detection of carbon dioxide using a fiber-amplified diode laser," Applied Physics B: Lasers and Optics **83**, 285–288 (2006). 10.1007/s00340-005-2106-9.

[58] H. Cattaneo, T. Laurila, and R. Hernberg, "Photoacoustic detection of oxygen using cantilever enhanced technique," Appl. Phys. B **85**, 337–341 (2006).

[59] V. Koskinen, J. Fonsen, K. Roth, and J. Kauppinen, "Cantilever enhanced photoacoustic detection of carbon dioxide using a tunable diode laser source," Appl. Phys. B **86**, 451–454 (2007).

[60] V. Koskinen, J. Fonsen, K. Roth, and J. Kauppinen, "Progress in cantilever enhanced photoacoustic spectroscopy," Vibrational Spectroscopy **48**, 16 – 21 (2008).

[61] T. Kuusela, J. Peura, B. Matveev, M. Remennyy, and N. Stus', "Photoacoustic gas detection using a cantilever microphone and III-V mid-IR LEDs," Vibrational Spectroscopy **51**, 289 – 293 (2009).

[62] J. Uotila, "Use of the optical cantilever microphone in photoacoustic spectroscopy," Ph.D. thesis, University of Turku (2009).

[63] C. B. Hirschmann, J. Uotila, S. Ojala, J. Tenhunen, and R. L. Keiski, "Fourier transform infrared photoacoustic multicomponent gas spectroscopy with optical cantilever detection," Appl. Spectrosc. **64**, 293–297 (2010).

[64] C. B. Hirschmann, N. S. Koivikko, J. Raittila, J. Tenhunen, S. Ojala, K. Rahkamaa-Tolonen, R. Marbach, S. Hirschmann, and R. L. Keiski, "FT-IR-cPAS – new photoacoustic measurement technique for analysis of hot gases: A case study on VOCs," Sensors **11**, 5270–5289 (2011).

[65] A. A. Kosterev, Y. Bakhirkin, R. F. Curl, and F. K. Tittel, "Quartz-enhanced photoacoustic spectroscopy," Opt. Lett. **27**, 1902–1904 (2002).

[66] R. D. Grober, J. Acimovic, J. Schuck, D. Hessman, P. J. Kindlemann, J. Hespanha, A. S. Morse, K. Karrai, I. Tiemann, and S. Manus, "Fundamental limits to force detection using quartz tuning forks," Review of Scientific Instruments **71**, 2776–2780 (2000).

[67] A. A. Kosterev, F. K. Tittel, D. V. Serebryakov, A. L. Malinovsky, and I. V. Morozov, "Applications of quartz tuning forks in spectroscopic gas sensing," Review of Scientific Instruments **76**, 043105 (2005).

[68] A. Kosterev, G.Wysocki, Y. Bakhirkin, S. So, R. Lewicki, M. Fraser, F. Tittel, and R. Curl, "Application of quantum cascade lasers to trace gas analysis," Appl. Phys. B **90**, 165–176 (2008).

[69] R. Lewicki, G. Wysocki, A. A. Kosterev, and F. K. Tittel, "QEPAS based detection of broadband absorbing molecules using a widely tunable, cw quantum cascade laser at 8.4 μm," Opt. Express **15**, 7357–7366 (2007).

[70] K. Liu, J. Li, L. Wang, T. Tan, W. Zhang, X. Gao, W. Chen, and F. K. Tittel, "Trace gas sensor based on quartz tuning fork enhanced laser photoacoustic spectroscopy," Appl. Phys. B **94**, 527–533 (2009).

[71] K. Liu, X. Guo, H. Yi, W. Chen, W. Zhang, and X. Gao, "Off-beam quartz-enhanced photoacoustic spectroscopy," Opt. Lett. **34**, 1594–1596 (2009).

[72] J. M. Hollas, *Modern Spectroscopy* (Wiley, 2004), 4th ed.

[73] Y. Itikawa, "Cross sections for electron collisions with carbon dioxide," J. Phys. Chem. **31**, 749 –767 (2002).

[74] J. Henningsen and H. Simonsen, "The $(22^01 - 00^00)$ band of co_2 at 6348 cm^{-1}: Linestrengths, broadening parameters, and pressure shifts," Journal of Molecular Spectroscopy **203**, 16 – 27 (2000).

[75] L. Rothman, D. Jacquemart, A. Barbe, D. C. Benner, M. Birk, L. Brown, M. Carleer, C. Chackerian, Jr., K. Chance, L. Coudert, V. Dana, V. Devi, J.-M. Flaud, R. Gamache, A. Goldman, J.-M. Hartmann, K. Jucks, A. Maki, J.-Y. Mandin, S. Massie, J. Orphal, A. Perrin, C. Rinsland, M. Smith, J. Tennyson, R. Tolchenov, R. Toth, J. V. Auwera, P. Varanasi, and G. Wagner, "The HITRAN 2004 molecular spectroscopic database," Journal of Quantitative Spectroscopy and Radiative Transfer **96**, 139 – 204 (2005).

[76] L. Rothman, I. Gordon, A. Barbe, D. Benner, P. Bernath, M. Birk, V. Boudon, L. Brown, A. Campargue, J.-P. Champion, K. Chance, L. Coudert, V. Dana, V. Devi, S. Fally, J.-M. Flaud, R. Gamache, A. Goldman, D. Jacquemart, I. Kleiner, N. Lacome, W. Lafferty, J.-Y. Mandin, S. Massie, S. Mikhailenko, C. Miller, N. Moazzen-Ahmadi, O. Naumenko, A. Nikitin, J. Orphal, V. Perevalov, A. Perrin, A. Predoi-Cross, C. Rinsland, M. Rotger, M. Simeckov, M. Smith, K. Sung, S. Tashkun, J. Tennyson, R. Toth, A. Vandaele, and J. V. Auwera, "The HITRAN 2008 molecular spectroscopic database," Journal of Quantitative Spectroscopy and Radiative Transfer **110**, 533 – 572 (2009).

[77] M. Pushkarsky, A. Tsekoun, I. G. Dunayevskiy, R. Go, and C. K. N. Patel, "Sub-parts-per-billion level detection of NO_2 using room-temperature quantum cascade lasers," Proceedings of the National Academy of Sciences **103**, 10846–10849 (2006).

[78] J. Lima, H. Vargas, A. Mikls, M. Angelmahr, and P. Hess, "Photoacoustic detection of NO_2 and N_2O using quantum cascade lasers," Applied Physics B: Lasers and Optics **85**, 279–284 (2006).

[79] R. A. Gangi and L. Burnelle, "Electronic structure and electronic spectrum of nitrogen dioxide. iii spectral interpretation," The Journal of Chemical Physics **55**, 851–856 (1971).

[80] N. Barreiro, A. Vallespi, A. Peuriot, V. Slezak, and G. Santiago, "Quenching effects on pulsed photoacoustic signals in NO_2-air samples," Applied Physics B: Lasers and Optics **99**, 591–597 (2010).

[81] R. Bartlome, M. Kaučikas, and M. W. Sigrist, "Modulated resonant versus pulsed resonant photoacoustics in trace gas detection," Appl. Phys. B **96**, 56–1–566 (2009).

[82] V. Slezak, "High-precision pulsed photoacoustic spectroscopy in NO_2-N_2," Applied Physics B: Lasers and Optics **73**, 751–755 (2001).

[83] V. Slezak, G. Santiago, and A. L. Peuriot, "Photoacoustic detection of NO_2 traces with CW and pulsed green lasers," Optics and Lasers in Engineering **40**, 33 – 41 (2003).

[84] H. Yi, K. Liu, W. Chen, T. Tan, L. Wang, and X. Gao, "Application of a broadband blue laser diode to trace NO_2 detection using off-beam quartz-enhanced photoacoustic spectroscopy," Opt. Lett. **36**, 481–483 (2011).

[85] J. Kalkman and H. van Kesteren, "Relaxation effects and high sensitivity photoacoustic detection of NO_2 with a blue laser diode," Applied Physics B: Lasers and Optics **90**, 197–200 (2008).

[86] R. Bernhardt, G. D. Santiago, V. B. Slezak, A. Peuriot, and M. G. Gonzlez, "Differential, LED-excited, resonant NO_2 photoacoustic system," Sensors and Actuators B: Chemical **150**, 513 – 516 (2010).

[87] G. D. Santiago, M. G. Gonzalez, A. L. Peuriot, F. Gonzalez, and V. B. Slezak, "Blue light-emitting diode-based, enhanced resonant excitation of longitudinal acoustic modes in a closed pipe with application to NO_2," Review of Scientific Instruments **77**, 023108 –023108–3 (2006).

[88] K. Bogumil, J. Orphal, T. Homann, S. Voigt, P. Spietz, O. C. Fleischmann, A. Vogel, M. Hartmann, H. Kromminga, H. Bovensmann, J. Frerick, and J. P. Burrows, "Measurements of molecular absorption spectra with the SCIAMACHY pre-flight model: instrument characterization and reference data for atmospheric remote-sensing in the 230 − 2380 nm region," Journal of Photochemistry and Photobiology A: Chemistry **157**, 167 – 184 (2003). Atmospheric Photochemistry.

[89] J. N. Seinfeld and S. N. Pandis, *Atmospheric chemistry and physics: from air pollution to climate change* (John Wiley & Sons, Inc., 2006), 2nd ed.

[90] C. M. Roehl, J. J. Orlando, G. S. Tyndall, R. E. Shetter, G. J. Vazquez, C. A. Cantrell, and J. G. Calvert, "Temperature dependence of the quantum yields for the photolysis of NO_2 near the dissociation limit," The Journal of Physical Chemistry **98**, 7837–7843 (1994).

[91] B. Heyne, F. Tfibel, M. Hoebeke, P. Hans, V. Maurel, and M.-P. Fontaine-Aupart, "Photochemistry of 2,6-diisopropylphenol (propofol)," Photochem. Photobiol. Sci. **5**, 1059–1067 (2006).

[92] O. Friaa, V. Chaleix, M. Lecouvey, and D. Brault, "Reaction between the anesthetic agent propofol and the free radical DPPH in semiaqueous media: Kinetics and characterization of the products," Free Radical Biology and Medicine **45**, 1011 – 1018 (2008).

[93] G. James, D. Burley, P. Dyke, J. Searl, N. Steele, and J. Wright, *Advanced Modern Engineering Mathematics* (Pearson Education Limited, 1999), 2nd ed.

[94] J. Kauppinen and J. Partanen, *Fourier transforms in spectroscopy* (WILEY-VCH Verlag Berlin GmbH, 2001).

[95] J. W. Cooley and J. W. Tukey, "An algorithm for the machine calculation of complex fourier series," Mathematics of Computation **19**, 297–301 (1965).

[96] G. D. Bergland, "A guided tour of the fast fourier transform," Spectrum, IEEE **6**, 41–52 (1969).

[97] R. Chang and R. Gibby, "A theoretical study of performance of an orthogonal multiplexing data transmission scheme," Communication Technology, IEEE Transactions on **16**, 529 –540 (1968).

[98] S. Weinstein and P. Ebert, "Data transmission by frequency-division multiplexing using

the discrete fourier transform," Communication Technology, IEEE Transactions on **19**, 628 –634 (1971).

[99] J. Heiskala and J. Terry, Ph.D., *OFDM Wireless LANs: A Theoretical and Practical Guide* (Sams, Indianapolis, IN, USA, 2001).

[100] T. Ajtai, gnes Filep, M. Schnaiter, C. Linke, M. Vragel, Z. Bozki, G. Szab, and T. Leisner, "A novel multi-wavelength photoacoustic spectrometer for the measurement of the UV-vis-NIR spectral absorption coefficient of atmospheric aerosols," Journal of Aerosol Science **41**, 1020 – 1029 (2010).

[101] J. Reid and D. Labrie, "Second-harmonic detection with tunable diode lasers – comparison of experiment and theory," Applied Physics B: Lasers and Optics **26**, 203–210 (1981).

[102] S. L. Castleden, G. F. Kirkbright, and D. E. M. Spillane, "Wavelength modulation in photoacoustic spectroscopy," Analytical Chemistry **53**, 2228–2231 (1981).

[103] M. Angelmahr, A. Mikls, and P. Hess, "Wavelength- and amplitude-modulated photoacoustics: comparison of simulated and measured spectra of higher harmonics," Appl Opt **47**, 2806–2812 (2008).

[104] L. Goldberg, H. Taylor, and J. Weller, "Time-dependent thermal effects in current-modulated semiconductor lasers," Electronics Letters **17**, 497 –499 (1981).

[105] Y. Wang, H. Cai, J. Geng, and Z. Fang, "Logarithmic conversion of absorption detection in wavelength modulation spectroscopy with a current-modulated diode laser," Appl. Opt. **48**, 4068–4076 (2009).

[106] W. Demtröder, *Laser Spectroscopy: Basic Concepts and Instrumentation* (Springer, 1996), 2nd ed.

[107] T. Iguchi, "Modulation waveforms for second-harmonic detection with tunable diode lasers," J. Opt. Soc. Am. B **3**, 419–423 (1986).

[108] A. Fried, J. Drummond, B. Henry, and J. Fox, "Versatile integrated tunable diode laser system for high precision: application for ambient measurements of OCS," Appl Opt **30**, 1916–1932 (1991).

[109] J. Pilgrim and D. Bomse, "Wavelength modulated photoacoustic spectrometer," U.S. Patent No. 6 552 792 (2000).

[110] P.-A. Probst and A. Jaquier, "Multiple-channel digital lock-in amplifier with PPM resolution," Review of Scientific Instruments **65**, 747–750 (1994).

[111] X. Wang, "Sensitive digital lock-in amplifier using a personal computer," Review of Scientific Instruments **61**, 1999–2001 (1990).

[112] J. H. Scofield, "Frequency-domain description of a lock-in amplifier," American Journal of Physics **62**, 129–133 (1994).

[113] P. K. Dixon and L. Wu, "Broadband digital lock-in amplifier techniques," Review of Scientific Instruments **60**, 3329–3336 (1989).

[114] F. T. G. Wysocki, A.A. Kosterev, "Influence of molecular relaxation dynamics on quartz-enhanced photoacoustic detection of co2 at ? = 2 ?m," Appl. Phys. B **85**, 301–306 (2006).

[115] R. E. T. L. Besson J.-P., Schilt S., "Ammonia trace measurements at ppb level based on near-ir photoacoustic spectroscopy," Appl. Phys. B **85**, 323–328 (2006).

[116] M. Ito and T. Kimura, "Stationary and transient thermal properties of semiconductor laser diodes," **17**, 787–795 (1981).

[117] W. Li, X. Li, and W.-P. Huang, "A traveling-wave model of laser diodes with consideration for thermal effects," Optical and Quantum Electronics **36**, 709?724 (2004).

[118] J. H. Shorter, S. Herndon, M. S. Zahniser, D. D. Nelson, J. Wormhoudt, K. L. Demerjian, and C. E. Kolb, "Real-time measurements of nitrogen oxide emissions from in-use new york city transit buses using a chase vehicle," Environmental Science & Technology **39**, 7991–8000 (2005).

[119] D. Allan, "Statistics of atomic frequency standards," Proceedings of the IEEE **54**, 221–230 (1966).

[120] A. Barnes and D. Allan, "Variances based on data with dead time between the measurements," NIST Technical Note 1318 pp. 296–335 (1990).

Appendices

Publication 1

Jaakko Saarela, Juha Toivonen, Albert Manninen, Tapio Sorvajärvi, and Rolf Hernberg.

Wavelength modulation waveforms in laser photoacoustic spectroscopy.

Applied Optics **48**, 743–747 (2009)

Wavelength modulation waveforms in laser photoacoustic spectroscopy

Jaakko Saarela,* Juha Toivonen, Albert Manninen, Tapio Sorvajärvi, and Rolf Hernberg

Optics Laboratory, Department of Physics, Tampere University of Technology, P.O. Box 692, FI-33101 Tampere, Finland

*Corresponding author: jaakko.saarela@tut.fi

Received 20 October 2008; accepted 5 December 2008; posted 17 December 2008 (Doc. ID 102920); published 23 January 2009

Different wavelength modulation waveforms were studied comprehensively in tunable diode laser photoacoustic spectroscopy. The generation of the photoacoustic signal was studied by way of simulations and experiments. A cantilever-enhanced photoacoustic detector and CO_2 sample gas were used in the experiments. The modulation waveforms compared in this study were sinusoidal, triangular, shaped, and quasi-square waves. All four waveforms allow background-free detection of trace gases. Compared to the conventionally used sinusoidal modulation, the triangular, shaped, and quasi-square waves enhanced the photoacoustic signal by factors of 1.12, 1.42, and 1.57, respectively. © 2009 Optical Society of America

OCIS codes: 300.6260, 300.6430, 300.6380.

1. Introduction

Photoacoustic spectroscopy (PAS) is a sensitive tool for trace gas analysis. In the photoacoustic (PA) effect sample molecules absorb light that is modulated periodically. Because of inelastic collisions between molecules, a portion of the absorbed energy is released as heat to the environment. As a result, an acoustic wave is generated that is then detected with a microphone.

Ultrasensitive PAS techniques take advantage of cantilever-enhanced [1] and quartz-enhanced [2] detection. Very low detection limits have also been achieved with resonant PA cells and high-power lasers [3,4]. In the infrared region of the spectrum where most molecules have their fundamental vibrational bands, tunable, narrowband semiconductor lasers are preferred. Normalized noise-equivalent absorption (NNEA) is often used to compare different methods [5]. The smallest reported NNEA values are $1.9 \times 10^{-9}\,\mathrm{cm^{-1}\,WHz^{-1/2}}$ for quartz-enhanced PAS [2], $1.5 \times 10^{-9}\,\mathrm{cm^{-1}\,WHz^{-1/2}}$ for resonant PA detection [3], and $1.7 \times 10^{-10}\,\mathrm{cm^{-1}\,WHz^{-1/2}}$ for cantilever-enhanced PAS [5].

Usually, in tunable diode laser PAS (TDLPAS) the emission wavelength of the laser is scanned sinusoidally and symmetrically across the absorption line with a small modulation amplitude. During one scanning period the absorption line of the sample molecules is crossed twice. Thus, a nearly sinusoidal PA signal is generated at twice the modulation frequency ($2f_{\mathrm{mod}}$). In resonant detection the signal frequency is matched to the resonance of the PA detector. Because the walls and windows are broadband absorbers, the PA signal from sample gas is void of acoustic background. Therefore, the background-free wavelength modulation (WM) is often favored over amplitude modulation (AM), which suffers from an interfering background at the PA signal frequency.

In this work, the sensitivity of TDLPAS was studied with a cantilever-enhanced PA detector by using different modulation waveforms. Quasi-square [6], shaped, triangular, and sinusoidal waveforms were used. Conventionally, the sinusoidal modulation

0003-6935/09/040743-05$15.00/0

waveform is used, which is not the optimum choice for generation of a PA signal. The novel shaped modulation waveform is tailored for a specific absorption line to produce a sinusoidal PA signal. Compared to the sinusoidal modulation, the obtained results indicate that the triangular, shaped, and quasi-square modulation waveforms improve the PA signal by factors of 1.12, 1.42, and 1.57, respectively. The quasi-square waveform (QSW) gives the largest signal-to-noise ratio (SNR) due to the largest $2f_{\mathrm{mod}}$ frequency component in the PA signal.

2. Experimental Setup

A custom nonresonant photoacoustic detector (Gasera Ltd., Turku, Finland) was used in the laboratory experiments. The pressure transducer is a flexible, rectangular cantilever (length 6 mm, width 1.5 mm, and thickness 10 μm), whose bending motion is measured optically with a Michelson interferometer. The cantilever resembles a damped harmonic oscillator. Its vibrational amplitude is directly proportional to the pressure but is also defined by the modulation frequency and the mechanical properties of the detector, which contribute to the sensitivity of the device [1,7]. The inner diameter and the length of the photoacoustic cell were 3 mm and 42 mm, respectively.

Carbon dioxide (CO_2), with a concentration of 5000 ppm in nitrogen (N_2), was used as the sample gas in normal environment [normal temperature and pressure (NTP)] conditions. The measurement setup is shown in Fig. 1. A temperature controller (LDT 5525, ILX Lightwave, Bozeman, Montana) was used for temperature stabilization and coarse wavelength tuning of a distributed-feedback (DFB) diode laser (FOL 15DCWD-A81-19060, Furukawa Electric, Tokyo, Japan). A diode laser current controller (LDX-3320, ILX Lightwave) was modulated by a programmable function generator (33250A, Agilent Technologies, Santa Clara, California) for fine tuning of the laser wavelength. The DFB diode laser has a current tuning parameter of 7.6×10^{-3} nm/mA. The diameter of the collimated laser beam was approximately 1 mm and the average power was 30 mW.

3. Formation of Photoacoustic Signal

In TDLPAS the $2f_{\mathrm{mod}}$ frequency component is extracted from an amplitude spectrum of the PA signal. The amplitude at the signal frequency is a product of

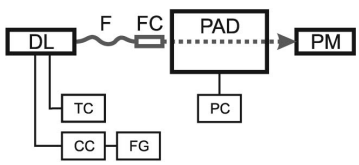

Fig. 1. Measurement setup: DL, fiber-pigtailed DFB diode laser; F, optical fiber; FC, fiber collimator; PAD, photoacoustic detector; PM, powermeter; TC, temperature controller; CC, current controller; FG, function generator; and PC, personal computer. The gas exchange system is not shown.

the detector sensitivity, the absorption coefficient of the gas, and the laser power [8]. The signal depends also on the manner in which the laser wavelength is tuned across the absorption line.

In semiconductor diode lasers the wavelength is usually tuned by adjusting the injection current. A sinusoidal, small-amplitude tuning across the absorption line center produces an acoustic signal, having most of the energy at frequency $2f_{\mathrm{mod}}$. However, when the amplitude of the tuning is increased, harmonic frequencies of $2f_{\mathrm{mod}}$ are added to the signal and the signal is no longer sinusoidal. This is caused by the nonlinear-shaped absorption profile, which is modeled with a Voigt function in general. Furthermore, if the amplitude of the sinusoidal modulation is increased beyond a certain range, the $2f_{\mathrm{mod}}$ signal component saturates and begins to decrease [9–12].

The magnitude of modulation is often described with a unitless modulation index, also referred to as a modulation depth. The modulation index is defined as a peak-to-peak modulation amplitude divided by the absorption linewidth (FWHM) of the molecule [6]. Intuitively, the PA signal would reach its maximum when the modulation index is much larger than 1. With a large modulation index the absorption is varied between zero and the maximum value at the line center. For the sinusoidal modulation the optimum modulation index is about 2.2 [6]. Beyond this value a remarkable portion of the $2f_{\mathrm{mod}}$ signal is redistributed to the higher harmonics. Thus, the best choice is to use the optimum modulation index and to measure only the $2f_{\mathrm{mod}}$ component, which usually has the best SNR.

One way to improve the $2f_{\mathrm{mod}}$ signal component is by using a novel shaped modulation waveform. Under an assumption of a very narrow laser line and weak absorption, the PA signal is directly proportional to the absorption coefficient of the sample gas at the laser frequency, $\alpha(\nu_L - \nu_0)$. The absorption profile can be determined experimentally with a linear wavelength scan. However, in this work, the absorption profile was calculated from the known line-broadening parameters of CO_2. Once the shape of the absorption is known, one can tailor a shaped modulation waveform that yields a pure sinusoidal PA signal in TDLPAS. The shaped modulation waveform and its PA response is shown in Fig. 2. A PA response for a linear, triangular modulation waveform is also shown. For simplicity, the frequency response of the PA detector was omitted in the simulations. The shaped waveform in Fig. 2 was calculated from an assumed Voigt-like absorption of CO_2, which is a convolution of Lorentz and Doppler profiles. At the transition wavelength of 1572 nm, i.e., at 6361 cm^{-1}, and in normal environment, the linewidth (FWHM) of the pressure-broadened Lorentzian is 0.1428 cm^{-1} [13], whereas the Doppler linewidth [14] is only 0.0118 cm^{-1}. Thus, the Voigt profile resembles a Lorentzian closely. The absorption cross section at the line center is 7.5×10^{-23} cm^2/molecule.

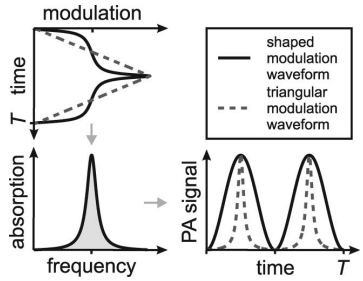

Fig. 2. Simulated PA signals with triangular and shaped modulation waveforms. The modulation index, i.e., the peak-to-peak modulation amplitude with respect to the absorption linewidth (FWHM), is 10. Triangular scan yields a pure absorption spectrum from which the shaped modulation waveform is calculated. The shaped modulation waveform produces a pure sinusoidal PA signal with all the absorbed energy concentrated into a single signal frequency.

4. Results and Discussion

The PA responses of four different modulation waveforms, a quasi-square, shaped, triangular, and sinusoidal, were compared by way of simulations and experiments. The quasi-square wave, which was originally introduced [6] and implemented [15] for wavelength modulation in absorption spectroscopy, is a symmetric, three-level staircase. The laser frequency switches between the values $\nu_0 - \Delta\nu$, ν_0, and $\nu_0 + \Delta\nu$, where $\Delta\nu$ is the modulation amplitude, in such a way that the absorption maximum is crossed twice during a modulation period.

Experimental PA spectra, recorded for the different modulation waveforms, are presented in Fig. 3.

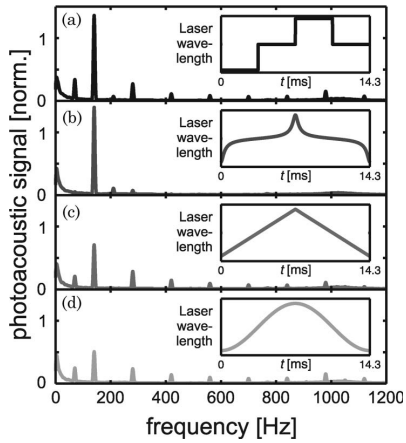

Fig. 3. Typical amplitude spectra of measured PA signals with a large laser modulation index, being about 10 in these spectra. The modulation waveforms are (a) quasi-square wave (QSW), (b) shaped wave, (c) triangular wave, and (d) sinusoidal wave, which are shown in the insets. The fundamental PA signal frequency $2f_{\mathrm{mod}} = 140$ Hz. The spectra are normalized with an amplitude that is produced by the sinusoidal modulation at an optimum modulation index of 2.2.

The insets show one period of each modulation waveform. The modulation frequency was set to 70 Hz. Thus, the fundamental $2f_{\mathrm{mod}}$ signal frequency was 140 Hz. Several higher harmonics of $2f_{\mathrm{mod}}$ are seen below the resonance frequency of the cantilever (1 kHz), beyond which the PA response of the detector is substantially reduced. Each PA spectrum in Fig. 3 is an average of 100 fast Fourier transform (FFT) spectra, each of which is calculated from a PA signal of 300 ms in duration. The laser wavelength was scanned symmetrically across the rotational absorption line with a modulation index of about 10. The modulation index was determined by multiplying the laser tuning parameter with the peak-to-peak current modulation amplitude and dividing that by the known linewidth (FWHM) of the Voigt-shaped absorption profile.

Fourier analysis and background measurements, not shown, prove that all four waveforms are background-free at $2f_{\mathrm{mod}}$. The PA signal itself is generated at even harmonics of f_{mod}, i.e., at $2f_{\mathrm{mod}}$, $4f_{\mathrm{mod}}$ etc. Despite the fact that the current modulation of a diode laser always produces a combined AM–WM, all the waveforms generate a background signal at odd harmonics. The reason for this is that symmetric waveforms consist only of odd harmonics.

The effect of the modulation amplitude was studied experimentally by varying the modulation index between the values of 0.34 and 14.8. A PA spectrum was recorded for each modulation index and waveform. The measured amplitude values at $2f_{\mathrm{mod}}$ as a function of modulation index are presented as dots in Fig. 4. The solid curves are simulated signal amplitudes where an ideal WM is assumed. The calculated curves for the quasi-square, triangular, and sine waves are similar, as presented in Iguchi's work [6]. Both the measured and the simulated curves are normalized with the maximum responses of the sinusoidal excitation at $2f_{\mathrm{mod}}$.

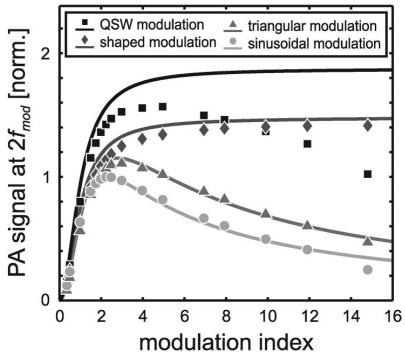

Fig. 4. Measured (dots) and simulated (solid curves) PA signal amplitudes, produced by the four modulation waveforms, at the frequency of $2f_{\mathrm{mod}}$. Pure WM was assumed in the simulations. Wavelength chirp of the diode laser increases with increasing modulation index. Because the QSW modulation suffers the most from the chirp, there is a discrepancy between the modeled and the observed curves at large modulation indices.

The QSW modulation produces approximately an 11% signal improvement compared to the shaped modulation, and nearly 41% and 57% enhancements relative to both triangular and sinusoidal modulations, respectively. With the shaped modulation, the signal level reaches a plateau, whereas sinusoidal, triangular, and quasi-square waveforms give rise to local maxima at modulation indices of 2.2, 3, and 5, respectively. The novel shaped modulation suppressed higher harmonic frequencies very efficiently and it increased the PA signal at $2f_{\mathrm{mod}}$ with 42% relative to the sinusoidal modulation. This means a reduction of the detection limit by a factor of 0.7 compared to the limit with optimum sinusoidal modulation. Correspondingly, the QSW modulation reduced the detection limit by a factor of 0.6. The results are summarized in Table 1.

Iguchi has shown theoretically that, in absorption WMS, the second harmonic signal with a sinusoidal modulation, at the line center of a Lorentzian profile, reaches its maximum at a modulation index of about 2.2. In the same article the optimum modulation index for a triangular wave was about 2.8. The QSW modulation gives an absorption enhancement of about 90%, which remains constant at large modulation indices. The QSW modulation produces a square wave absorption and, therefore, has the largest $2f_{\mathrm{mod}}$ signal component [6].

The absorption waveforms are the same in both WMS and TDLPAS at the line center. In Fig. 4 the detected amplitude as a function of modulation index with the sinusoidal and triangular waveforms are the same as reported for WMS. However, the experimental curve with the QSW modulation is different at large modulation indices. According to the simulations, the QSW modulation should enhance the signal with about 84%, whereas the enhancement achieved experimentally in this work was only 57%. The discrepancy and the decreasing response of the QSW modulation is due to the fact that the wavelength of the DFB diode laser chirps. During a step modulation the wavelength tuning is not instantaneous but is delayed. Chirping is a well-known effect with DFB diode lasers and, depending on the laser characteristics, the thermal setting times can vary from submicroseconds to several milliseconds, whereas the photon density in the active region is set to within a few nanoseconds [16,17]. Interferometric measurements showed that the wavelength of the DFB diode laser used in this work tuned exponentially to the resonance with a time constant of 0.4 ms, independent of the current modulation step. With 70 Hz QSW modulation, the modulation current is constant for 3.6 ms. Thus, the larger the modulation index, the longer it takes to reach the maximum absorption. Therefore, the absorbed power as a function of time is a distorted square wave whose amplitude at $2f_{\mathrm{mod}}$ decreases with increasing modulation index. The wavelength chirp was less significant at $2f_{\mathrm{mod}}$ below 20 Hz. However, at such low frequencies the background noise from building vibrations is increased, decreasing the SNR of the PA detection. Optimum modulation frequencies of each modulation waveform were not explored in this study. Neither was the sensitivity of the PA detector optimized.

In contrast to the QSW modulation, all the other modulation waveforms produced PA signals as predicted by the simulations. These waveforms do not show discontinuities that are prone to chirp. However, the wavelength chirp can explain why a small portion of the PA signal, with the novel shaped modulation waveform, was redistributed to $4f_{\mathrm{mod}}$ even though chirp occurs mainly far away from the absorption maximum. The reduced effect of the chirp, the insensitivity to the magnitude of the modulation current, and the enhanced sensitivity, compared to the sinusoidal modulation, make the shaped modulation waveform attractive for PA devices.

Despite the fact that a nonresonant PA detector was used in this research, the results are applicable to all kinds of PA device. This is assumed because the PA signal is always directly proportional to the absorbed power. Therefore, in a resonant PA cell, the different waveforms will generate standing pressure waves with similar relative strengths, as shown in Table 1. At very low modulation frequencies or with diode lasers, which exhibit negligible wavelength chirp, the QSW modulation waveform can nearly double the PA signal compared to the sinusoidal modulation. If AM has to be used instead of WM, as with gases absorbing within a broad wavelength band, the obtained results are not directly applicable. In the AM case, a simple square wave, with a duty cycle of 50%, will produce the largest signal because it has the largest $1f_{\mathrm{mod}}$ frequency component.

Table 1. Experimental Results with Different Modulation Waveforms Using $f_{\mathrm{mod}} = 70$ Hz and $f_{\mathrm{sig}} = 2f_{\mathrm{mod}} = 140$ Hz

	Waveforms			
	Quasi-Square	Shaped	Triangular	Sinusoidal
PA signal [norm.][a]	1.57[b]	1.42	1.12	1.00
CO_2 detection limit [ppm]	57	63	80	90
NNEA [10^{-8} cm^{-1} WHz$^{-1/2}$]	0.85	0.94	1.20	1.35
Optimum modulation index	5.0	≥8	3.0	2.2

[a]The PA signals are normalized with the maximum signal produced by the sinusoidal modulation at the optimum modulation index of 2.2.

[b]Simulated prediction is 1.84, which was not achieved experimentally because of the wavelength chirp of the DFB diode laser.

5. Conclusions

Photoacoustic spectroscopy is an established method for trace gas analysis. In the infrared part of the spectrum, where molecules have narrow absorption lines, the PA signal is preferably excited with tunable, single-mode semiconductor lasers. The wavelength scanning enables a background-free PA detection at the signal frequency of $2f_{\mathrm{mod}}$.

Usually, sinusoidal wavelength modulation is preferred due to its simple use. There are, however, other modulation waveforms that enhance the sensitivity of the PA detector. In this research, four different modulation waveforms were studied by way of simulations and experiments. The waveforms were sinusoidal, triangular, shaped, and quasi-square waves. All the waveforms produce PA signals that are void of acoustic background, which is due to the light absorption at the cell windows and walls.

The shaped modulation waveform developed in this work takes into account the Voigt profile of absorption lines and produces a pure sinusoidal PA signal. Compared to the sinusoidal modulation, the novel waveform increased the signal by a factor of 1.42 when modulation indices larger than 8 were used. Correspondingly, the quasi-square waveform (QSW) produced 1.57 signal enhancement and reduction of the detection limit by a factor of 0.64. Ideally, the QSW modulation should increase the PA signal by a factor of 1.84. This was not achieved because the laser exhibited relatively slow wavelength tuning under the QSW modulation.

The findings of this work apply to all PA systems where wavelength modulation is employed. The QSW modulation gives the largest PA signal with lasers that exhibit negligible wavelength chirp at the modulation frequency used. The novel shaped modulation waveform is also a good choice because of the reduced effect of the chirp, the insensitivity to the magnitude of the modulation current, and the enhanced sensitivity compared to the conventionally used sinusoidal modulation.

References

1. V. Koskinen, J. Fonsen, K. Roth, and J. Kauppinen, "Progress in cantilever enhanced photoacoustic spectroscopy," Vib. Spectrosc. **48**, 16–21 (2008).
2. A. Kosterev, G. Wysocki, Y. Bakhirkin, S. So, R. Lewicki, M. Fraser, F. Tittel, and R. Curl, "Application of quantum cascade lasers to trace gas analysis," Appl. Phys. B **90**, 165–176 (2008).
3. M. E. Webber, M. Pushkarsky, and C. K. N. Patel, "Fiber-amplifier-enhanced photoacoustic spectroscopy with near-infrared tunable diode lasers," Appl. Opt. **42**, 2119–2126 (2003).
4. T. Fink, S. Büscher, R. Gäbler, Q. Yu, A. Dax, and W. Urban, "An improved CO_2 laser intracavity photoacoustic spectrometer for trace gas analysis," Rev. Sci. Instrum. **67**, 4000–4004 (1996).
5. V. Koskinen, J. Fonsen, K. Roth, and J. Kauppinen, "Cantilever enhanced photoacoustic detection of carbon dioxide using a tunable diode laser source," Appl. Phys. B **86**, 451–454 (2007).
6. T. Iguchi, "Modulation waveforms for second-harmonic detection with tunable diode lasers," J. Opt. Soc. Am. B **3**, 419–423 (1986).
7. J. Kauppinen, K. Wilcken, I. Kauppinen, and V. Koskinen, "High sensitivity in gas analysis with photoacoustic detection," Microchem. J. **76**, 151–159 (2004).
8. V. S. Letokhov and V. P. Zharov, *Laser Optoacoustic Spectroscopy* (Springer-Verlag, 1986).
9. H. Cattaneo, T. Laurila, and R. Hernberg, "Photoacoustic detection of oxygen using cantilever enhanced technique," Appl. Phys. B **85**, 337–341 (2006).
10. G. Wysocki, A. Kosterev, and F. Tittel, "Influence of molecular relaxation dynamics on quartz-enhanced photoacoustic detection of CO_2 at $\lambda = 2\,\mu$m," Appl. Phys. B **85**, 301–306 (2006).
11. J.-P. Besson, S. Schilt, E. Rochat, and L. Thévenaz, "Ammonia trace measurements at ppb level based on near-IR photoacoustic spectroscopy," Appl. Phys. B **85**, 323–328 (2006).
12. R. Lewicki, G. Wysocki, A. Kosterev, and F. Tittel, "Carbon dioxide and ammonia detection using $2\,\mu$m diode laser based quartz-enhanced photoacoustic spectroscopy," Appl. Phys. B **87**, 157–162 (2007).
13. L. S. Rothman, D. Jacquemart, A. Barbe, D. C. Benner, M. Birk, L. R. Brown, M. R. Carleer, C. Chackerian, Jr., K. Chance, L. H. Coudert, V. Dana, V. M. Devi, J.-M. Flaud, R. R. Gamache, A. Goldman, J.-M. Hartmann, K. W. Jucks, A. G. Maki, J.-Y. Mandin, S. T. Massie, J. Orphal, A. Perrin, C. P. Rinsland, M. A. H. Smith, J. Tennyson, R. N. Tolchenov, R. A. Toth, J. Vander Auwera, P. Varanasi, and G. Wagner, "The HITRAN 2004 molecular spectroscopic database," J. Quant. Spectrosc. Radiat. Transfer **96**, 139–204 (2005).
14. O. Svelto, "Inhomogeneous broadening," in *Principles of Lasers*, 4th ed. (Springer, 1998), pp. 48–49.
15. A. Fried, J. Drummond, B. Henry, and J. Fox, "Versatile integrated tunable diode laser system for high precision: application for ambient measurements of OCS," Appl. Opt. **30**, 1916–1932 (1991).
16. M. Ito and T. Kimura, "Stationary and transient thermal properties of semiconductor laser diodes," IEEE J. Quantum Electron. **17**, 787–795 (1981).
17. W. Li, X. Li, and W.-P. Huang, "A traveling-wave model of laser diodes with consideration for thermal effects," Opt. Quantum Electron. **36**, 709–724 (2004).

Publication 2

Albert Manninen, Johan Sand, Jaakko Saarela, Tapio Sorvajärvi, Juha Toivonen, and Rolf Hernberg.

Electromechanical film as a photoacoustic transducer.

Optics Express **17**, 16994–16999 (2009)

Electromechanical film as a photoacoustic transducer

Albert Manninen[1]*, Johan Sand[1], Jaakko Saarela[1], Tapio Sorvajärvi[1], Juha Toivonen[1], and Rolf Hernberg[1,2]

[1]*Optics Laboratory, Department of Physics, Tampere University of Technology, P.O. Box 692, FI-33101 Tampere, Finland*
[2]*Deceased*
**albert.manninen@tut.fi*

Abstract: An electromechanical film, EMFi, is utilized as a transducer in a photoacoustic (PA) gas sensor. The film is a sensitive acoustic transducer, it is easily formable, and it exhibits a wide frequency response regardless of its large surface area. As a demonstration of its capabilities, the EMFi-based PA detector is used to measure NO_2 with pulsed excitation at 436 and 473 nm. The minimum detectable absorption coefficient is extrapolated to be $5 \cdot 10^{-7}$ cm^{-1}. Improvements for EMFi-based PA detector are discussed.

OCIS codes: (040.0040) Detectors; (300.6360) Spectroscopy, laser.

References and links

1. J. Stenberg, R. Hernberg, and J. Vattulainen, "Analysis of pollutant chemistry in combustion by in situ pulsed photoacoustic laser diagnostics," Appl. Opt. **34**(36), 8400–8408 (1995), http://ao.osa.org/abstract.cfm?URI=ao-34-36-8400.
2. H. A. Beck, R. Niessner, and C. Haisch, "Development and characterization of a mobile photoacoustic sensor for on-line soot emission monitoring in diesel exhaust gas," Anal. Bioanal. Chem. **375**(8), 1136–1143 (2003), http://dx.doi.org/10.1007/s00216-003-1810-8.
3. T. Schmid, "Photoacoustic spectroscopy for process analysis," Anal. Bioanal. Chem. **384**(5), 1071–1086 (2006), http://www.springerlink.com/content/p3762k758px0g825.
4. A. Bohren, and M. Sigrist, "Compact optical parametric oscillator based tunable mid-IR difference frequency laser spectrometer for intracavity photoacoustic trace gas sensing," in *Lasers and Electro-Optics, 1999. CLEO '99* pp. 190 – 191 (1999). *http://ieeexplore.ieee.org/search/wrapper.jsp?arnumber=834067*
5. M. Nägele, and M. Sigrist, "Mobile laser spectrometer with novel resonant multipass photoacoustic cell for tracegas sensing," Appl. Phys. B **70**, 895–901 (2000), http://www.springerlink.com/content/f54nkqlg6ppgbxkw/.
6. A. Rosencwaig, *Photoacoustics and Photoacoustic spectroscopy* (Robert E. Krieger Publishing Company, 1980) pp. 138.
7. M. Paajanen, J. Lekkala, and K. Kirjavainen, "ElectroMechanical Film (EMFi) - a new multipurpose electrets material," Sens. Actuators A Phys. **84**(1-2), 95–102 (2000), http://www.ingentaconnect.com/content/els/09244247/2000/00000084/00000001/art00269.
8. M. Paajanen, J. Lekkala, and H. Välimäki, "Electromechanical modeling and properties of the electret film EMFI," IEEE Trans. Dielectr. Electr. Insul. **8**(4), 629–636 (2001), http://ieeexplore.ieee.org/search/wrapper.jsp?arnumber=946715.
9. J. Hillenbrand, and G. M. Sessler, "High-sensitivity piezoelectric microphones based on stacked cellular polymer films (L)," Acoustical Society of America Journal **116**(6), 3267–3270 (2004).
10. V. P. Zharov, and V. S. Letokhov, *Laser Optoacoustic Spectroscopy* (Springer-Verlag, Berlin, 1986) pp. 112.
11. M. Paajanen, M. Wegener, and R. Gerhard-Multhaupt, "Understanding the role of the gas in the voids during corona charging of cellular electret films - a way to enhance their piezoelectricity," J. Phys. D Appl. Phys. **34**(16), 2482–2488 (2001), http://stacks.iop.org/0022-3727/34/2482.
12. V. Bovtun, J. Döring, J. Bartusch, U. Beck, A. Erhard, and Y. Yakymenko, "Ferroelectret non-contact ultrasonic transducers," Appl. Phys., A Mater. Sci. Process. **88**(4), 737–743 (2007), http://www.springerlink.com/content/3253n4610uk94818/.
13. J. L. Ealo, F. Seco, and A. R. Jimenez, "Broadband EMFi-based transducers for ultrasonic air applications," IEEE Trans. Ultrason. Ferroelectr. Freq. Control **55**(4), 919–929 (2008), http://ieeexplore.ieee.org/search/wrapper.jsp?arnumber=4494787.
14. A. Streicher, M. Kaltenbacher, R. Lerch, and H. Peremans, "Broadband EMFi Ultrasonic Transducer for Bat Research," in *2005 IEEE Ultrasonics Symposium* pp. 1629–1632 (2005). *http://ieeexplore.ieee.org/iel5/10674/33680/01603174.pdf?arnumber=1603174*
15. A. Streicher, R. Muller, H. Peremans, M. Katenbacher, and R. Lerch, "Ferroelectrets: ultrasonic transducer for a biomimetic sonar system," in *2004 IEEE Ultrasonics Symposium,* 1142–1145 (2004). *http://ieeexplore.ieee.org/search/wrapper.jsp?arnumber=1417982*

#113257 - $15.00 USD Received 23 Jun 2009; revised 25 Aug 2009; accepted 6 Sep 2009; published 9 Sep 2009

16. I. G. Calasso, and M. W. Sigrist, "Selection criteria for microphones used in pulsed nonresonant gas-phase photoacoustics," Rev. Sci. Instrum. **70**(12), 4569–4578 (1999), http://scitation.aip.org/getabs/servlet/GetabsServlet?prog=normal&id=RSINAK000070000012004569000001&idtype=cvips&gifs=yes.
17. S. Schäfer, A. Miklós, and P. Hess, "Quantitative signal analysis in pulsed resonant photoacoustics," Appl. Opt. **36**(15), 3202–3211 (1997), http://ao.osa.org/abstract.cfm?URI=ao-36-15-3202.
18. A. C. Vandaele, C. Hermans, P. C. Simon, M. Roozendael, J. M. Guilmot, M. Carleer, and R. Colin, "Fourier transform measurement of NO2 absorption cross-section in the visible range at room temperature," J. Atmos. Chem. **25**(3), 289–305 (1996), http://www.springerlink.com/content/l4521j3t0w962533.

1. Introduction

Trace gas detection is important in medical, industrial, and environmental research and monitoring. Emission standards for industry and energy production plants generate necessity for sensitive gas detectors. In situ gas detection provides valuable information for better understanding and optimizing the industrial processes. Trace gas detection is also a noninvasive diagnostic method for medical science. Photoacoustic spectroscopy (PAS) is generally considered as one of the most sensitive gas detection methods. A resent development of inexpensive but powerful laser light sources as well as a relatively simple implementation of the photoacoustic (PA) instrumentation makes PAS-based gas detector attractive for different applications. PA gas detector can also be used for in situ, real-time gas analysis during the industrial process [1–3]. Detection principle of the PA detectors is based on an excitation of the sample by the light and a detection of the thermal relaxation-induced pressure difference. The detection of the pressure difference, i.e. an acoustic wave, is based on an acoustic transducer. Conventionally, a microphone is used as the transducer. The microphone acts as a point detector for the pressure signal. However, the laser induced acoustic wave possess a cylindrically shaped wavefront, therefore, the planar microphone is not shaped optimally for the detection of the acoustical wave. Exploiting the acoustical resonances of the cylindrical gas cell require high signal frequencies up to tens of kHz to be detected. Some suggestions for the detection of cylindrical waveforms are published in literature. A tubular array of up to 80 microphones is used with a cylindrical PA cell [4,5]. In another application, an electret foil was wrapped around a metal tube, having closely spaced holes [6]. The Q value of the machined cell was around 30 at the resonance.

In this work, electromechanical film (EMFi), also referred to as EMFIT film [7,8], is used as a PA transducer. EMFi is thin and flexible cellular polypropylene film, having permanent internal charge. When external force is introduced onto the EMFi, an induced mirror charge is collected from metalized surfaces of the film. EMFi is durable, inexpensive, formable, and has a very wide frequency response of up to hundreds of kHz. Stacking films together increases sensitivity of the transducer [9]. Formability of the film enables utilization of a large area cylindrical acoustic transducer. An acoustic noise of a turbulent gas flow is mostly occurring below 2 kHz [10]. The use of flowing samples is possible with EMFi, due to the wide frequency response of the film. As a demonstration of its capabilities, a detection limit of 27 ppb of NO_2 in nitrogen is extrapolated from flowing gas measurements.

2. Electromechanical film in photoacoustics

The EMFi is typically 70 μm thick polypropylene film with voided internal structure. The film is corona charged during the manufacturing process. The permanent charges are located on the surfaces of the air voids. Both sides of the film are metalized to form electrical contacts. As an external force is introduced to the film, the voids are compressed and the opposite charges are brought closer together. Thus, a mirror charge is collected from the metalized surfaces. The electromechanical effect is related to the voided structure of the EMFi, rather than the piezoelectricity of the material itself. The sensitivity of the EMFi is often expressed with the piezoelectric coefficient d_{33} in pCN^{-1} units [7]. The porous structure of the film enables sensitivities up to 790 pCN^{-1} [11]. The sensitivity of the EMFi, used in this study, is estimated to be about 140–150 pCN^{-1}. The sensitivities of conventional piezoelectric films like PVDF, PZT-polymer composite and ceramic PZT are in the range of 20-600 pCN^{-1},

#113257 - $15.00 USD Received 23 Jun 2009; revised 25 Aug 2009; accepted 6 Sep 2009; published 9 Sep 2009

whereas the coupling factors of the piezoelectric films are higher than for EMFi [12]. An acoustic impedance of EMFi is two orders of magnitude smaller than that of traditional piezoelectric films and thus it is better matched with the ambient air. A figure of merit, describing the efficiency of a transducer film in air-coupled applications, is 165 for EMFi, 42 for composite PZT and less than 1 for PVDF and ceramics PZT [12]. The reported sensitivity of EMFi is 2.2 $mVPa^{-1}$ [9], which is comparable to 1 $mVPa^{-1}$ of commercial (B&K type 4138) 140 kHz frequency bandwidth condenser microphone. The sensitivities of commercial Knowles electret microphones are in order of 10 $mVPa^{-1}$, whereas the bandwidth of this type of microphones is limited to 10-20 kHz.

Previously EMFi was used for ultrasonic applications in air [12,13], for an artificial bat head [14], for keyboards, loudspeakers, medical monitoring, and a number of other applications [7]. The diversity of the applications can be explained by the properties of the film. The film is flexible, durable, sensitive, and has wide frequency response up to hundreds of kilohertz. The sensitivity can be further enhanced by stacking the films together. The frequency response of the EMFi is flat and wide. A single-layer film has resonance frequency at about 300 kHz, whereas the resonance frequency of the double-layer stack is reduced to about 70-90 kHz [15]. Increasing the size of the transducer increases the total detected acoustical energy. The size of traditional microphones is fixed, whereas the size of the EMFi can be altered without a reduction of the frequency bandwidth. The large size of the film can be exploited in PA applications to maximize the transducer area inside the PA cell.

The laser beam induces a cylindrically shaped acoustic wave. Thus, cylindrical cells are often used in PA applications, especially when acoustical resonances of the cell are exploited for the signal amplification. In this work, a simple 100 mm long iron tube with 18.5 mm radius is used as PA cell. Windows are placed at the ends of the tube. A two-layer EMFi is glued inside the tube covering half of the cylinder, as is shown in Fig. 1. To be able to measure azimuthal modes of the cell, the second half of the inner surface is left bare. Since the best signal to noise ratio (SNR) in our case is achieved with radial resonances, the azimuthal modes are only used for aligning the laser beam. Minimizing the azimuthal modes ensures centrosymmetric beam path inside the PA cell. The sensitivity of the detector could be nearly doubled just by coating the whole inner surface of the tube with the film. The EMFi transducer is attached to the cell with epoxy glue, whereas the films are attached to each other and to electrical contacts with a conductive epoxy. A self-made amplifier is used to amplify the output current signal of the film. The amplified signal is averaged and recorded with a digital oscilloscope (WaveRunner6100A, LeCroy) for further data processing.

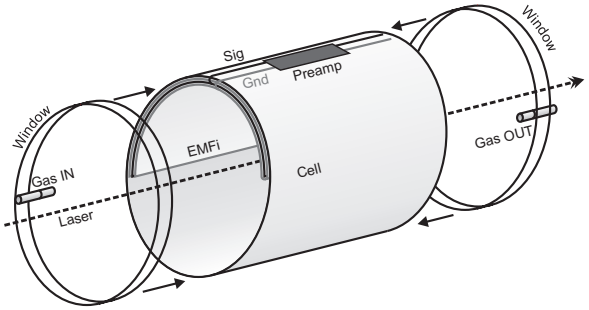

Fig. 1. Photoacoustic cell with EMFi transducer. An upper half of the inner surface of the iron tube is coated with a double layer EMFi. Ground (Gnd) and signal (Sig) contacts to preamplifier (Preamp) are located on the top of the cell.

The performance of the PA instrumentation was demonstrated with 5–45 ppm of NO_2 in nitrogen as a sample gas at atmospheric pressure. The sample gas of 186 ppm of NO_2 in nitrogen was diluted with pure N_2 by a mass flow controller (5850S, Brooks Instrument). A pulsed OPO laser (NT342/1/UVE, Ekspla) operating at 10 Hz repetition rate, having the tuning range of 210–2300 nm, was used as a light source. Excitation wavelengths of 436 nm

#113257 - $15.00 USD Received 23 Jun 2009; revised 25 Aug 2009; accepted 6 Sep 2009; published 9 Sep 2009

and 473 nm were used with average pulse energies of 5.8 mJ and 4.6 mJ, respectively. The pulse duration of the laser was 5 ns. The laser beam diameter was about 1 mm. The short laser pulse excites a broadband acoustical pulse [16], thus the characterization of the cell resonances was performed with a pulsed excitation.

3. Results and discussion

An averaged photoacoustic signal from 5 ppm of NO_2 in N_2 both in time and in frequency domains are shown in Fig. 2. The detectable acoustic wave, shown in the inset of Fig. 2, resonates in the PA cell for about 10 ms. The Q-switched laser produced a high amplitude electrical noise at the beginning of the signal, thus a smooth but stiff window function was used to clean the beginning of PA signal during the signal processing. Also PA signal after 10 ms was reduced with exponentially decaying window function. PA signal was then normalized with the corresponding average pulse energy and transformed into the frequency domain with Fourier transform (FT). The dumped acoustic resonance vanishes from the recorded signal after about 10 ms. Therefore, a zero padding property of FT was applied to continue the time domain signal with zeros to 200 ms. The frequency range of the detector was mostly limited by the self-made preamplifier. Therefore, the highest SNR of the responses is located at around 60 kHz. The Q-value for the 6th radial resonance at 59.2 kHz is over 1180 when the Q-value is defined as the frequency of the mode divided by the full width at half-maximum, FWHM of power spectrum [17]. First ten radial modes are labeled in the Fig. 2 and can clearly be distinguished below 100 kHz. Other peaks in the frequency spectrum in between the radial modes are azimuthal, longitudinal and combinations of the resonance modes. Existence of these extra modes is originated from the unideal shape and direction of the laser beam.

The recording time of an individual signal was 20 ms. However, due to the static electrical noise, the time frame of the signal was windowed to about 10 ms. 100 signals were averaged in each measurement, resulting in a nominal measurement time of 1 s or a real measurement time of 10 s, if 10 Hz repetition rate of the laser is taken into account.

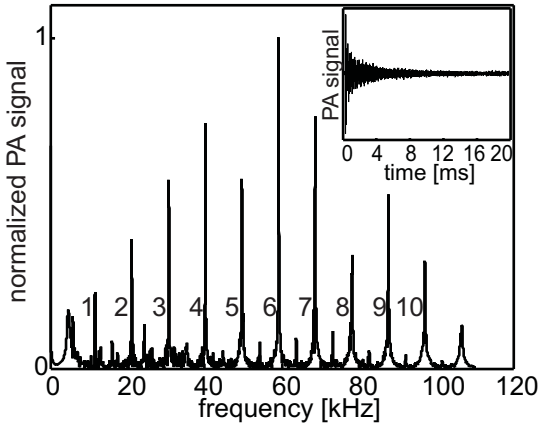

Fig. 2. Averaged PA signal of 5 ppm NO_2, excited at 473 nm. Main figure: frequency domain, first ten radial eigenmodes labeled. Inset: PA signal in time domain.

PA signal is linearly dependent on the sample gas concentration. The linearity of our detector was measured at the concentrations from 5 ppm to 45 ppm. Nitrogen dioxide tend to stick on the surfaces, thus a high total flow of 5 $Lmin^{-1}$ was used. Since the acoustical noise from airflow is generated well below 10 kHz, the PA measurements at around 60 kHz were not affected by the acoustic noise. The measured PA signal as a function of concentration is shown in Fig. 3. The signal levels are determined from the peak of the 6th radial mode. The measured signals show linear dependence of the PA signal on the sample gas concentration within the measured range. We were unable to reliably generate sample gas with

#113257 - $15.00 USD Received 23 Jun 2009; revised 25 Aug 2009; accepted 6 Sep 2009; published 9 Sep 2009

concentrations less than 5 ppm, thus the sensitivity limit of the instrumentation had to be extrapolated from the presented data. The 42 ppb sensitivity limit of the instrumentation is reached at the crossing point of the linear fit and the rms noise level of the 6th radial mode. For the noise level measurements, PA cell was washed with pure nitrogen for several minutes. The noise level was determined by calculating rms values of 20 PA measurements, each having 100 averaged signals. All the measurement conditions were kept similar to the measurements of the NO_2 samples.

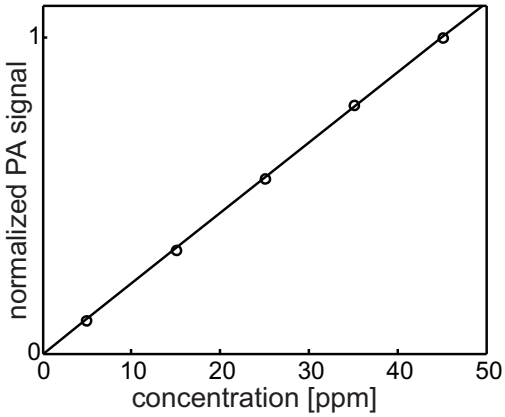

Fig. 3. Concentration measurements of NO_2 at 473 nm excitation. Circles: measured amplitudes of the 6th radial mode at 59.2 kHz, line: linear fit. Detection limit corresponding to $S/N_{rms} = 1$ is 42 ppb.

The absorption cross-sections of NO_2 [18] and the average pulse energies used are listed in Table 1. The measured SNR of the 6th radial mode from 5 ppm NO_2 at 436 nm is over 180, which correspond to 27 ppb detection limit of the instrumentation. Further lowering the wavelength is a trade-off between increasing the absorption cross-section and decreasing the pulse energies of our laser without overall SNR improvement. The sensitivity of the presented PA detector can be expressed as a minimum detectable absorption coefficient of $\alpha_{min} = 5 \cdot 10^{-7}$ cm^{-1}.

Table 1. Properties of NO_2 and corresponding laser pulse energies

Laser wavelength [nm]	Absorption cross-section [cm^2][a]	Average pulse energy [mJ]
436	$7 \cdot 10^{-19}$	5.8
473	$4 \cdot 10^{-19}$	4.6

[a]Literature values [18]

In this study, the performance of EMFi is demonstrated with a high-frequency PA cell. The presented instrumentation was designed to show the capabilities of the new transducer, rather than to optimize the gas detector. The sensitivity of EMFi-based detector can be improved in several ways. Highest reported sensitivity of EMFi is 790 pCN^{-1} [11], which is almost 6 times larger than the one used in this study. The whole inner surface of the resonator tube should be covered with the film, and also prolonging the resonator will increase the surface area of the EMFi. Stacking the films together will increase sensitivity and lower the resonance frequency of the transducer, if lower frequencies are preferred [9,15]. It would be advantageous to use the resonance frequency of the EMFi to maximize the signal. Proper focusing of the laser beam will produce the initial acoustic pulse with a peak frequency at the desired band [16]. The diameter of the PA cell can be fixed to produce 1st radial resonance at the same frequency. The pressure amplitude at the walls of the cylindrical PA cell is about 40% of the pressure amplitude in the middle of the cell for the 1st radial resonance mode [17].

#113257 - $15.00 USD Received 23 Jun 2009; revised 25 Aug 2009; accepted 6 Sep 2009; published 9 Sep 2009

The pressure amplitude at the walls is only 30% for the 2nd radial mode, 25% for the 3rd and is further reduced for higher resonances. Thus, the first radial mode is often preferred.

Some properties of EMFi are to be studied. The frequency response and SNR improvement of EMFi-based PA detector, as the film size and a number of layers in a stack are increased. Different cell geometry could be introduced to utilize multipass or cavity enhancement of excitation. Because EMFi is a whole new kind of acoustic transducer in gas phase PAS, fresh ideas for PA cell geometry can be implemented.

4. Conclusions

We have utilized EMFi transducer in PA detector for the first time. EMFi is flexible, durable, inexpensive, and regardless of its large size, combines relatively good sensitivity and a wide frequency response of hundreds of kilohertz. Compared to traditional microphones, formability of the film enables optimal detection of cylindrical acoustic waves inside the acoustic cell. The minimum detectable absorption coefficient of the presented gas detector is $\alpha_{min} = 5 \cdot 10^{-7}$ cm^{-1} for NO_2 in nitrogen at the atmospheric pressure and 436 nm excitation wavelength, which corresponds to the detection limit of 27 ppb. As the film is easily formable and stackable, geometry of PA detector can be completely rethought to take full advantage of the new transducer material.

Acknowledgements

Author acknowledges Mika Paajanen from VTT Technical Research Centre of Finland for providing us with EMFi samples. Author also acknowledges Graduate School of Modern Optics and Photonics for financial support, and Jukka Lekkala and Timo Salpavaara from Department of Automation Science and Engineering, Tampere University of Technology, for sharing their expertise in utilizing EMFi as an acoustic transducer.

#113257 - $15.00 USD Received 23 Jun 2009; revised 25 Aug 2009; accepted 6 Sep 2009; published 9 Sep 2009

Publication 3

Jaakko Saarela, Johan Sand, Tapio Sorvajärvi, Albert Manninen, and Juha Toivonen.

Transversely Excited Multipass Photoacoustic Cell Using Electromechanical Film as Microphone.

Sensors **10**, 5294–5307 (2010), featured in the
Special Issue of Laser Spectroscopy and Sensing.

Sensors **2010**, *10*, 5294-5307; doi:10.3390/s100605294

OPEN ACCESS

sensors

ISSN 1424-8220

www.mdpi.com/journal/sensors

Article

Transversely Excited Multipass Photoacoustic Cell Using Electromechanical Film as Microphone

Jaakko Saarela [1,⋆], Johan Sand [1], Tapio Sorvajärvi [1], Albert Manninen [1,2] and Juha Toivonen [1]

[1] Optics Laboratory, Department of Physics, Tampere University of Technology, P.O. Box 692, FI-33101 Tampere, Finland; E-Mails: johan.sand@tut.fi (J.S.); tapio.sorvajarvi@tut.fi (T.S.); juha.toivonen@tut.fi (J.T.)

[2] Empa, Swiss Federal Laboratories for Materials Science and Technology, Laboratory for Air Pollution & Environmental Technology, Überlandstr. 129, 8600 Dübendorf, Switzerland; E-Mail: Albert.Manninen@empa.ch

⋆ Author to whom correspondence should be addressed; E-Mail: jaakko.saarela@tut.fi; Tel.: +35-83-31153417; Fax: +35-83-31152600.

⋆ Author to whom correspondence should be addressed;

Received: 19 April 2010; in revised form: 21 May 2010 / Accepted: 24 May 2010 / Published: 26 May 2010

Abstract: A novel multipass photoacoustic cell with five stacked electromechanical films as a microphone has been constructed, tested and characterized. The photoacoustic cell is an open rectangular structure with two steel plates facing each other. The longitudinal acoustic resonances are excited transversely in an optical multipass configuration. A detection limit of 22 ppb (10^{-9}) was achieved for flowing NO_2 in N_2 at normal pressure by using the maximum of 70 laser beams between the resonator plates. The corresponding minimum detectable absorption and the normalized noise-equivalent absorption coefficients were 2.2×10^{-7} cm^{-1} and 3.2×10^{-9} cm^{-1}WHz$^{-1/2}$, respectively.

Keywords: multipass; photoacoustic; spectroscopy; longitudinal resonance; transversal excitation; transducer; electromechanical film microphone; EMFIT film

Classification: PACS 82.80.Kq; 07.88.+y; 07.07.Df; *43.20.Ks; 43.38.Kb; 77.55.H-

1. Introduction

Photoacoustic spectroscopy (PAS) is a sensitive technique for trace gas analysis. The photoacoustic (PA) technique is based on the detection of sound waves that are generated due to the absorption of modulated light. The acoustic wave is usually excited inside a closed cell, having larger dimensions than the wavelength of the acoustic wave. When the frequency of the acoustic wave is matched to the resonance frequency of the PA cell, the acoustic wave is amplified constructively by the quality (Q) factor of the resonance. The sound is detected with a transducer, such as a condenser, or an electret microphone [1]. Optical microphones [2] and quartz tuning forks [3] have also been used. Recently, an electromechanical film was also applied for PAS of gases [4].

The electromechanical film (EMFi or EMFIT film) is a flexible, approximately $70\ \mu\mathrm{m}$ thick, cellular polypropylene film with an internal charge [5]. The film has thin metal electrodes on its both sides. When a dynamic force is applied onto the film, opposite electric charges are generated on the two electrodes, from which the electric signal is measured. A single film layer has a wide frequency bandwidth with a flat response, even up to 300 kHz where the electromechanical resonance occurs. Below its resonance frequency the film has a sensitivity of about $2\ \mathrm{mVPa}^{-1}$. Furthermore, the films can be stacked to improve the sensitivity [6]. Due to the increased inertia of a film stack the resonance frequency reduces to tens of kilohertz [5,7] which, however, is usually above the operation frequencies of PA detectors.

Commonly, closed cylindrical PA cells are used together with radial, azimuthal, or longitudinal resonances. The Q values of cylindrical resonators are typically in the range of 10–1,000. Spherical resonators with even higher Q values have also been used. In cylindrical PA cells the radial resonances have their pressure maxima on the cylindrical axis. The optimum excitation of the radial resonances is achieved by aligning a small-diameter laser beam along the cylindrical axis [1].

In addition to the acoustic resonances, the PA signal can also be enhanced by optical multipass- or cavity-enhanced arrangements [8–17]. The increase of the sensitivity of a multipass PA system is based on the increased light absorption path length when the light beam is reflected multiple times through the sample volume. In intracavity systems the PA cell is placed inside a laser resonator [8–10]. On the other hand, in extracavity PA systems resonant optical cavities are seldom used because they need to be stabilized continuously and actively in order to maintain the optical resonance of the cavity. Instead, non-resonant multipass cavities are the most common.

In a Herriott-type multipass cavity the laser beam is introduced off-axially into a cavity, made of two mirrors, with the PA cell placed in between, so that the reflection of the beam occurs at a different spot after each roundtrip. The closer the beam family is to an antinode of a radial resonance of the PA cell, the better is the coupling of light energy into acoustic energy. However, due to the reflection losses of the mirrors, the PA signal enhancement is not directly proportional to number of roundtrips [11–13].

Optical multipass-enhancement of longitudinal acoustic modes has also been exploited. The laser beam can be introduced through a small aperture into a cylindrical PA cell, perpendicularly or transversally to the symmetry axis [14]. In this approach, the laser beam reflects multiple times from the inner metal walls of the PA cell until it is attenuated or exits through the entrance hole. Similar transversal illumination has been used in a Helmholtz resonator [15]. Absorbtion of light at the cell walls induces an

inherent PA background signal, especially if amplitude modulation is used instead of wavelength modulation.

The PA background signal and the reflection losses can be minimized simultaneously by using a windowless multipass PA cell where the laser beam is reflected between high-reflectivity mirrors that are outside the open PA cell. This kind of open configuration was used with a Herriott-type PA cell [11] and recently with a nonresonant PA cell that was aligned between two planar mirrors [18].

In this work, a 5-layer EMFIT film is applied as a transducer in a novel PA cell where both acoustic longitudinal resonances and optical multipasses are employed to enhance the sensitivity of the PA detector. The PA resonator is a simple rectangular structure with two steel plates, facing each other, and with open sides. The acoustic wave, which resonates between the plates, is excited transversally in an optical multipass configuration where the reflected laser beams lie in a plane, parallel to the plates. The optical multipass configuration, used in this research, was adopted from the previous study [18]. 308 ppm (10^{-6}) of nitrogen dioxide (NO_2) diluted in pure nitrogen (N_2) was used as a sample gas. The PA signal was excited within the visible rovibronic absorption band of NO_2, using amplitude-modulated blue laser light. The absorption cross-section of NO_2 at the 473 nm wavelength used was 4×10^{-19} cm^2 [19].

The sensitivity of the longitudinally resonant PA detector is compared with a cylindrical PA resonator that was used in a previous study [4]. It is demonstrated that the open longitudinal and the closed radial PA resonators give comparable sensitivities in a single pass measurement if they have the same Q values and similar EMFIT microphones. Additional PA signal improvement is achieved by multipassing the laser beam inside the transversally excited PA resonator. With a maximum of 70 laser beam passes a detection limit of 22 ppb of NO_2 in N_2 was achieved. This corresponds to a normalized noise-equivalent absorption coefficient (NNEA) of 3.2×10^{-9} cm^{-1}WHz$^{-1/2}$ which is close to the best values that have been measured with PA methods from a flowing gas sample. Future improvements of the PA detection of trace gases, using EMFIT film microphones, are discussed.

2. Experimental

2.1. Photoacoustic instrumentation and measurements

The schematic of the PA measurement set-up is shown in Figure 1a. A novel resonant photoacoustic cell with an optical multipass configuration was used in this work. The longitudinal PA resonator had rectangular steel plates (10 cm $\times$ 10 cm), facing each other 2.4 cm apart as is illustrated in Figure 1b. Five EMFIT films (Emfit Ltd., Vaajakoski, Finland), each of them having a size of 4 cm $\times$ 4 cm, were stacked together with a thin layer of epoxy-glue. The internal polarizations of the films were aligned parallel to each other so that the overall voltage across the capacitive film stack was the sum of the voltages of individual films. The film stack is an equivalent to capacitors, connected in series. Afterwards, the stack was glued onto the upper steel plate with electrically conducting epoxy so that the back plate served as one of the metal electrodes. Electrical connections from the steel plate and the front surface of the film stack were wired into an input of a self-made voltage amplifier, which had a 60 dB amplification.

Figure 1. (a) Measurement setup: diode-pumped solid state laser (DPSSL), multipass photoacoustic cell (MPAC), function generator (FG), radio frequency power source (RFS), acusto-optic modulator (AOM), data acquisition (DAQ), personal computer (PC), mirrors (M1–M4), aperture (A), cylindrical lenses (L1–L2), and spherical lenses (L3–L4). (b) Multipass photoacoustic cell (MPAC). The reflected laser beam generates an acoustic plane wave source and excites longitudinal acoustic resonances.

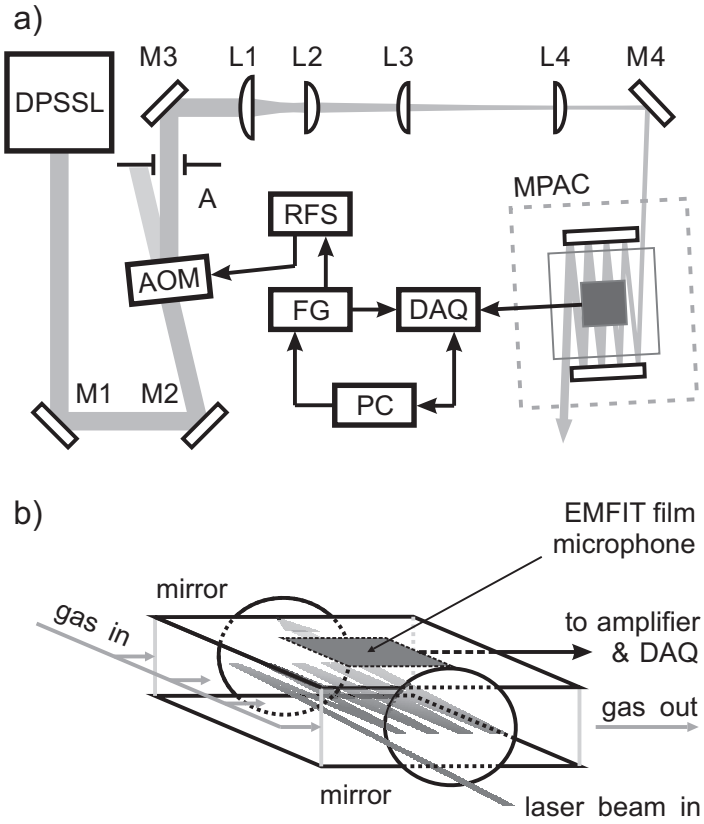

With the EMFIT film stack facing into the PA resonator, the two rectangular plates were separated with hollow 24-mm-long aluminum retainer tubes and tightened together with screws. Two broadband dielectric mirrors (ø = 50.8 mm, BB2-E02, Thorlabs) were placed on the opposite sides of PA resonator, forming an optical multipass cavity. The multipass PA cell (MPAC) was enclosed inside an aluminum box. The enclosure was equipped with windows as input and output ports for laser light. The NO_2 sample gas (308 ppm of NO_2 in N_2, AGA, Finland) was introduced into the sample volume of the MPAC through a teflon tubing whose terminal end was drilled with a row of small holes in order to guarantee a uniform input flow of the sample gas. The measured concentrations between 1–30 ppm were diluted from the certified 308 ppm NO_2–N_2 gas mixture with a cascade of two mass flow controllers (5850S, Brooks Instrument, Hatfield, PA, United States), whereas the concentrations of 30–308 ppm were generated with only one of the controllers. In order to maintain a stable gas flow through the cascade, a pressure relief valve was used between the two controllers.

An acusto-optic modulator (MT110-A1.5-VIS, AA Opto-Electronic, Orsay, France) was used to amplitude-modulate the laser beam that was emitted from a diode-pumped solid state laser (Cobolt Blues^{TM}, Cobolt AB, Stockholm, Sweden), having an emission power and wavelength of 40 mW and 473 nm, respectively. A radio-frequency power source (MODA110-B4-33, AA Opto-Electronic) provided a 110 MHz carrier wave to the acusto-optic modulator (AOM). The carrier wave was square-wave modulated with a programmable function generator (33250A, Agilent Technologies, Santa Clara, CA, United States) via a LabVIEW software. As a result, approximately 27 mW of optical peak power was achieved into the first diffraction order of the AOM. The modulation frequency of the output of the AOM can be tuned up to 32 MHz. However, in PA measurements only modulation frequencies of 0.1–60 kHz were used due to a limited frequency response of the microphone–amplifier circuit.

The amplitude-modulated laser beam was guided and focussed into the MPAC. In Figure 1 a L3 and L4 are spherical plano-convex lenses with focal lengths of 30 cm and 20 cm, which are used as a lens pair to collimate the slightly diverging laser beam. The lenses L1 and L2 are cylindrical plano-convex lenses, having 10 cm and 3 cm focal lengths. They had an effective focal length of 1.2 m, and they focussed the laser beam horizontally into the PA resonator, bypassing the first mirror of the MPAC. The size of the beam [full width at half maximum (FWHM)] at the entrance mirror was $0.2\ \mathrm{mm} \times 0.8\ \mathrm{mm}$ in the horizontal and vertical directions. The average laser power at the input of the MPAC was approximately 10 mW. The laser power was measured with a power meter (PD300-UV, Ophir Optronics Ltd., Jerusalem, Israel).

Due to the light absorption by NO_2 molecules, a pressure wave is generated at the modulation frequency of the plane of laser beams. The PA signal is measured as the output voltage of the amplifier with a high-speed digitizer (NI USB-5133, National Instruments, Austin, TX, United States), DAQ. The data acquisition is controlled and the measurement data is stored to a personal computer (PC) with same LabVIEW software that controls the function generator (FG). In the PA measurements typical data sampling frequencies (f_s) and data record lengths (T_m) were 250 kHz and about 2.1 s, respectively. Their product corresponds to a total of 2^{19} data points. A fast Fourier transform (FFT) was calculated from the collected PA signal data. In a FFT spectrum the even number of $2N$ data points, where N is a positive integer, are presented at frequencies $f_k = k \times \Delta f = k/T_m$, where $k = -N, ..., N-1$ [20]. When measuring the PA response of the MPAC as a function of frequency, the modulation frequencies of the laser beam were selected in such a way that they coincided with the frequencies $f_k \geq 0$, which were predetermined by f_s and T_m. The FFT spectrum was calculated after each PA measurement, using Hanning windowing, and only the root mean square (RMS) voltage at the modulation frequency is stored into the PC's hard disc for further data analysis.

2.2. Microphone response measurements

The sensitivity and the frequency response of the 5-layer EMFIT microphone was compared with a calibrated reference microphone (BK Type 4939, Brüel&Kjær Sound&Vibration Measurement A/S, Nærum, Denmark), which had a measurement bandwidth of 0–100 kHz. The signal from the reference microphone was first connected to a preamplifier (2670, Brüel&Kjær) and then to a programmable amplifier (SR650, Stanford Research System Inc., Sunnyvale, CA, United States) having a high-pass cut-off frequency and a gain factor of 100 Hz and 60 dB, respectively. The response of the 5-layer

film was also compared to that of a single film. A single EMFIT layer is known to exhibit response to sound waves up to 300 kHz. The operation of traditional loudspeakers that are used as calibration sound sources, are usually limited to audio frequencies.

The free-field responses of the three microphones were measured by PA means. Laser pulses from a Q-switched OPO laser system (NT342/1/UVE, Ekspla Ltd., Vilnius, Lithuania) were guided onto a solid steel sample at about 40° incidence. The pulse energy, duration, wavelength, and the diameter of the impact area were 60 mJ, 5 ns , 355 nm, and 5 mm, respectively. The high-intensity laser pulses heat the metal surface. A part of the heat is released to the surrounding air and, as a result, an acoustic pulse is emitted.

The acoustic pulse was measured with the three microphones, which were separated by 6 cm, at a distance of 1.8 m from the source. Thus, the microphones measured the acoustic far-field of the source roughly from the same solid angle. A thousand microphone signals were recorded and averaged with an oscilloscope (Waverunner6100A, LeCroy Co., Chestnut Ridge, NY, United States). In order to resolve acoustic frequencies of several hundreds of kHz, a sampling frequency of 2.5 MHz was used. The frequency responses were achieved by calculating FFT spectra from the measured data.

3. Results and Discussion

3.1. Microphone response

The acoustic response of the 5-layer EMFIT film microphone, used as the transducer in the PA measurements of NO_2, is compared to that of a commercial condenser microphone (BK Type 4939) in Figure 2. The response of a single film is also presented. The responses were measured by PA means as described in Subsection 2.2. It can be seen that the single EMFIT film has its electromechanical resonance at 280 kHz, whereas the resonance frequency of the 5-layer EMFIT stack is around 45 kHz. Below this frequency the film stack has approximately 4–5-fold sensitivity when compared to the sensitivity of the single film. Furthermore, the layered films give a signal that is comparable with that of the reference microphone whose reported sensitivity is 4.14 mV/Pa at 250 Hz.

The measured amplitude spectra of Figure 2 could be presented as absolute sensitivity curves by dividing them with the frequency distribution of the incident pressure wave. This, however, was not done because there are several local minima and maxima in the reference spectrum below 100 kHz which are not seen in the smoother spectra of the EMFIT films. The existence of these features is probably related to acoustic interference. Different frequency components exhibit different directionality patterns when the diameter of the source is comparable to the wavelength of sound [21], as now is the case at ultrasonic frequencies. Thus, the transducers are affected by the directionality and interference. Due to the large size of the EMFIT films, the interference is averaged out, and smoother spectra are measured than with the $1/4\,''$ reference microphone.

Figure 2. Photoacoustic response of a stack of 5-layer EMFIT film microphone in free field, compared with the responses of a 1-layer film and a reference condenser microphone. Due to the layering of the microphone films, the electromechanical resonance of the 5-layer microphone is reduced to 45 kHz from 280 kHz of the single microphone film. The layering enhances the microphone signal by a factor of 4–5 at low frequencies.

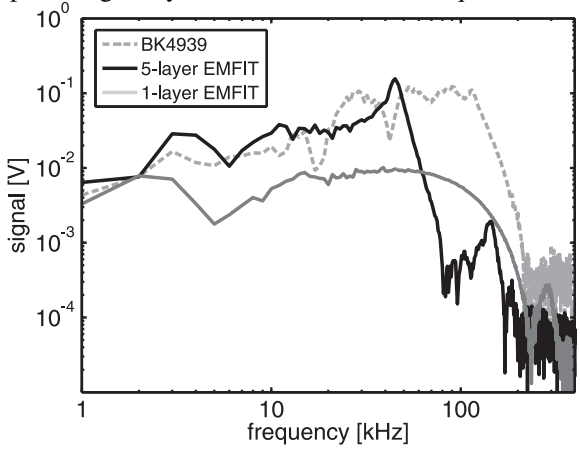

3.2. Performance of planar photoacoustic cell

The performance of the novel MPAC was compared with a cylindrical PA cell that was used in the previous study [4]. The cylindrical PA cell was optimized for the excitation of radial eigenmodes and for optical single pass measurement. The cylinder had a length and radius of 10 cm and 1.85 cm, respectively, and half of the inner surface was covered with a folded 2-layer EMFIT film. The 2nd radial resonance of the cell was at 21.06 kHz. In order to compare the performances of the planar MPAC and the cylindrical cell, the plate distance of the MPAC was adjusted to 1.6 cm to give a resonance frequency of 22.62 kHz for the 2nd longitudinal mode. In addition, the $10\ \mathrm{cm} \times 10\ \mathrm{cm}$ MPAC resonator was equipped with an EMFIT film of similar size and sensitivity as used in the cylindrical PA cell.

A cylindrical laser beam, having a diameter of 0.8 mm (FWHM), was aligned collinearly along the cylindrical axis of the PA cell. The spherical beam profile that is commonly achieved from laser sources, is ideal for the excitation of radial acoustic modes, whereas a wide rectangular profile would be the optimum beam shape for the planar longitudinal waves. A wide elliptical beam profile serves as a close approximation to the rectangular profile. Therefore, a short focal length cylindrical lens was used to divert the spherical, gaussian laser beam into an elliptical profile, having a minor and major axes of about 0.8 mm and 20 mm, respectively.

The initial pressure wave amplitudes of the two different PA cell types can be compared by normalizing their PA signals with the corresponding laser powers and Q values. The Q values of the 2nd order modes of the cylindrical and planar PA cells were about 530 and 220, respectively. The Q value was defined as a ratio of the resonance frequency and the width of the resonance profile at $2^{-1/2}$ height. Consequently, a difference of a factor of two in the initial amplitudes was found for the benefit of the cylindrical PA cell. This probably results from the more efficient PA coupling between the spherical laser beam and the radial mode, compared to the coupling between the elliptical beam and the longitudinal

mode. Nevertheless, with a single beam pass the sensitivity of the novel transversely excited planar PA cell was about 5 times lower than the sensitivity of the similar cylindrical PA cell with axial excitation.

3.3. Multipass photoacoustic measurements

The frequency response of the PA detector is presented in Figure 3. The 5-layer film microphone and its mounting plate were attached to the MPAC as the top plate of the resonator, and the plate separation was adjusted back to 2.4 cm. A plane of 21 laser beams was aligned parallel to the resonator plates. When the laser beams are located on the bottom of the PA resonator, all the longitudinal acoustic resonances can be excited. The fundamental longitudinal resonance occurs at 7.86 kHz, and the higher harmonics occur approximately at its multiples. On the other hand, when the beams are aligned along the central plane of symmetry only even harmonics can be excited. This is due to the fact that only even harmonics have an antinode in center of the resonator. Then, the induced pressure wave is amplified constructively as it oscillates between the resonator plates. Furthermore, the amplitudes of the even harmonics are maximized with central excitation because the up- and downwards propagating pressure waves, which are generated by the plane of laser beams, oscillate in phase with each other. The large scale spectra in Figure 3 a and b were measured with a resolution of 50 Hz. The spectrum in the inset, where the profile of the 2nd longitudinal eigenmode is shown, was measured with a resolution of 5 Hz. The Q value is 175 for the the PA cell with the 2.4 cm plate distance.

Figure 3. Acoustic resonances of the planar MPAC with the plane of multipassed laser beams lying horizontally (a) in the center and (b) at the bottom of the cell. The longitudinal resonances occur above 7.86 kHz. The 2nd longitudinal resonance at 14.87 kHz, having a Q value of 175, is shown in the inset. Only even longitudinal modes are excited when the laser beams are located in the center of PA cell.

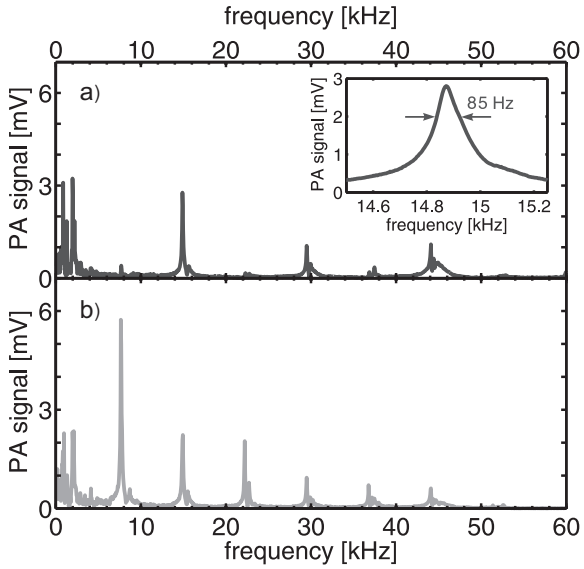

By measuring the peak value of the 2nd longitudinal resonance at 14.87 kHz as a function of gas flow, it was found out that the peak amplitude of the PA signal increases. This is probably due to the

fact that NO_2 is a polar molecule with a tendency of being adsorbed onto the tubing and walls of the PA cell. The PA signal remains nearly constant above 1.5 standard liters per minute (SLPM). However, the signal-to-noise ratio (SNR) started to decrease above 2 SLPM because the acoustic background noise, due to a turbulent gas flow, was increased. At the resonance frequency of the fundamental mode the flow noise is more dominating. Therefore, only 1 SLPM sample gas flow was used in measurements that are presented in Figure 3. The estimated NO_2 concentration in the MPAC was 20 ppm.

The cell constant of the MPAC is shown in Figure 4 as a function of number of laser beam passes with two different laser beam profiles. The collimated beam had a diameter of 0.8 mm. The horizontal width of the diverging beam was 0.2 mm at the entrance mirror of the MPAC, after which it diverts with a divergence angle of 0.6 mrad. At high number of laser beam passes the cell constant of the MPAC is about 10% larger with the diverging laser beam than with the collimated beam.

Figure 4. Cell constant of the PA cell as a function of laser beam passes. The total absorption of light by the NO_2 molecules was approximately 0.01 in each measurement. At high numbers of passes the horizontally diverging laser beam enhances the sensitivity of the planar MPAC, when compared to the response achieved with the collimated beam, due to the better directionality of the generated pressure wave.

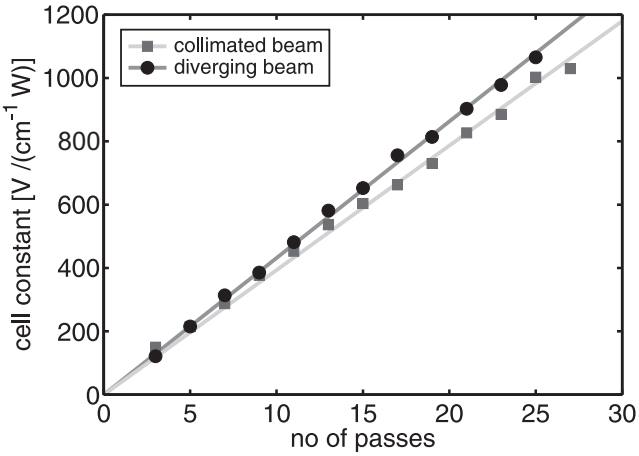

After 25 passes, for example, the width of the diverging laser beam was about 1.8 mm, whereas the width of the collimated beam remained at 0.8 mm. The beam spacing in the center of the planar PA resonator was about 1 mm with the 25 passes. Thus, the horizontally diverging beams overlap better with each other and generate an acoustic wave with a higher degree of directionality than with the spherical beams. A dense group of a large number of overlapping laser beams generates a uniform source for acoustic plane waves with negligible side lobes in the directionality pattern of the emitted sound. Instead, it is expected that a sparse group of separated beams produces a sound wave with prominent side lobes and a lower degree of directionality.

As the laser beams traverse diagonally as separate beams between the mirrors of MPAC with a low number of passes, it would be expected that the curves in Figure 4 showed a nonlinear dependence on the number of passes because of the changing directionality pattern. However, at the low number of passes, the reduced directionality of the generated sound wave is compensated by the increased, diagonal absorption path. Therefore, the measured dependencies of the cell constants in Figure 4 are fairly linear with both beam profiles.

By tilting the entrance mirror of the MPAC horizontally in such a way that the laser beam turns back between the mirrors, the number of beam passes is increased by more than a factor of two. About 70 passes were achieved, corresponding to cell constants of 3,120 VcmW^{-1} and 2,740 VcmW^{-1} with the diverging and the collimated beam, respectively.

The dielectric mirrors, used in the MPAC, had a 1-mm-wide, uncoated circular strip at the outer circumferences. The non-reflective areas limit the minimum spacing of the laser beams and, also, the maximum number of laser beam passes which can be achieved. On the other hand, the size and the divergence of the laser beam are also limiting factors. For example, with too high a divergence the light energy leaks easily from between the mirrors, and the PA signal enhancement is poor. The optimum beam divergence was not sought in this study. Instead, it was simply demonstrated that a horizontally diverging laser beam is a better choice for generating an acoustic plane wave than a collimated beam.

The PA signal as a function of NO_2 concentration is presented in Figure 5. The horizontally diverging laser beam was used, with the maximum number of 70 passes. Thus, the total absorption path length was 7 m inside the 10-cm-long PA resonator. Lower concentrations than 1 ppm were not diluted because of the nonlinear behavior of the mass flow controllers. The controllers had a linear dilution range approximately between 10%–100%. A curve of type $1 - \exp(-\alpha L)$, where α and L are the absorption coefficient and the total absorption path length, respectively, was fitted to the data of Figure 5. The equation describes the Beer–Lambert's law for total absorption and does not take into account for the reflection losses of the mirrors. At normal incidence the reflectivity of the dielectric mirrors was 99.8%. The curve seems to fit the PA signal data well even at high absorption levels. For example, the optical density at 30 ppm is high, about 0.21, and the decrease from the linear approximation of Beer–Lambert's law is about 10%. With a measurement time of 2.1 s the detection limit ($\mathrm{SNR} = 1$) of NO_2, diluted in N_2 in NTP (normal temperature and pressure) conditions, is extrapolated to 22 ppb. This corresponds to a minimum detectable absorption coefficient and NNEA value of 2.2×10^{-7} cm^{-1} and 3.2×10^{-9} cm^{-1}WHz$^{-1/2}$, respectively.

Our results are summarized and compared with the results of other single and multipass PA methods in Table 1. In the case that only the minimum detectable absorption coefficient or concentration was given in the reference literature, a calculated NNEA value is indicated in Table 1, or vice versa. Furthermore, only studies where continuous-wave (CW) or quasi-CW light sources were used, are referenced in Table 1 because the NNEA value cannot be defined for a PA cell where single-pulse excitation of the PA signal is used. In quasi-CW mode of operation the PA signal is excited with a train of short pulses whose repetition rate is matched to the resonance frequency of the PA cell. Optimally, the quasi-CW excitation enhances the PA signal by a factor of $\pi/2$ compared to the CW excitation with the same average optical power [22]. The NNEA value of 3.2×10^{-9} cm^{-1}WHz$^{-1/2}$, achieved in this study, is close to smallest values that have been achieved with other resonant PA cells.

Figure 5. Photoacoustic signal as a function of NO_2 concentration at the resonance frequency of the 2nd longitudinal mode. Central excitation with a diverging laser beam and about 70 passes was used. A simple curve, describing the Beer–Lambert's law, was fitted to the measured data. The noise level is 5.9 μV with 2.1 s measurement time, yielding a detection limit of 22 ppb for NO_2 in N_2.

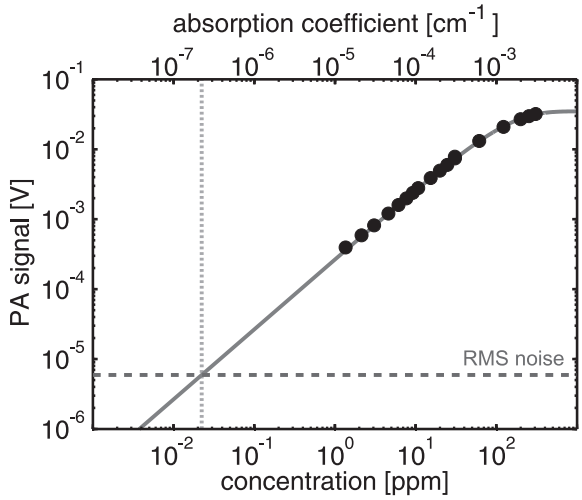

Table 1. Comparison of PA methods with different number of optical passes in PA cell. P_{laser}, t_{m}, α_{min}, and NNEA are the average laser power, measurement time, minimum detectable absorption coefficient, and normalized noise-equivalent absorption, respectively.

	Parameters				
Study	No of passes	P_{laser} [mW]	t_{m} [s]	α_{min}* $[10^{-8}\mathrm{cm}^{-1}]$	NNEA* $[10^{-9}\mathrm{cm}^{-1}\mathrm{WHz}^{-1/2}]$
This	70	10	2.1	22	3.2
[18]	10	126	0.3	2.6	1.8†
[12]	36	6,000	30	0.069	22.7†
[23]	2	500	10	0.95	1.5
[24]	1	6.6	1	40†	2.6
[25]	1	30	2.6	0.36‡	0.17‡

*For SNR = 1
†A calculated value
‡For nonflowing gas sample

In future, the sensitivity of the PA detector where EMFIT films are used as a microphone, can be improved by increasing the number of stacked film layers and by replacing the self-made amplifier with another of lower electrical noise. In addition, the PA signal could be enhanced by using EMFIT films with higher sensitivity and by matching the electromechanical resonance of the stacked EMFIT films to the acoustic resonance of the PA cell. In order to reduce the electromechanical resonance frequency to a

lower frequency than the 45 kHz, more than 5 layers need to be stacked. At a lower resonance frequency more efficient overlap between the laser beams and the standing pressure wave could also be achieved.

4. Conclusions

In this work, five stacked electromechanical films were applied as a transducer in a novel photoacoustic cell where both longitudinal acoustic resonances and optical multipasses were employed. The PA resonator was a simple rectangular structure with two steel plates, facing each other, and with open sides. The acoustic wave, resonating between the plates, was excited transversally in an optical multipass configuration. The laser beam, having a wavelength of $473\ \mathrm{nm}$, was reflected between two planar dielectric mirrors so that the beams lay in a plane, parallel to the resonator plates of the PA cell.

A detection limit of 22 ppb for NO_2 in N_2 was achieved with the maximum number of 70 laser beam passes inside the PA cell and by using a measurement time and an average optical power of 2.1 s and 10 mW, respectively. The minimum detectable absorption and the normalized noise-equivalent absorption coefficients were $2.2 \times 10^{-7}\ \mathrm{cm}^{-1}$ and $3.2 \times 10^{-9}\ \mathrm{cm}^{-1}\mathrm{WHz}^{-1/2}$, respectively.

A sample gas flow of up to 2 liters per minute was used without a significant increase of the acoustic background noise at the second longitudinal resonance of 14.87 kHz where the acoustic quality factor was 175. Furthermore, it was demonstrated that the novel PA cell gives a comparable PA signal with a single laser beam pass than a corresponding cylindrical PA cell that are commonly used. The PA signal is easily enhanced by using multiple laser beam passes inside the planar PA cell.

The achieved sensitivity is close to the best values, measured from flowing gas samples at normal pressure. The sensitivity of the multipass PA cell, where electromechanical films are used as a microphone, can be further enhanced by optimizing the number of layered films, by using a low-noise electronic preamplifier, and by exploiting the electromechanical resonance of the microphone.

Acknowledgements

Mika Paajanen (VTT Technical Research Centre of Finland) and Emfit Ltd. are acknowledged for providing the EMFIT films and for sharing their expertise in using the films as an acoustic transducer.

References

1. Miklós, A.; Hess, P.; Bozóki, Z. Application of acoustic resonators in photoacoustic trace gas analysis and metrology. *Rev. Sci. Instrum.* **2001**, *72*, 1937–1955.
2. Koskinen, V.; Fonsen, J.; Roth, K.; Kauppinen, J. Progress in cantilever enhanced photoacoustic spectroscopy. *Vibrat. Spectrosc.* **2008**, *48*, 16–21.
3. Kosterev, A.; Wysocki, G.; Bakhirkin, Y.; So, S.; Lewicki, R.; Fraser, M.; Tittel, F.; Curl, R. Application of quantum cascade lasers to trace gas analysis. *Appl. Phys. B* **2008**, *90*, 165–176.
4. Manninen, A.; Sand, J.; Saarela, J.; Sorvajärvi, T.; Toivonen, J.; Hernberg, R. Electromechanical film as a photoacoustic transducer. *Opt. Expr.* **2009**, *17*, 16994–16999.
5. Paajanen, M.; Lekkala, J.; Kirjavainen, K. ElectroMechanical Film (EMFi)—A new multipurpose electret material. *Sens. Actuat. A* **2000**, *84*, 95–102.

6. Hillenbrand, J.; Sessler, G.M. High-sensitivity piezoelectric microphones based on stacked cellular polymer films (L). *Acoust. Soc. Am. J.* **2004**, *116*, 3267–3270.
7. Bovtun, V.; Döring, J.; Bartusch, J.; Beck, U.; Erhard, A.; Yakymenko, Y. Ferroelectret non-contact ultrasonic transducers. *Appl. Phys. A* **2007**, *88*, 737–743.
8. Gerlach, R.; Amer, N. Brewster window and windowless resonant spectrophones for intracavity operation. *Appl. Phys. A: Mater. Sci. Process.* **1980**, *23*, 319–326.
9. Harren, F.J.M.; Bijnen, F.G.C.; Reuss, J.; Voesenek, L.A.C.J.; Blom, C.W.P.M. Sensitive intracavity photoacoustic measurements with a CO_2 waveguide laser. *Appl. Phys. B: Photophys. Laser Chem.* **1990**, *50*, 137–144.
10. Bijnen, F.G.C.; Harren, F.J.M.; Hackstein, J.H.P.; Reuss, J. Intracavity CO laser photoacoustic trace gas detection: cyclic CH_4, H_2O and CO_2 emission by cockroaches and scarab beetles. *Appl. Opt.* **1996**, *35*, 5357–5368.
11. Hornberger, C.; König, M.; Rai, S.B.; Demtröder, W. Sensitive photoacoustic overtone spectroscopy of acetylene with a multipass photoacoustic cell and a colour centre laser at 1.5 μm. *Chem. Phys.* **1995**, *190*, 171–177.
12. Nägele, M.; Sigrist, M. Mobile laser spectrometer with novel resonant multipass photoacoustic cell for trace-gas sensing. *Appl. Phys. B: Lasers Opt.* **2000**, *70*, 895–901.
13. Rey, J.; Marinov, D.; Vogler, D.; Sigrist, M. Investigation and optimisation of a multipass resonant photoacoustic cell at high absorption levels. *Appl. Phys. B* **2005**, *80*, 261–266.
14. Ioli, N.; Violino, P.; Meucci, M. A simple transversely excited spectrophone. *J. Phys. E: Sci. Instrum.* **1979**, *12*, 168–170.
15. Mattiello, M.; Niklès, M.; Schilt, S.; Thévenaz, L.; Salhi, A.; Barat, D.; Vicet, A.; Rouillard, Y.; Werner, R.; Koeth, J. Novel Helmholtz-based photoacoustic sensor for trace gas detection at ppm level using GaInAsSb/GaAlAsSb DFB lasers. *Spectrochim. Acta A: Mol. Biomol. Spectrosc.* **2006**, *63*, 952–958.
16. Hao, L.Y.; Qiang, S.; Wu, G.R.; Qi, L.; Feng, D.; Zhu, Q.S.; Hong, Z. Cylindrical mirror multipass Lissajous system for laser photoacoustic spectroscopy. *Rev. Sci. Instrum.* **2002**, *73*, 2079–2085.
17. Veeken, K.; Dam, N.; Reuss, J. A multipass transverse photoacoustic cell. *Infrared Physics* **1985**, *25*, 683–696.
18. Miklós, A.; Pei, S.C.; Kung, A.H. Multipass acoustically open photoacoustic detector for trace gas measurements. *Appl. Opt.* **2006**, *45*, 2529–2534.
19. Rothman, L.; Jacquemart, D.; Barbe, A.; Benner, D.C.; Birk, M.; Brown, L.; Carleer, M.; Chackerian, C., Jr.; Chance, K.; Coudert, L.; Dana, V.; Devi, V.; Flaud, J.M.; Gamache, R.; Goldman, A.; Hartmann, J.M.; Jucks, K.; Maki, A.; Mandin, J.Y.; Massie, S.; Orphal, J.; Perrin, A.; Rinsland, C.; Smith, M.; Tennyson, J.; Tolchenov, R.; Toth, R.; Auwera, J.V.; Varanasi, P.; Wagner, G. The HITRAN 2004 molecular spectroscopic database. *J. Quant. Spectrosc. Rad. Transfer* **2005**, *96*, 139–204.
20. Kauppinen, J.; Partanen, J. *Fourier Transforms in Spectroscopy*; WILEY-VCH Verlag: Berlin, Germany, 2001; pp. 49–59.
21. Kinsler, L.E.; Frey, A.R.; Coppens, A.B.; Sanders, J.V. *Fundamentals of Acoustics*, 3rd ed.; John Wiley & Sons: Hoboken, NJ, USA, 1982; pp. 176–197.

22. Bartlome, R.; Kaučikas, M.; Sigrist, M.W. Modulated resonant versus pulsed resonant photoacoustics in trace gas detection. *Appl. Phys. B* **2009**, *96*, 561–566.
23. Webber, M.E.; Pushkarsky, M.; Kumar, C.; Patel, N. Fiber-amplifier-enhanced photoacoustic spectroscopy with near-infrared tunable diode lasers. *Appl. Opt.* **2003**, *42*, 2119–2126.
24. Lewicki, R.; Wysocki, G.; Kosterev, A.A.; Tittel, F.K. QEPAS based detection of broadband absorbing molecules using a widely tunable, cw quantum cascade laser at 8.4 μm. *Opt. Expr.* **2007**, *15*, 7357–7366.
25. Koskinen, V.; Fonsen, J.; Roth, K.; Kauppinen, J. Cantilever enhanced photoacoustic detection of carbon dioxide using a tunable diode laser source. *Appl. Phys. B* **2007**, *86*, 451–454.

Publication 4

Toni K. Laurila, Tapio Sorvajärvi, Jaakko Saarela, Juha Toivonen, Daniel W. Wheeler, Luca Ciaffoni, Grant A. D. Ritchie, and Clemens F. Kaminski,

Optical Detection of the Anesthetic Agent Propofol in the Gas Phase.

Analytical Chemistry **83**, 3963–3967 (2011).

Publication 5

Jaakko Saarela, , Tapio Sorvajärvi, Toni Laurila, and Juha Toivonen,

Phase-sensitive method for background-compensated photoacoustic detection of NO_2 *using high-power* LED*s.*

Optics Express **19**, A725–A732 (2011).

Phase-sensitive method for background-compensated photoacoustic detection of NO_2 using high-power LEDs

Jaakko Saarela,[1,*] Tapio Sorvajärvi,[1] Toni Laurila,[2] and Juha Toivonen[1]

[1]*Optics Laboratory, Department of Physics, Tampere University of Technology, P.O. Box 692, FI-33101 Tampere, Finland*

[2]*Centre for Metrology and Accreditation, P.O. Box 9, FI-02151 Espoo, Finland*

[*]*jaakko.saarela@tut.fi*

P5

Abstract: A photoacoustic (PA) sensor has been developed for the detection of nitrogen dioxide (NO_2). Ten amplitude-modulated high-power light emitting diodes (LEDs), emitting a total optical power of 9 W at 453 nm, are used to excite the photoacoustic signal in NO_2. The LEDs are attached to the circumference of a cylindrical PA cell. The induced longitudinal acoustics waves are detected using two electromechanical film stacks, located at the ends of the cell. Background signal cancelation is achieved by using phase-sensitive detection of the difference signal of the two pressure transducers. The phase-sensitive approach allows for improved dynamic range and sensitivity. A detection limit of 10 parts per billion by volume was achieved for flowing NO_2 gas sample in an acquisition time of 2.1 s, corresponding to a minimum detectable absorption coefficient of 1.6×10^{-7} $cm^{-1}Hz^{-1/2}$. The developed sensor has potential for compact, light-weight, and low-cost measurement of NO_2.

OCIS codes: (300.6430) Spectroscopy, photothermal; (300.6380) Spectroscopy, modulation; (230.3670) Light-emitting diodes; (120.5475) Pressure measurement; (120.5050) Phase measurement.

References and links

1. A. Rosencwaig, *Photoacoustics and Photoacoustic Spectroscopy* (Robert E. Krieger Publishing Company, 1980).
2. "Our Nation's Air–Status and Trends through 2008," Tech. Rep., U.S. Environmental Protection Agency (2010).
3. J. H. Shorter, S. Herndon, M. S. Zahniser, D. D. Nelson, J. Wormhoudt, K. L. Demerjian, and C. E. Kolb, "Real-time measurements of nitrogen oxide emissions from in-use New York City Transit buses using a chase vehicle," Environ. Sci. Technol. **39**, 7991–8000 (2005).
4. P. C. Claspy, C. Ha, and Y.-H. Pao, "Optoacoustic detection of NO_2 using a pulsed dye laser," Appl. Opt. **16**, 2972–2973 (1977).
5. J. Saarela, J. Sand, T. Sorvajrvi, A. Manninen, and J. Toivonen, "Transversely excited multipass photoacoustic cell using electromechanical film as microphone," Sensors **10**, 5294–5307 (2010).
6. A. Manninen, J. Sand, J. Saarela, T. Sorvajärvi, J. Toivonen, and R. Hernberg, "Electromechanical film as a photoacoustic transducer," Opt. Express **17**, 16994–16999 (2009).
7. N. Barreiro, A. Vallespi, A. Peuriot, V. Slezak, and G. Santiago, "Quenching effects on pulsed photoacoustic signals in NO_2-air samples," Appl. Phys. B: Lasers Opt. **99**, 591–597 (2010).
8. R. Bartlome, M. Kaučikas, and M. W. Sigrist, "Modulated resonant versus pulsed resonant photoacoustics intrace gas detection," Appl. Phys. B **96**, 561–566 (2009).
9. V. Slezak, "High-precision pulsed photoacoustic spectroscopy in NO_2-N_2," Appl. Phys. B: Lasers Opt. **73**, 751–755 (2001).

#145946 - $15.00 USD Received 14 Apr 2011; revised 18 May 2011; accepted 19 May 2011; published 26 May 2011

10. V. Slezak, G. Santiago, and A. L. Peuriot, "Photoacoustic detection of NO_2 traces with CW and pulsed green lasers," Opt. Lasers Eng. **40**, 33–41 (2003).
11. H. Yi, K. Liu, W. Chen, T. Tan, L. Wang, and X. Gao, "Application of a broadband blue laser diode to trace NO_2 detection using off-beam quartz-enhanced photoacoustic spectroscopy," Opt. Lett. **36**, 481–483 (2011).
12. J. Kalkman and H. van Kesteren, "Relaxation effects and high sensitivity photoacoustic detection of NO_2 with a blue laser diode," Appl. Phys. B: Lasers Opt. **90**, 197–200 (2008).
13. M. Pushkarsky, A. Tsekoun, I. G. Dunayevskiy, R. Go, and C. K. N. Patel, "Sub-parts-per-billion level detection of NO_2 using room-temperature quantum cascade lasers," Proc. Natl. Acad. Sci. U.S.A. **103**, 10846–10849 (2006).
14. J. Lima, H. Vargas, A. Mikls, M. Angelmahr, and P. Hess, "Photoacoustic detection of NO_2 and N_2O using quantum cascade lasers," Appl. Phys. B: Lasers Opt. **85**, 279–284 (2006).
15. R. Bernhardt, G. D. Santiago, V. B. Slezak, A. Peuriot, and M. G. Gonzlez, "Differential, LED-excited, resonant NO_2 photoacoustic system," Sens. Actuators B **150**, 513–516 (2010).
16. G. D. Santiago, M. G. Gonzalez, A. L. Peuriot, F. Gonzalez, and V. B. Slezak, "Blue light-emitting diode-based, enhanced resonant excitation of longitudinal acoustic modes in a closed pipe with application to NO_2," Rev. Sci. Instrum. **77**, 023108 (2006).
17. K. Bogumil, J. Orphal, T. Homann, S. Voigt, P. Spietz, O. C. Fleischmann, A. Vogel, M. Hartmann, H. Kromminga, H. Bovensmann, J. Frerick, and J. P. Burrows, "Measurements of molecular absorption spectra with the SCIAMACHY pre-fight model: instrument characterization and reference data for atmospheric remote-sensing in the 2302380 nm region," J. Photochem. Photobiol., A **157**, 167–184 (2003).
18. V. Sivakumaran, K. P. Subramanian, and V. Kumar, "Self-quenching and zero-pressure lifetime studies of NO_2 at 465-490, 423-462 and 399-416 nm," J. Quant. Spectrosc. Radiat. Transf. **69**, 525–534 (2001).
19. R. A. Gangi and L. Burnelle, "Electronic structure and electronic spectrum of nitrogen dioxide. III Spectral interpretation," J. Chem. Phys. **55**, 851–856 (1971).
20. C. M. Roehl, J. J. Orlando, G. S. Tyndall, R. E. Shetter, G. J. Vazquez, C. A. Cantrell, and J. G. Calvert, "Temperature dependence of the quantum yields for the photolysis of NO_2 near the dissociation limit," J. Chem. Phys. **98**, 7837–7843 (1994).
21. A. Manninen, "Pulsed Laser Spectroscopy: Bioaerosol Fluorescence and Gas-Phase Photoacoustics," Ph.D. thesis, Tampere University of Technology (2009).
22. M. Paajanen, J. Lekkala, and K. Kirjavainen, "Electromechanical film (EMFi)–a new multipurpose electret material," Sens. Actuators, A **84**, 95–102 (2000).
23. Y.-H. Pao, P. C. Claspy, C. F. j. Dewey, J. A. Gelbwachs, P. L. Kelley, L. B. Kreuzer, M. B. Robin, A. Rosencwaig, J. D. Stettler, and N. M. Witiriol, *Optoacoustic Spectroscopy and Detection* (Academic Press, Inc., 1977).
24. A. Miklós, P. Hess, and Z. Bozóki, "Application of acoustic resonators in photoacoustic trace gas analysis and metrology," Rev. Sci. Instrum. **72**, 1937–1955 (2001).
25. A. Kosterev, Y. Bakhirkin, F. Tittel, S. Blaser, Y. Bonetti, and L. Hvozdara, "Photoacoustic phase shift as a chemically selective spectroscopic parameter," Appl. Phys. B: Lasers Opt. **78**, 673–676 (2004).
26. G. Z. Angeli, Z. Bozoki, A. Miklos, A. Lorincz, A. Thony, and M. W. Sigrist, "Design and characterization of a windowless resonant photoacoustic chamber equipped with resonance locking circuitry," Rev. Sci. Instrum. **62**, 810–813 (1991).

1. Introduction

Photoacoustic spectroscopy (PAS) is an established and sensitive method for trace gas monitoring. It is based on the photoacoustic (PA) effect where modulated light is absorbed by gas molecules and converted to sound by non-radiative relaxation of the excited energy levels of the molecules. The induced sound waves are detected with a microphone. [1]

Nitrogen dioxide (NO_2) is an atmospheric pollutant which is mainly emitted into the atmosphere from anthropogenetic sources, such as combustion processes. The average mixing ratio of NO_2 in the atmosphere is typically between $5-30$ parts per billion by volume (ppb) [2] but can be orders of magnitude higher close to its source [3]. PAS has been previously applied to the detection of NO_2 using pulsed dye lasers [4], solid-state lasers [5–10], semiconductor diode lasers [11, 12], quantum cascade lasers [13, 14], and light emitting diodes (LEDs) [15, 16]. Since the PA signal is directly proportional to the excitation power [1], it is favorable to use high-power light sources for excitation. In the visible spectral range modern high-power LEDs offer an attractive alternative by reaching power levels beyond 1 W. Combined with low-cost microphone technology, LED-based PA sensors provide an interesting and cost-effective solution for NO_2 monitoring.

#145946 - $15.00 USD Received 14 Apr 2011; revised 18 May 2011; accepted 19 May 2011; published 26 May 2011

NO_2 has a strong and broadband absorption spectrum covering the $250-650$ nm spectral range with a maximum absorption cross-section of 7.4×10^{-19} cm^2/molecule at 414 nm [17]. The zero-pressure fluorescence lifetime of NO_2 in the excitation band of $423-464$ nm is approximately 43 μs [18], whereas the non-radiative lifetime is less than 4 μs at atmospheric pressure [12]. Thus, approximately 90 % of the absorbed light energy is expected to be converted to pressure through the PA effect. However, below 415 nm photochemical dissociation of NO_2 occurs [19, 20], which has been observed to reduce the PA signal by about 30 % at 510 Hz modulation frequency [1] and even more so at higher frequencies [21]. Therefore, excitation at slightly longer wavelengths is preferable, although high-power LEDs are available around the peak absorption of NO_2.

In this work sensitive PA detection of NO_2 is demonstrated using an array of ten amplitude-modulated high-power LEDs, emitting a total power of 9 W around 453 nm. The LEDs illuminate a cylindrical PA cell and excite its second longitudinal acoustic mode at 3.9 kHz resonance frequency. The induced pressure waves are detected with two stacks of five-layer electromechanical (EMFIT) films that are attached to the ends of the PA cell. EMFIT film microphones have recently been introduced for PAS of gases as a low-cost, light-weight, and wide-bandwidth alternative for condenser microphones [5, 6]. The EMFIT microphones are flexible, 70-μm-thick polymer films having ferroelectric properties [22]. Thin metal electrodes on both sides of the film stack allow the extraction of the pressure-induced electric signal. In this study, the two EMFIT stacks are oriented in such a way that the internal electric polarizations are in opposite directions. This novel construction results in a 180° phase difference between the two microphone signals. By monitoring their difference, common-mode electrical or vibrational disturbances are canceled.

PA background signal is a common drawback in systems using amplitude-modulated high-power light sources. The background signal stems from light being absorbed to the walls and windows of the measurement cell. If the background signal is in phase with the induced PA signal from the gas, a simple background subtraction technique can be applied. However, if the PA background has an opposite-phase component, the dynamic range and detection limit of a PA detector can be limited [23]. A common method to reduce such unwanted background signals is to use acoustic filters [24]. In this study, the remaining PA background in the difference signal was observed to originate from the high-power LEDs. This background can be distinguished from the PA signal of NO_2 using phase-sensitive detection. Finally, it is demonstrated that the phase of the PA signal can also be used to track the frequency of the acoustic resonance which drifts due to changes in the gas temperature.

2. Photoacoustic cell with high-power LEDs

The schematic of the PA sensor is shown in Fig. 1. Two five-layer EMFIT film microphones seal the ends of the cylindrical resonator, made of acrylic plastic. The length and inner diameter of the resonator are 9.0 cm and 3.6 cm, respectively. The quality factor (Q) of the PA cell was measured to be 50 at the second longitudinal mode of 3.9 kHz. The microphones were constructed by gluing five circular sheets of EMFIT films together so that their permanent internal polarizations were orientated in the same direction. Stacking five films together yields approximately five-fold sensitivity [5]. Finally, the two film stacks were attached onto grounded aluminum back-plates with positive and negative electrodes facing each other which results in 180° phase difference between their acoustic responses. By measuring the difference of the microphone signals, common-mode electrical or vibrational disturbances are eliminated while the overall signal is doubled.

#145946 - $15.00 USD Received 14 Apr 2011; revised 18 May 2011; accepted 19 May 2011; published 26 May 2011

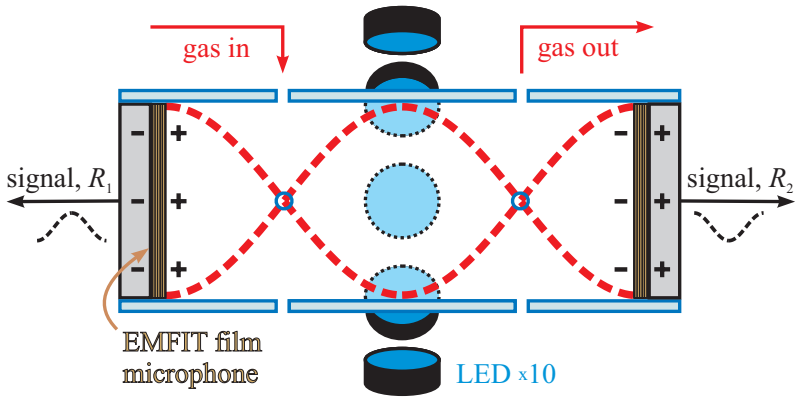

Fig. 1. Photoacoustic (PA) cell. Ten blue (453 nm) high-power LEDs are attached to the central part of the cell to excite acoustic waves at the second longitudinal mode when NO_2 is present. NO_2 monitoring is accomplished by measuring the difference of the opposite-phase PA signals of two EMFIT film microphones.

Ten blue high-power LEDs (LDW5AM-3T-4-0, OSRAM Opto Semiconductors) with metal-core printed circuit boards are attached onto the decahedron-shaped inner surface of the PA cell's aluminum body. The body functions both as a heat sink for the LEDs and an acoustic enclosure. The distance from the LEDs to the inner surface of the acrylic resonator tube is approximately 3.5 cm. The LEDs are close to Lambertian light sources with highly diverging emission. The full width at half maximum (FWHM) angle of the emission pattern is approximately 120°. The diverging emission was collimated using a plastic (polymethylmethacrylate, PMMA) lens

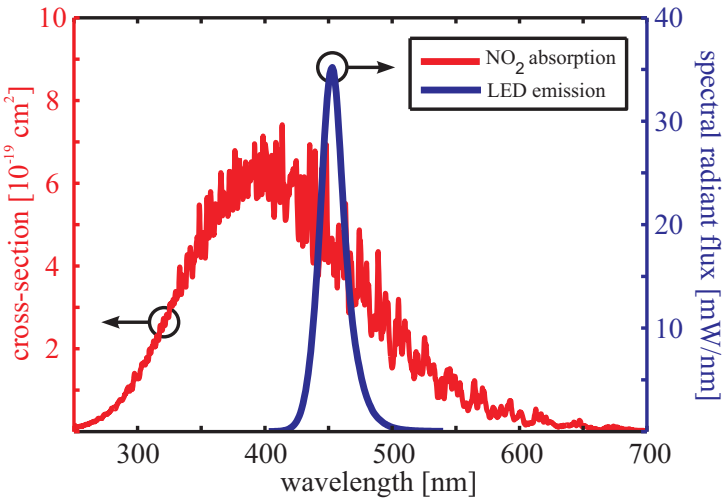

Fig. 2. Absorption cross-section of nitrogen dioxide [17], and the emission spectrum of a high-power LED.

#145946 - $15.00 USD Received 14 Apr 2011; revised 18 May 2011; accepted 19 May 2011; published 26 May 2011

(LO2-RS, Ledil) into a FWHM angle of 7°. The collimation efficiency was measured with an integrating sphere and it was over 90 % for the particular lens used. The peak wavelength, linewidth, and the delivered emission power at 1 A electric peak current were 453 nm, 23 nm, and 900 mW, respectively. The spectral emission of one LED is shown in Fig. 2 together with the absorption cross-section of NO_2. The effective absorption cross-section within the LED emission profile is 4.5×10^{-19} cm^2/molecule, calculated for an optically thin NO_2 gas as the average cross-section weighted by the LED emission spectrum.

Square-wave-modulated electric current is provided to the series-connected LEDs through an in-house built current driver that is controlled with a function generator (33250A, Agilent Technologies). The gas sample is diluted from 308 ppm NO_2–N_2 mixture (AGA) using a cascade of two mass flow controller units (5850S, Brooks Instrument). The gas is fed into the resonator through four 1-mm-sized holes that are located at the nodal points of the second eigenmode, minimizing the coupling of ambient acoustic noise into the PA cell.

3. Photoacoustic signal

The generation of the difference PA signal is illustrated in Fig. 3. Both the absorbing NO_2 molecules (R_s) and the background (R_b) contribute to the PA signal. In general, the two PA signal components, R_s and R_b, have a fixed phase difference θ, which describes the delay between the PA signal from NO_2 and the background. The delay can arise either from different relaxation rates at which the two sound waves are produced or from the difference in their acoustic propagation path lengths. Here, the non-radiative relaxations are fast compared to the modulation period, and thus, only the propagation delay has an effect on the phase θ.

Neglecting common-mode in-phase components the two microphone signals can be expressed as $R_1 = \left(R_{s1}e^{i\theta} + R_{b1}\right)e^{i\phi}$, and $R_2 = \left(R_{s2}e^{i\theta} + R_{b2}\right)e^{i(\pi+\phi)}$, where ϕ is a frequency-dependent PA signal phase which is caused by the longitudinal acoustic resonance and is the same for both the PA signal and background. Assuming equal microphone sensitivities, the magnitudes $R_{s1} = R_{s2} = R_s$ and $R_{b1} = R_{b2} = R_b$. Hence, the difference PA signal is $R_1 - R_2 = 2\left(R_s e^{i\theta} + R_b\right)e^{i\phi}$. The measurement delay can be adjusted, i.e. the reference coordinate system can be rotated, in such a way that $\phi = 0$ at the resonance of the PA cell. Then, as depicted in Fig. 3 a, the background becomes purely real, and the NO_2 signal projection is achieved from the imaginary part of the resultant PA signal. Kosterev et al. have used a similar

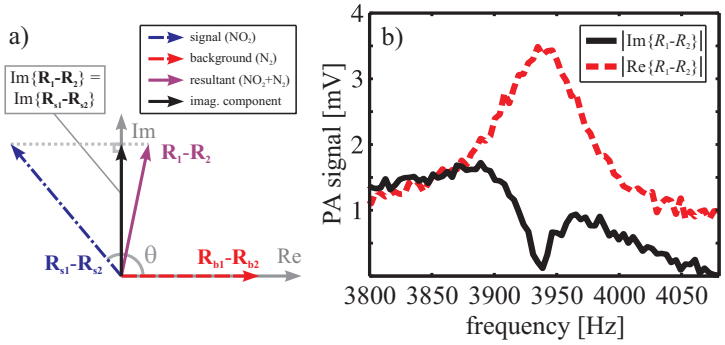

Fig. 3. Generation of the difference PA signal. **(a)** The resultant signal has only components of PA origin. Background-free measurement of NO_2 is achieved from the imaginary component. **(b)** Measured PA backgrounds from an empty (N_2-filled) cell. At the resonance of the PA cell (3940 Hz) the imaginary component of the PA background signal is reduced to the combined noise level of the two microphones.

#145946 - $15.00 USD Received 14 Apr 2011; revised 18 May 2011; accepted 19 May 2011; published 26 May 2011

phase-sensitive approach to distinguish between two gases, which have overlapping absorption features but different non-radiative lifetimes [25].

The opposite-phase PA signals R_1 and R_2 are amplified by 60 dB and then digitized with a 2-channel oscilloscope (NI USB-5133, National Instruments) using a sampling rate and data record length of 1 MS/s and 2^{19}, respectively. The PA signals are processed using a LabVIEW program. Four difference PA signals are averaged, yielding a data acquisition time of 2.1 s, and the fast-Fourier transformation (FFT) is calculated to retrieve the PA signal magnitude and phase. The real and imaginary components of PA signals are commonly separated using a lock-in amplifier. Alternatively, they can be calculated from the complex-valued FFT spectrum as done here.

It was observed that the high-power LEDs generate audible background noise when driven at kHz frequencies. The background noise (R_b) is coupled to the acoustic resonance $(3940\ \text{Hz})$ of the PA cell, even with the cell being filled with pure N_2, as shown with the dashed line in Fig. 3 b. However, this background signal can be distinguished from the PA signal of NO_2 due to the phase shift of 130°, caused by the different propagation lengths in the cell. At the resonance frequency $\phi = 0$ and the background is real, and therefore, the background is eliminated from the imaginary component of the PA signal which is shown with the solid line in Fig. 3 b. Continuous background-compensated monitoring of NO_2 concentration is achieved if the modulation frequency of the LEDs is kept at the resonance of the PA cell.

The PA background could also be compensated by using extra LEDs of different color that are modulated with an opposite phase [15]. However, with the presented method the PA background is automatically eliminated by measuring the imaginary PA signal component instead of the resultant, and no extra components are needed. Yet, the method of using extra LEDs of different color and opposite-phase modulation could be used to eliminate possible interference from other atmospheric compounds which absorb visible light, such as ozone and soot particles.

4. Results

The PA signal was measured as a function of NO_2 concentration both from the resultant amplitude and from the imaginary component of the complex difference signal. The open data points in Fig. 4 show resultant PA signal in the presence of 3.5 mV PA background. The phase of the PA background lags 130° with respect to the PA signal from NO_2 as can be seen from the inset of Fig. 4. This corresponds to an acoustic path length of 3.3 cm which approximately matches the distance from the LEDs to the outer surface of the acrylic resonator tube. This implies that the LEDs themselves were the source of the PA background instead of the light absorption at plastic walls of the resonator tube. Due to the phase lag the PA response dips around 300 ppb, whereafter the PA signal increases monotonically. Because the phase lag is more than 90°, background-subtraction technique does not improve the limit of detection.

The linear regime is extended to the combined electrical noise floor of the two microphones by measuring the imaginary component of the difference PA signal. Only 25 % of the PA signal is lost from the imaginary part due to the phase difference between the signal from NO_2 and background. This reduction could be avoided by re-designing the PA cell so that the LEDs would be located at exactly a quarter wavelength, which is 2.25 cm, apart from the acoustic resonator. In-phase PA background, which would arise from light absorption at the plastic cylinder walls and be larger than the measured electrical noise, was not observed. In fact, even if a small-amplitude in-phase PA background component existed, the detection phase could be fine-tuned in such a way that the resultant PA background would again be balanced out from the imaginary part of the PA signal. The noise level (80 μV) was measured as the root-mean-square (RMS) noise of the imaginary component from pure N_2 at the 2nd longitudinal resonance of the PA cell while the LEDs were being modulated. The detection limit for NO_2 in N_2 matrix is

#145946 - $15.00 USD Received 14 Apr 2011; revised 18 May 2011; accepted 19 May 2011; published 26 May 2011

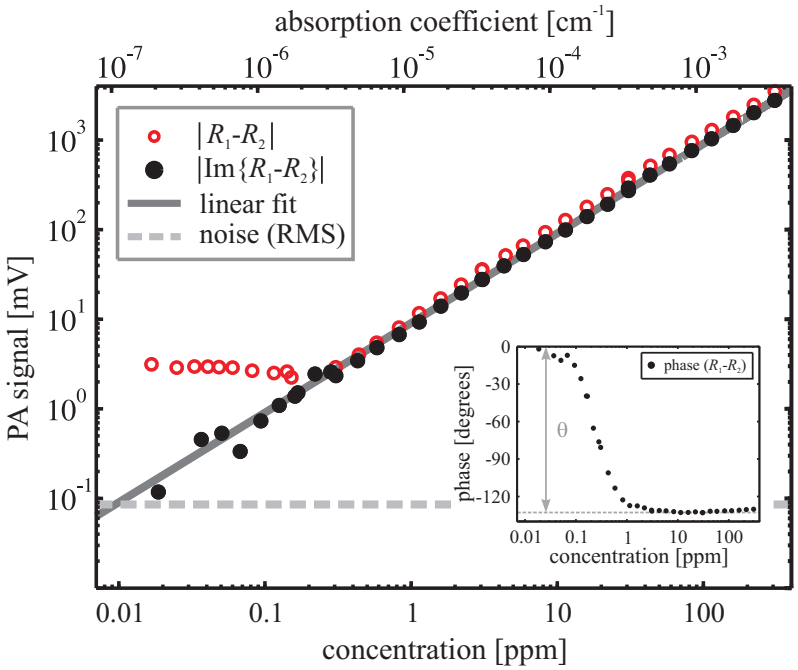

Fig. 4. PA signal as a function of NO_2 concentration. Open circles represent the PA signal in the presence of 3.5 mV background. The linear dynamic range is extended to the noise floor by measuring the imaginary component of the PA difference signal. The detection limit with 2.1 s acquisition time is 10 ppb. Inset: Phase of the resultant PA signal. Due to the phase difference $\theta = 130^\circ$ background-free measurement of NO_2 is achieved from the imaginary component.

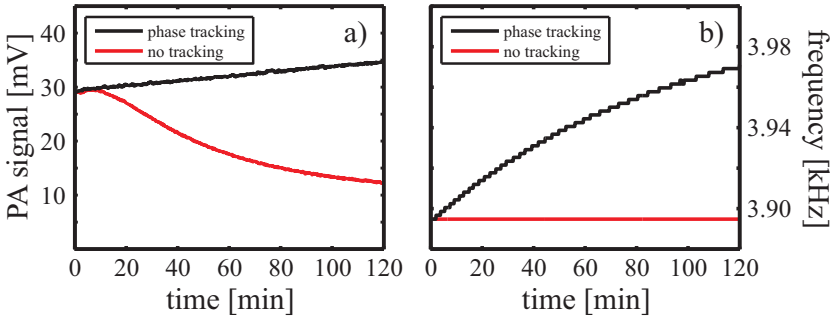

Fig. 5. Imaginary part of the PA signal as a function of time, measured from a constant 3 ppm NO_2 concentration **(a)**, and the corresponding signal frequencies **(b)**. The PA cell is heated by the high-power LEDs from 25°C to 40°C, causing the resonance frequency to drift to higher frequencies. Without resonance tracking the PA signal is lost (red curves). The resonance tracking enables continuous monitoring of NO_2 (black curves). The increase in PA signal is related to temperature-dependent sensitivity of the microphones.

#145946 - $15.00 USD Received 14 Apr 2011; revised 18 May 2011; accepted 19 May 2011; published 26 May 2011

10 ppb (SNR= 1) with 2.1 s data acquisition time which corresponds to a minimum detectable absorption coefficient of 1.1×10^{-7} cm^{-1} or 1.6×10^{-7} cm^{-1}Hz$^{-1/2}$. The sensitivity of the PA detector is about 180 V$/\left(\text{cm}^{-1}\text{W}\right)$ when normalized with the emitted average power of the LEDs.

During long-term PA measurements temporal changes in the gas temperature can cause problems, especially when using continuous-wave light sources, because the speed of sound is temperature-dependent, and, so is the resonance frequency [24]. In the presented set-up the PA cell itself is heated by the high-power LEDs. Therefore, a feedback algorithm was used to continuously track and minimize the difference between the modulation frequency and the actual resonance of the PA cell. As a demonstration, 3 ppm of NO_2 was set to flow at one standard liter per minute through the PA cell, and a signal stability measurement was carried out during which the PA cell temperature increased from 25 to 40°C. The effect of not using any resonance tracking is seen in the decaying PA signal curve of Fig. 5 a which was measured using a fixed modulation frequency of 3,895 Hz. By tracking the resonance frequency of the PA cell from the signal phase, which is $-130°$ at 3 ppm, the PA system followed the drifting resonance. At the same time the PA signal increased slowly by 17 % even though the NO_2 concentration was kept constant. The change is related to the increasing sensitivities of the microphone film stacks as a function of temperature, which was experimentally verified using an external loudspeaker. However, this could be easily taken into account by microphone calibration or by controlling the PA cell temperature. It was also checked that the radiant flux of the high-power LEDs reduced only by 1 % as the operating temperature of the PA cell increased. All the PA measurements were carried out in a constant atmospheric pressure, and the NO_2 absorption spectrum is not affected by such small temperature changes. It should be noted that the presented method of tracking the resonance directly from the PA signal phase works here only at sample concentrations above 1 ppm where the phase is constant. An additional loudspeaker, driven at some higher harmonic than the 2$^{\text{nd}}$ mode used for PA detection, could be integrated into the PA cell in order to make the resonance tracking concentration-independent [26].

5. Conclusion

Photoacoustic detection of NO_2 was demonstrated using an array of ten high-power LEDs, which were arranged onto the outer circumference of a transparent cylindrical PA cell. The total emission power and wavelength of the LEDs were 9 W and 453 nm, respectively. The overlapping beams from the LEDs excited pressure waves from NO_2 gas at the center of the PA cell. The pressure waves were detected using two stacks of 5-layer electromechanical film microphones. The internal electric polarizations of the film stacks were oriented in opposite directions resulting in opposite-phase PA signals. By measuring the difference of the two microphone signals and by using phase sensitive detection, the background signal that originated from the high-power LEDs, was eliminated improving the linear dynamic range of the PA detector. The minimum detectable absorption coefficient was 1.1×10^{-7} cm^{-1} in a measurement time of 2.1 s which corresponds to 10 ppb of NO_2 in N_2. The developed sensor has potential for compact, light-weight, and low-cost measurement of toxic NO_2. The presented PA system could also be modified for the measurement of other atmospheric trace constituents, such as soot particles or ozone, which absorb light in the visible spectral range.

Acknowledgements

OSRAM Opto Semiconductors GmbH is appreciated for providing the blue high-power LEDs. The authors would like to thank Lic.Sc. Tuomas Poikonen from Aalto University, School of Science and Technology for measuring the spectral radiant flux of the LEDs.

#145946 - $15.00 USD Received 14 Apr 2011; revised 18 May 2011; accepted 19 May 2011; published 26 May 2011

Tampereen teknillinen yliopisto
PL 527
33101 Tampere

Tampere University of Technology
P.O.B. 527
FI-33101 Tampere, Finland

ISBN 978-952-15-2676-3
ISSN 1459-2045